1-31-2013

Data compressive paradigm for spectral sensing and classification using electrically tunable detectors

Woo-Yong Jang

Woo-Yong Jang
Candidate

Electrical and Computer Engineering
Department

This dissertation is approved, and it is acceptable in quality and form for publication:

Approved by the Dissertation Committee:

Sanjay Krishna , Chairperson

Majeed M. Hayat

Steven R. J. Brueck

Sudhakar Prasad

Payman Zarkesh-Ha

DATA COMPRESSIVE PARADIGM FOR SPECTRAL SENSING AND CLASSIFICATION USING ELECTRICALLY TUNABLE DETECTORS

by

WOO-YONG JANG

B.E. (Hons), Engineering, University of Canterbury, 2001
M.S., Engineering, University of Southern California, 2004

DISSERTATION

Submitted in Partial Fulfillment of the
Requirements for the Degree of

Doctor of Philosophy
Engineering

The University of New Mexico
Albuquerque, New Mexico

December, 2012

Dedication

To my parents.

Acknowledgments

First of all, I would like to thank my wife, Jinyoung Lee, for her support and patience through the years of my Ph.D. study. Thank you for taking care of our lovely daughter Khloe. I would also like to thank my parents in New Zealand and my parents-in-law in Korea for their endless support.

I would like to thank my advisors, Professor Majeed M. Hayat and Professor Sanjay Krishna for their professional guidance. Without them, it would not have been possible to successfully complete my Ph.D.

I would like to thank my committee members, Professor Steven R. J. Brueck, Professor Sudhakar Prasad and Professor Payman Zarkesh-ha for their valuable comments to strengthen my dissertation. I would also like to thank collaborators, Professor Chee Hing Tan and Dr. Peter Vines from the University of Sheffield and Dr. Steven Bender from the Los Alamos National Laboratory.

I would like to thank my colleagues, Dr. David Ramirez, Dr. Biliana Paskaleva, Mr. Sebastian Godoy for all your help and friendship. I also thank all other group members. I will remember all the good memories of CHTM.

Finally, I would like to acknowledge funding agencies, the National Consortium for MASINT Research Partnership Project led by Defense Intelligence Agency and the National Science Foundation under awards ECCS-0925757, IIS-0434102 and ECS-0401154.

Data Compressive Paradigm for Spectral Sensing and Classification using Electrically Tunable Detectors

by

Woo-Yong Jang

B.E. (Hons), Engineering, University of Canterbury, 2001
M.S., Engineering, University of Southern California, 2004
Ph.D., Engineering, University of New Mexico, 2012

Abstract

It is well known that the inclusion of detailed spectral information in sensing, by means of targeting more bands with finer resolution, can enhance the performance of any application substantially. Unfortunately, this enhancement is clearly accompanied by a dramatic increase in the amount of collected data and increase in its dimensionality. Nature has, nevertheless, found a way to break this trade-off by finding ways to transmit what is needed. The human eye can distinguish more than 16 million colors but the retina strips the images down to its bare essentials before sending visual information to the brain. Such front-end processing is performed in the retina [Wässle *et al*., Nature Reviews Neuroscience, vol. 5, pp. 747–757, 2004]. There is evidence to believe that only 10-12 output channels, with a sparse representation of the world, are sent from the eye to the brain and each of these compressed signals, such as a signal representing color and the detection of a moving edge, are created by a set of amacrine cells [Roska *et al*., Nature, vol. 410, pp. 583–587, 2001]. As man-made sensors have evolved beyond the visible domain to the infrared and terahertz domains with fine spectral resolution and long spans in data acquisition.

Among man-made spectral sensors, multispectral (MS) and hyperspectral (HS) infrared (IR) sensors have become known as enablers of a wide range of remote-sensing applications. Over the past twenty years, the demand for MS/HS sensing

systems has been increasing steadily and many sensor technologies have been developed. Unlike the human eye, however, a MS/HS imager typically collects the maximum amount of spectral data corresponding to a large number of spectral bands (e.g. upwards of 15 bands in MS sensors and 350 bands in HS sensors). Such massive data acquisition requires long data-acquisition times, large data storage and a powerful processing unit to process and analyze the data via suitable algorithms. Inspired by the need to sense only the relevant information for a specific sensing application, the main objective of this dissertation is to develop and demonstrate data-compressive IR spectral-sensing algorithms and systems geared toward coarsely and electrically tunable nanoscale IR detectors, developed at Center for High Technology Materials, that can identify and employ minimal (compressed) set of spectral data required for applications including spectrometry, object classification and MS sensing in general. The data-compressive sensing algorithms developed here aim to pave the way for the development of a real-time, smart-pixel MS/HS sensing systems.

Specifically, this dissertation contains three major parts: (1) demonstration of the algorithmic spectrometry in the mid-IR sensing regime using spectrally tunable quantum dots-in-a-well (DWELL) IR detector without employing any spectral filters; (2) further demonstration of the spectral-classification capability of tunable DWELL IR focal-plane array (FPA), again without using any spectral filters; and (3) development of a generalized filter-free data-compressive spectral sensing paradigm using the DWELL detector that enables arbitrarily specified MS sensing (e.g., spectral matched filtering, slope sensing, multicolor sensing, etc.) without using any spectral filters and possibly under constrained acquisition times.

The DWELL detector offers relatively broad bias-dependent spectral tunability, resulting in data that is spectrally rich yet with a high level of redundancy. One of the main tasks of this dissertation is to create post-processing algorithms to deconvolve this redundancy in the data so that detailed spectral information is extracted beyond that which is readily accessible in the raw data. At the heart of these algorithms is our ability to approximate arbitrarily specified spectral shapes, e.g., a narrowband filter, a multiband filter, reflectance/transmittance spectrum of some material, etc., by means of forming a weighted linear superposition of the DWELL's bias-dependent spectral responses. These algorithms carefully take into account the detector's bias-dependent signal-to-noise ratio (SNR) in the calculation of the superposition weights so as to minimize the effect of noise accumulation in the superposition process. For the

spectrometry problem, the transmittance or reflectance of an unknown target at any wavelength is reconstructed by forming a superposition of photocurrents, one for each selected applied bias, using appropriate weights specified for each center wavelength of a hypothetical narrowband filter with a specified spectral resolution. This process eliminates the need for actual spectral filters. The post-processing algorithms are further extended to identify compressed bias sets to be used in the superposition process, resulting in uniformly-accurate solutions to arbitrarily specified MS sensing problems beyond spectrometry, including spectral matched filtering. For example, our experiments show that a minimum four biases out of 30 biases can be extracted, corresponding to a significant data reduction by a factor of 7.5, to achieve a performance that approximates that obtained while employing all 30 biases. Hence, the new compressive spectral-sensing paradigm developed in this dissertation takes us one step closer to mimicking the way a human retina works in its ability to sense only the relevant information that is needed for a specific application.

Contents

List of Figures

List of Tables

Chapter 1

Introduction

While the thrust of this dissertation is algorithm development and validation for spectral sensing with certain state-of-the-art detector technologies developed at UNM, it is important to first give a brief survey of infrared sensing technology before introducing the main content of the dissertation. As such, we follow the survey by a subsection on the motivation for this dissertation, a summary of prior work and a summary of the key contributions of this dissertation.

1.1 State of the art in infrared detectors

The important performance metric (or broadband figures of merit) in mid-IR detectors are detectivity, quantum efficiency and noise equivalent difference in temperature. The detectivity D^* [1,2] is defined as the normalized signal-to-noise ratio performance of detectors. The quantum efficiency (QE) [1,2] is defined as the number of electron-hole pairs generated per incident photon. The noise equivalent difference in temperature (NEDT) [3] is the relevant parameter for focal-plane array (FPA), which is the smallest difference in a uniform temperature scene that the FPA can detect. The smaller the NEDT, the better in terms of the sensitivity of FPA. Mercury cadmium telluride (HgCdTe) IR detector [1], as shown in Fig. 1.1, is predominantly the current state-of-the-art as it continues to demonstrate superior sensitivity (high $D^* \geq 10^{12}$ $\text{cmHz}^{1/2}\text{W}^{-1}$, QE $\geq 70\%$ and pixel NEDT ≤ 10 mK) as compared to the state-of-the-art quantum dot IR photodetector (QDIP) or quantum well IR photodetector (QWIP) [1,2] in mid-IR region. For multispectral sensing, HgCdTe detectors have also been integrated with arrays of diffractive optics at the detector level. Examples of such diffractive optics are lenslet arrays [4], micro-electromechanical systems (MEMS) [5] and acousto-optic tunable filters (AOTFs) [6]. Sample images of HgCdTe IR FPA are shown in Fig. 1.2. However, despite its superior performance, HgCdTe suffers from difficulties in spatial uniformity, problems in epitaxial growth and low fabrication yields, leading to extremely expensive manufacturing of large FPAs extremely expensive [1,7,8] and also are not spectrally tunable. Another dominant technology is the micro-bolometer, which

is an uncooled semiconductor device (room temperature operation), in which the incident IR radiation heats the pixel elements and causes a change in the resistance of the pixel. Due to the nature of the thermal energy transfer process, micro-bolometer [9] detector have slow response (milliseconds) and hence find very limited use in high performance applications which require large frame rates with small integration times. Moreover, the bolometer is spectrally broad and is not tunable.

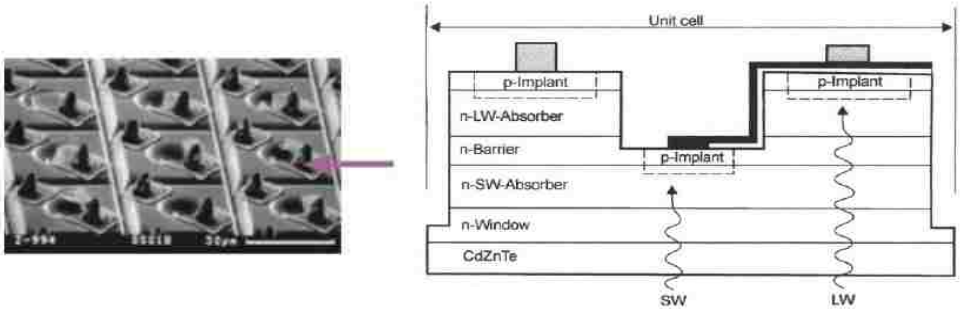

Figure 1.1: Cross section view of unit cell for back-illuminated dual-band HgCdTe detector approach [2]

Figure 1.2: MWIR and LWIR images taken with two-color HgCdTe FPA [2]

One of the potential alternatives to replace above technologies is InAs-GaSb strained layer superlattice (SLS) material system [10,11]. SLS has theoretically been predicted to yield a higher D^*, than HgCdTe. The SLS system has shown the potential to operate at room temperature. Since SLS can usually be grown with greater uniformity on cheaper substrates, the yields are expected to be greater. However, one of the major drawbacks is the control of interfaces between the InGaSb/InAs material, which can significantly affect the cutoff wavelength of the device and the dark current. Also the processing of SLS structure is difficult, due to the high surface leakage currents. The surface currents dominate the bulk currents and limit the performance of the devices, as the pixel sizes become smaller. Nonetheless, SLS is a promising technology for IR detection. Images taken by the dual color SLS FPA are shown in Fig. 1.3.

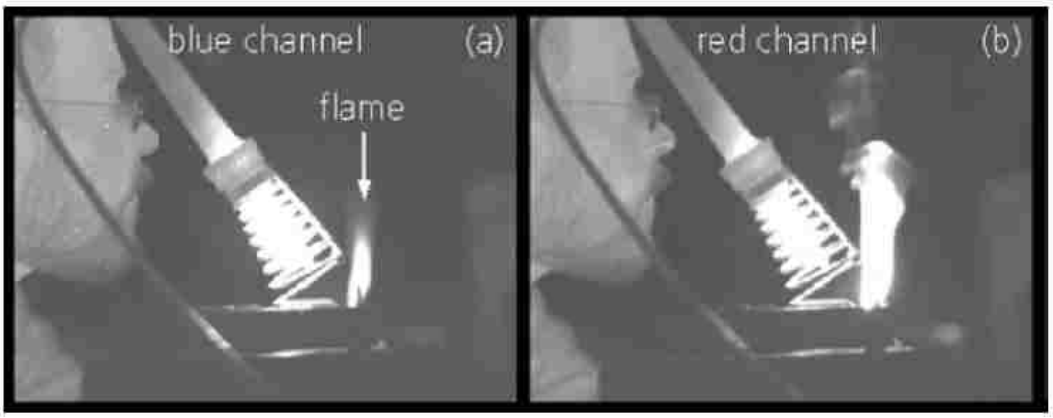

Figure 1.3: Images taken by the dual color InAs/GaSb SLS FPA [2]. MWIR (blue channel) image is on the left and LWIR (red channel) image is shown on the right.

Other potential alternatives are the intersubband detectors such as QWIP and QDIP shown in Fig. 1.4. Standard QWIP [12] is based on the III-V mature material systems increasing the feasibility of production with low cost and large scale devices as compared to current state of the art detectors. Potential advantages of QWIP FPAs [2] include a lower uncorrected-response nonuniformity (typically 1 %–3 %) coupled with a higher operability (above 99.9 %) compared to HgCdTe detectors [2]. Images captured by QWIP FPA are shown in Fig. 1.5. QDIPs [13,14] have some advantages over QWIPs. The advantages of QDIPs include normal incidence operation [15,16], lower darkcurrent due to increased lifetime [15-17], higher operating temperature and D^* [15-17] than QWIPs. Additionally, QDIPs offer the electrically tunable spectral response through the applied bias voltages. As a result of the quantum-confined Stark effect [18,19], a single QDIP can serve as a multispectral detector without any dispersive optics. In Table 1.1, QWIP, QDIP, SLS and micro-bolometer detectors are compared to the state of the art HgCdTe detector for different figures of merit.

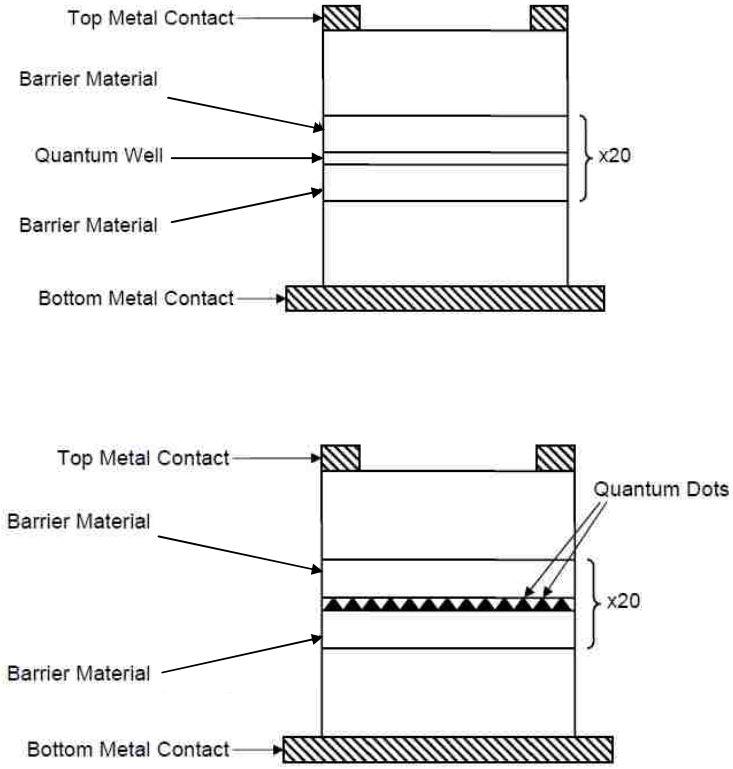

Figure 1.4: (Top) QWIP structure and (Bottom) QDIP structure

Figure 1.5: Images taken with a dual band QWIP FPA [2]. The left image shows the scene in the MW and the right image shows the same scene in the LW.

Detector	**QE**	***D****	**NEDT**
HgCdTe	≥70% at 77K	~10^{12} cmHz$^{1/2}$W^{-1} at 77K	10 mK
InAs-GaSb SLS	52% at 77K	~10^{11} cmHz$^{1/2}$W^{-1} at 70K	23.8 mK at 77K
QWIP	≤ 10% at 70K	~10^{11} cmHz$^{1/2}$W^{-1} at 70K	33 mK at 70K
QDIP	≤ 3%	~10^{10} cmHz$^{1/2}$W^{-1} at 77K	40 mK at 60K
Micro-bolometer	N/A	~10^{8} cmHz$^{1/2}$W^{-1} at 77K	200 mK

Table 1.1: Comparison of figures of merit in various mid-IR detectors [1, 2, 9, 11]

1.2 Motivation of dissertation

Multispectral (MS) and hyperspectral (HS) infrared (IR) sensing continues to be a pivotal tool in remote sensing. The role of MS/HS sensing in a wide spectrum of applications has been increasing with advancements in sensor technology as well as data-processing and interpretation techniques. MS/HS sensing systems offer spectral information of a scene (target or an agent) in a spectral band by sensing a wide range of narrow segments of the IR spectrum in a spectral range of interest. Conventionally, this is realized through either multiple IR detectors, each sensing at a specific range, or a single broadband IR detector integrated with dispersive optics or some sort of an "optical filter wheel," where each filter admits a single IR spectral band. However, this conventional approach yields sub-systems that can be bulky and often expensive due to the complexity of their optical systems.

In recent years, spectrally multicolor detectors have been emerging as a highly desirable alternative to conventional MS/HS sensing strategies. Such alternative sensing systems feature simplicity through their single-detector nature (or array of identically fabricated detectors) without requiring dispersive elements. In this direction, a new class of IR photodetectors, based on epitaxial quantum dots (QDs) have recently been proposed and developed. A key feature of this detector is that it exploits intersubband transitions between quantum-confined energy levels in a self-assembled dots-in-a-well (DWELL) structure in which QDs are embedded in a quantum well as shown in Fig. 1.6 (a). Advantages of this detector technology are operating wavelength tailoring [17,20], sensitivity to normally incident radiation [17,20], increased carrier lifetime [17,20], and notably electrically controlled spectral tunability [17,20]. The quantum-confined Stark effect (QCSE) [18,19] in the DWELL structure results in a bias-dependent spectral response and also introduces a spectral shift with significant spectral overlap by varying the applied bias voltage, as shown in Fig. 1.6 (b). This property leads to greater optical simplicity as the spectral response is tuned electrically rather than optically. Hence, a single DWELL photodetector can be thought of as a MS detector albeit with overlapping spectral bands.

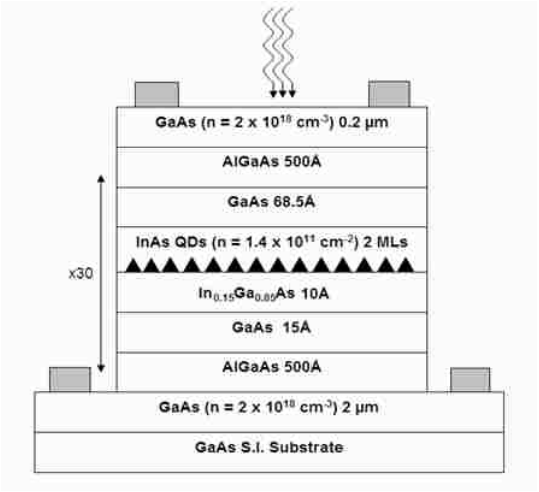

(a)

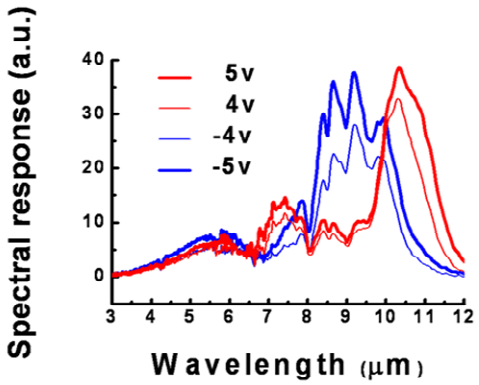

(b)

Figure 1.6: (a) Growth schematic of the DWELL heterostructure (left) and cross-sectional transmission electron microscopy image of active region (right). (b) Bias-tunable spectral bands of the DWELL photodetector for various applied bias voltages ranging from -5 to 5 V.

Now the overlapping nature of the spectral responses results in significant redundancy in the sensed data when a large set of biases is used to produce a set of spectral data. Nonetheless, despite the redundancy present in the data resulting from sensing at different biases, each bias brings new spectral information that is buried by the redundant portion of the data. Meanwhile, the DWELL's spectral response at any applied bias, as shown in Fig. 1.6 (b), is not sufficiently narrow ($\geq$2 μm) for use in high resolution MS/HS sensing applications without the aid of spectral filters. Hence, to extract the detailed spectral information amidst spectrally rich yet redundant data, we need to develop signal-processing algorithms that can deconvolve the spectral overlap and redundancy in the sensed data.

Along these lines, the main question that we should ask is whether we can develop post-processing algorithms that employ data from a large set of (or even from a continuum of biases, in principle) of spectrally overlapping bands of the DWELL, one for each applied bias, to perform applications that require high spectral resolution. And, can we identify a substantially reduced set of sensing biases that can perform equally well without wasting acquisition time on redundant data? The benefit of such a hybrid algorithmic-hardware approach is that it enables us to perform spectral sensing for applications that require spectral resolutions beyond that offered by the raw DWELL detector without the need for spectral filters. This dissertation aims to address these two questions, both theoretically and experimentally.

1.3. An integrated algorithm-hardware approach for spectral sensing

1.3.1 Prior work

To enhance the spectral resolution of the DWELL beyond what is available at each fixed applied bias, the bias-dependent spectral tunability of the DWELL was exploited and the novel multi-bias modes of sensing through post processing were explored. In recent years, our group has reported post-processing algorithms that offer two functionalities beyond those offered by the single-bias mode of the DWELL. The underlying idea is to sense an object of interest repeatedly at multiple applied biases and then form a linear superposition of the bias-dependent photocurrents (i.e., the bias-dependent detector outputs) according to pre-calculated weights that are designed for specific MS sensing tasks, such as narrow-band spectral filtering, spectroscopy and spectral matched filtering among other tasks. Below are the qualitative descriptions of algorithmic sensing methodologies.

The first algorithm, termed spectral tuning [21-24], allows performing algorithmic spectrometry, which is capable of reconstructing the transmittance of target of interest without utilizing any physical optics or spectrometer. Specifically, for an arbitrarily specified narrowband tuning filter, the algorithmic spectral-tuning technique yields an optimal set of weights that can be used to add the bias-dependent spectral responses of the DWELL. The resulting superposition spectral response is the best approximation of

the desired shape of the specified narrowband tuning filter. The bandwidth of the tuning filter can be as narrow as 0.5 μm, which is less than one fourth of the DWELL's bandwidth. A reconstruction of a target's transmittance at each wavelength is then obtained by forming a weighted linear superposition of bias-dependent photocurrents. Such "superposition photocurrent" represents the best approximation of the ideal photocurrent that would be obtained if we were to use a broadband detector to probe the same target of interest through a physical narrowband spectral filter. The entire procedure is repeated for other tuning wavelengths within the spectral regions of interest to complete the spectral reconstruction of the arbitrary unknown target.

The second algorithm, termed spectral matched-filtering [25,26], is also based upon a similar principle of forming a superposition. However, the objective is to perform target classification instead of spectral reconstruction. Specifically, for a known transmittance (representing a class of targets of interest), the spectral matched-filtering technique finds an optimal set of weights to be used to form a weighted superposition of the DWELL's bias-dependent spectral responses approximating the transmittance of interest. Such superposition response can be represented as the most "informative direction" for a given target's transmittance in the presence of noise. A matched-output for the target's transmittance is obtained by forming a weighted linear superposition of the bias-dependent photocurrents. The superposition photocurrent represents the best approximation of the ideal photocurrent that would be obtained if we were to use a broadband detector through a spectral filter that is matched to the target's transmittance. Both algorithms accommodate the noise characteristics (SNRs) of the DWELL's photocurrents to minimize the noise accumulation in a superposition process. While both algorithms were formulated earlier [21-26], the principles have not been demonstrated in conjunction with the DWELL photodetectors heretofore nor have they been generalized for versatile spectral sensing with minimal number of biases, as done in this dissertation.

1.3.2. Contributions of this dissertation

This dissertation presents the first demonstration of the spectral tuning algorithm using the spectrally tunable DWELL photodetector. The experimental results show that it is possible to reconstruct the spectral content (transmittance or reflectance) of a target electronically without using any dispersive optical elements for tuning, thereby demonstrating a DWELL-based algorithmic spectrometer (DAS) [27-29]. (Later, the DAS was also successfully demonstrated by an other research group at the University of Sheffield, UK [30].)

To generalize both spectral tuning and spectral matched-filtering for near real-time implementation, this dissertation presents a new generalized data-compressive spectral sensing algorithm [31] with the DWELL photodetector to substantially compress the number of necessary biases, and hence the amount of data to be sensed, subject to a prescribed performance level across multiple sensing applications. In essence, the algorithm identifies a minimal set of data-acquisitions to capture only the relevant spectral information for multiple remote-sensing applications of interest. As a result, this new algorithm can substantially reduce the required data-acquisition time. The algorithm is demonstrated for target spectrometry and classification. Note that the selection of suitable biases and the photocurrent weights must be done with the bias-dependent SNR of the detector in mind due to the noise accumulation in superposition process.

The example shown in Fig. 1.7 demonstrates the use of minimal biases that are judiciously selected by the generalized data-compressive spectral-sensing algorithm for spectral filter approximation. Minimum of four biases out of a total of 30 biases were selected, yielding a significant data-reduction in the required number of biases by a factor of 7.5. As shown in Fig. 1.7 (blue), the approximations of various types of specified spectral filters using minimal four biases are uniformly accurate. Also the approximations using minimal four biases are comparable to those using all 30 biases shown in Fig. 1.7 (red). Thus, the use of minimal biases does not sacrifice the performance of algorithm.

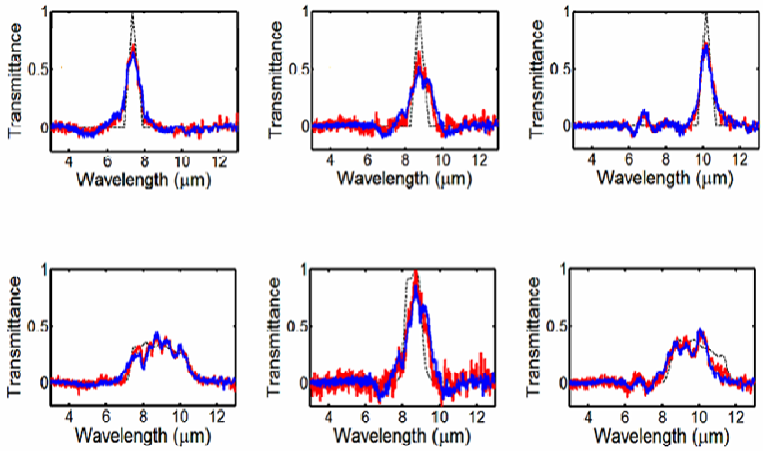

Figure 1.7: The data-compressive spectral-sensing algorithm is used to approximate the specified spectral-filter collection: (top row) hypothetical narrowband triangular sensing filters and (bottom row) spectral matched filters using only minimal four biases out of total 30 biases. The successful approximations using minimal four biases are shown in blue, which corresponds to the error metric 6.7% as compared to the approximations using all 30 biases shown in red [31].

Generalizing the concept of sensing sequentially at different biases and forming a weighted superposition of the detector's photocurrents, this dissertation also investigates optimal biasing the detector, within a fixed integration time, using a continuously varying bias. This is especially relevant when it is desirable to extract the most relevant spectral information in a limited integration time. The basic question here is what is the optimal time-varying bias within the integration time that enables the sensor to gather the most relevant spectral information for a specific sensing application? Clearly, when the waveform is restricted to a piece-wise constant form, this approach reduces to the DAS. We particularly emphasize this modality of spectrally agile sensing is most relevant for focal-plane arrays (FPAs), for which integration time can be a constraint imposed by the readout circuit. Note that as in the case of the DAS, here too the SNR considerations must be taken into account, with the added complexity that changing shape and values of the bias waveform within the integration time affects the instantaneous SNR.

1.4 Organization of the dissertation

The organization of this dissertation is as follows. Demonstration of the DWELL-based algorithmic spectrometer is presented in Chapter 2. The MS classification capability of tunable DWELL FPA is demonstrated in Chapter 3. A new data-compressive MS sensing paradigm, based upon the tunable DWELL photodetector, is presented in Chapter 4. Chapter 5 presents the sensitivity analysis of data-compressive MS sensing algorithm for hardware implementation. In Chapter 6, theory and simulations are presented to define the acquisition-time/data-volume constraints to optimally solve a specific sensing problem for potential use in FPAs.

1.5 Publications resulting from the dissertation

The selected publications related to this dissertation include 1 US patent, 9 peer-reviewed publications and 12 conference papers.

Patent

1. S. Krishna, M. M. Hayat, J. S. Tyo and **W-Y. Jang**, "Infrared Retina," US 8,071,945 B2, 2011.

Peer-reviewed publications

1. **W-Y. Jang**, M. M. Hayat, P. Zarkesh-ha and S. Krishna, "Continuous time-varying biasing approach for spectrally tunable infrared detectors," *Optics Express*, 2012 (in preparation).
2. **W-Y. Jang,** M. M. Hayat, S.E. Godoy, S. C. Bender, P. Zarkesh-ha and S. Krishna, "Data compressive paradigm for generalized multispectral sensing using tunable DWELL mid-infrared detectors," *Optics Express*, Vol. 19, No. 20, 19454-19472, 2011.
3. **W-Y. Jang**, B. Paskaleva, M. M. Hayat and S. Krishna, "Spectrally Adaptive Nanoscale Quantum Dot Sensors," *Wiley Handbook of Science and Technology for Homeland Security*, 2009.
4. **W-Y. Jang**, M. M. Hayat, J. S. Tyo, R. S. Attaluri, T. E. Vandervelde, Y. D. Sharma, R. Shenoi, A. Stintz, E. R. Cantwell, S. C. Bender, S. J. Lee, S. K. Noh and S. Krishna, "Demonstration of Bias-Controlled Algorithmic Tuning of Quantum Dots in a Well (DWELL) MidIR Detectors," *IEEE Journal of Quantum Electronics*, Vol. 45, No. 6, 674-683, 2009 **(Citations = 14, source: Google scholar)**.
5. B. Paskaleva, **W-Y. Jang**, S. C. Bender, Y. D. Sharma, S. Krishna and M. M. Hayat, "Multispectral Classification with Bias-tunable Quantum Dots-in-a-Well Focal Plane Arrays," *IEEE Sensors Journal*, Vol. 11, No. 6, 1342-1351, 2011.
6. P. Vines, C. H. Tan, J. P. R. David, R. S. Attaluri, T. E. Vandervelde, S. Krishna, **W-Y. Jang** and M. M. Hayat, "Versatile Spectral Imaging With an Algorithm-Based Spectrometer Using Highly Tuneable Quantum Dot Infrared Photodetectors," *IEEE Journal of Quantum Electronics*, Vol.47, No. 2, 190-197, 2011.

7. J. Andrews, **W-Y. Jang**, J. E. Pezoa, Y. D. Sharma, S. J. Lee, S. K. Noh, M. M. Hayat, S. Restaino, S. W. Teare and S. Krishna, "Demonstration of a Bias Tunable Quantum Dots in a Well Focal Plane Array," *the Infrared Physics & Technology Journal*, Vol. 52, Issue 6, 380-384, 2009.
8. S. J. Lee, Z. Ku, A. Barve, J. Montoya, **W-Y. Jang**, S. R. J. Brueck, M. Sundaram, A. Reisinger, S. Krishna and S. K. Noh, "A Monolithically Integrated Plasmonic Infrared Quantum Dot Camera," *Nature Communications*, 2, 286, 2011.
9. J. R. Andrews, S. R. Restaino, S. W. Teare, Y. D. Sharma, **W-Y. Jang**, T. E. Vandervelde, J. S. Brown, A. Reisinger, M. Sundaram, S. Krishna and L. Lester, "Comparison of Quantum Dots-in-a Double-Well and Quantum Dots-in-a-Well Focal Plane Arrays in the Long Wave Infrared," *IEEE Transactions on Electron Devices*, Vol. 58, Issue 7, 2022-2027, 2011.

Conference papers

1. **W-Y. Jang**, M. M. Hayat, S.E. Godoy, P. Zarkesh-ha, S. C. Bender and S. Krishna, "Compressive Multispectral Sensing Algorithm with Tunable Quantum Dots-in-a-Well Infrared Photodetectors," *IEEE Photonics 2011 Conference (IPC11)*, 9-13 October, 2011.
2. **W-Y. Jang**, M. M. Hayat, B. S. Paskaleva and S. Krishna, "Enhanced Efficiency and Functionality of Algorithmic Multispectral Sensing using Tunable Dwell-Based MidIR Detectors," *the 23rd Annual Meeting of the IEEE Photonics Society Volume*, 708-709, 2010.
3. **W-Y. Jang**, M. M. Hayat, B. Paskaleva, S. C. Bender, P. Vines, C. H. Tan and S. Krishna, "Compressive Algorithmic Spectrometry based on Tunable Quantum Dots-in- a-well Detectors," *International Symposium on Spectral Sensing Research (ISSSR)*, June 21-24th, 2010, Springfield, Missouri, USA.
4. **W-Y. Jang**, S. Krishna, M. M. Hayat, S. C. Bender and B. S. Paskaleva, "Tunable Infrared Imaging Sensors," *National Consortium of MASINT Research (NCMR) Technology Fair*, December 15th, 2009, Washington, D.C, USA.
5. **W-Y. Jang**, B. S. Paskaleva, M. M. Hayat, S. C. Bender and S. Krishna, "Multispectral Classification with Bias-tunable Quantum Dots in a Well Focal Plane Array," *the 22nd Annual Meeting of the IEEE Photonics Society Volume*, 168-169, 2009.

6. **W-Y. Jang**, J. E. Pezoa, Y. D. Sharma, S. J. Lee, S. K. Noh, M. M. Hayat and S. Krishna, "Demonstration of a Bias Tunable Quantum Dots in a Well Focal Plane Array," *Quantum Structure Infrared Photodetector (QSIP) International Conference*, January 18-23rd, 2009, Yosemite, California, USA.
7. **W-Y. Jang**, M. M. Hayat, S. Bender, Y. D. Sharma, J. Shao and S. Krishna, "Performance enhancement of an algorithmic spectrometer with quantum-dots-in-a- well infrared detectors," *International Symposium on Spectral Sensing Research (ISSSR)*, June 23-27th, 2008, Hoboken, New Jersey, USA **(received the Best Presentation Student Award)**.
8. **W-Y. Jang**, R. S. Attaluri, S. Annamalai, M. M. Hayat, J. S. Tyo and S. Krishna, "Development of an algorithmic spectrometer for target recognition using quantum-dot infrared sensors," *Nanoelectronic Devices for Defense & Security conference (NANO- DDS)*, June 18-21st, 2007, Crystal City, Virginia, USA.
9. P. Zarkesh-Ha, **W-Y. Jang**, P. Nguyen, A. Khoshakhlagh and J. Xu, "A Reconfigurable ROIC for Integrated Infrared Spectral Sensing," *the 23rd Annual Meeting of the IEEE Photonics Society Volume,* 714-715, 2010.
10. C. H. Tan, P. Vines, J. P. R. David, R. S. Attaluri, T. E. Vandervelde, S. Krishna, **W-Y. Jang** and M. M. Hayat, "Spectrally Tunable Quantum Dot Detectors: Implementation of an Algorithm-Based Spectrometer," *the 23rd Annual Meeting of the IEEE Photonics Society Volume*, 706-707, 2010 (Invited).
11. P. Vines, C. H. Tan, J. P. R. David, R. S. Attaluri, T. E. Vandervelde, S. Krishna, **W-Y. Jang** and M. M. Hayat, "Quantum dot infrared photodetectors with highly tunable spectral response for an algorithm-based spectrometer," *Infrared Technology and Applications XXXVI*, *Proceedings of SPIE*, Vol. 7660, 2010.
12. P. Vines, C. H. Tan, J. P. R. David, R. S. Attaluri, T. E. Vandervelde, S. Krishna, **W-Y. Jang** and M. M. Hayat, "Low Strain Multiple Stack Quantum Dot Infrared Photodetectors for Multispectral and High Resolution Hyperspectral Imaging," *the 22nd Annual Meeting of the IEEE Photonics Society Volume*, 166-167, 2009.

Chapter 2

Demonstration of Bias-controlled Algorithmic Spectrometry using Quantum Dots-in-a-well (DWELL) Photodetectors

In this chapter, we first review germane aspects of the operation principle and characterization of the DWELL single pixel device. We then show the experimental demonstration of the concept of DWELL-based algorithmic spectral tuning and further develop an algorithmic spectrometer. The performance of the DWELL-based algorithmic spectrometer (DAS) is examined taking into account issues such as sensitivity to bias selection, dark current and detector temperature.

2.1 Device concept and characterization of DWELL photodetectors

A DWELL photodetector is a clever hybrid of conventional QW and QD infrared photodetectors. In a representative DWELL heterostructure InAs QDs are embedded in InGaAs/GaAs multiple QW structures as shown in Fig. 2.1. Electrons in the ground state of QD are promoted to a set of bound states within the QW by photoexcitation. Altering the QW thickness of the DWELL detector alters the nature of the allowable energy transitions (bound-to-bound, bound-to-quasi-bound, and bound-to-continuum) as shown in Fig. 2.2 (a), thereby altering the DWELL's operating wavelengths as shown in Fig 2.2 (b). These energy transitions enable the detection of photons from MWIR to VLWIR within a single detector. Moreover, a bias-dependent spectral response is also observed in DWELL detectors due to the QCSE. The asymmetric geometry of the electronic potential, due to the shape of the dot and the different thicknesses of QW above and below the dot, results in variation of the local potential as a function of the applied bias as shown in Fig. 2.3. From these measurements, one

can observe the bias-dependent multicolor capability of the DWELL detector structure. As a result, in the context of MS sensing, a single DWELL detector can be operated as multiple detectors, obviating the need of optical systems, offering on-demand electronically controlled agility.

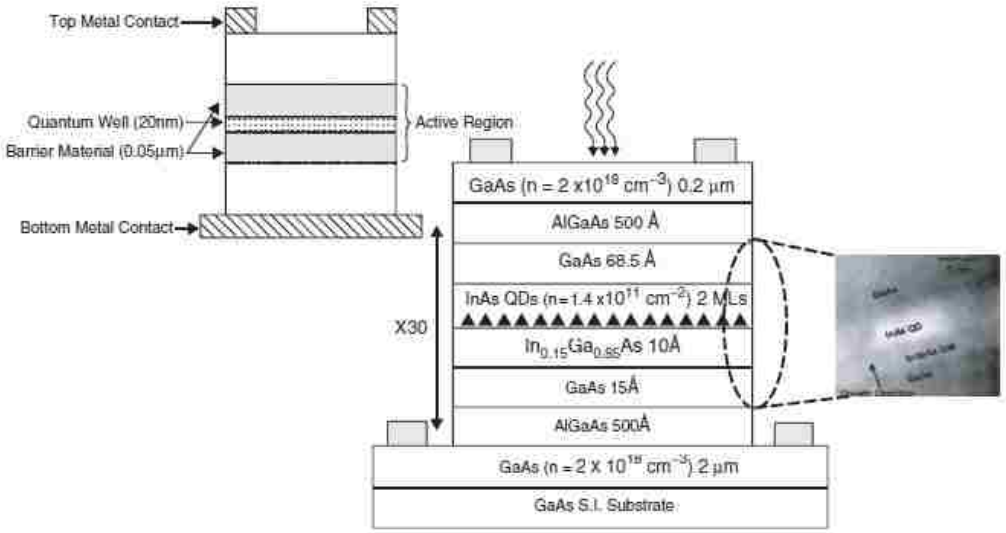

Figure 2.1: General schematic of the DWELL heterostructure (top, left), example of the DWELL growth schematic (middle) and cross-sectional transmission electron microscopy (TEM) image (right) [27].

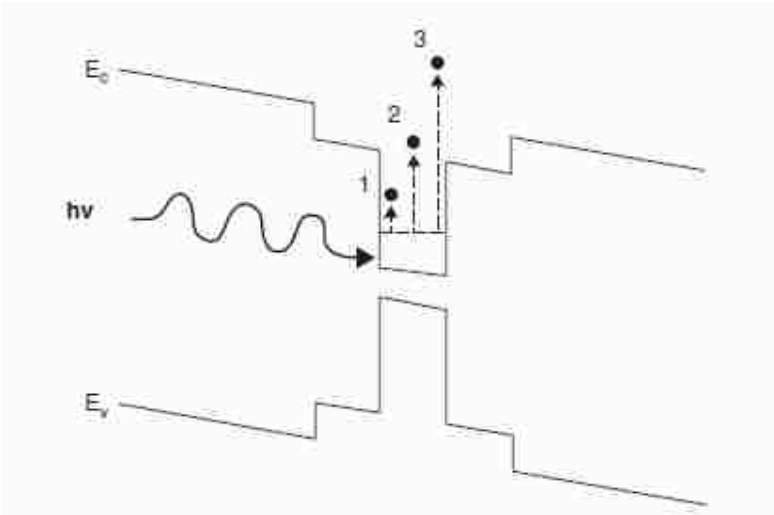

(a)

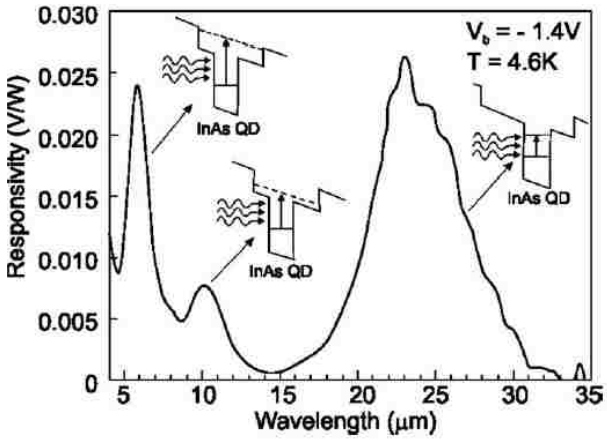

(b)

Figure 2.2: (a) DWELL energy band diagram describing: (1) bound-to-bound, (2) bound-to-quasibound, and (3) bound-to-continuum transitions [27]. (b) Operating-wavelength tailoring by the DWELL structure: the MWIR (LWIR) peak is possibly a transition from a state in the dot to a higher (lower) lying state in the well, whereas the VLWIR response is possibly from two quantum-confined levels within the QD [2].

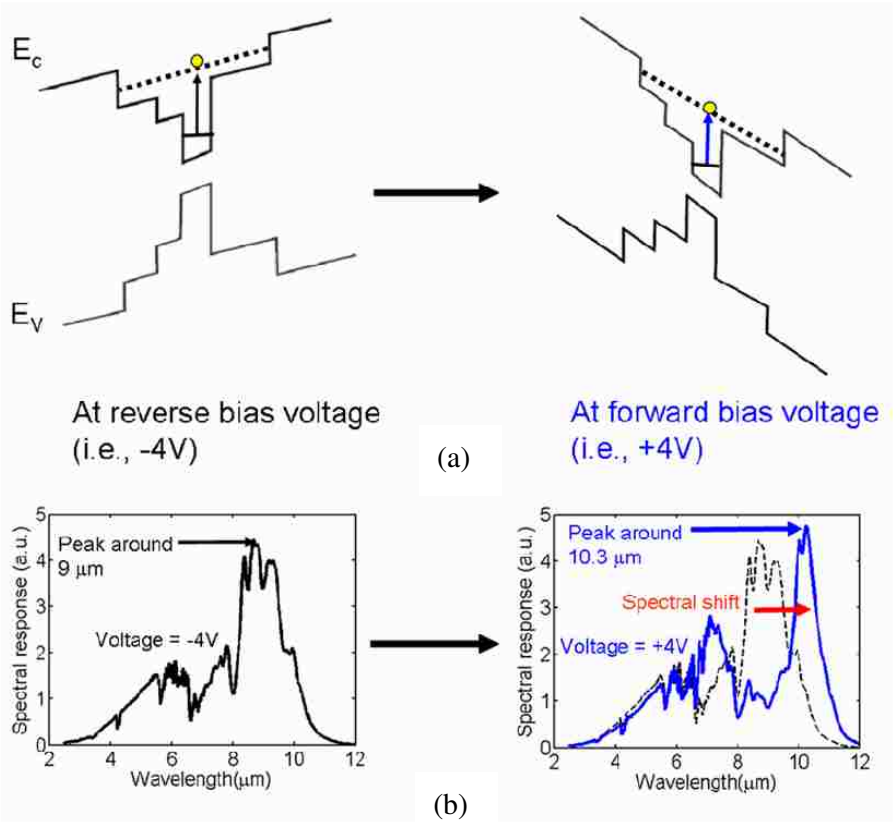

Figure 2.3: (a) Band diagram and (b) spectral tunability of the DWELL MidIR photodetector as a function of electrically applied bias voltages.

Spectral response measurements were performed for the DWELL photodetectors using a Nicolet 870 Fourier Transform Infrared (FTIR) spectrometer and a Keithley 428 current amplifier, which controls the electrical bias voltage to the detectors. Experimental photocurrents and dark currents were also taken at different biases. The characterization setup is shown in Fig. 2.4.

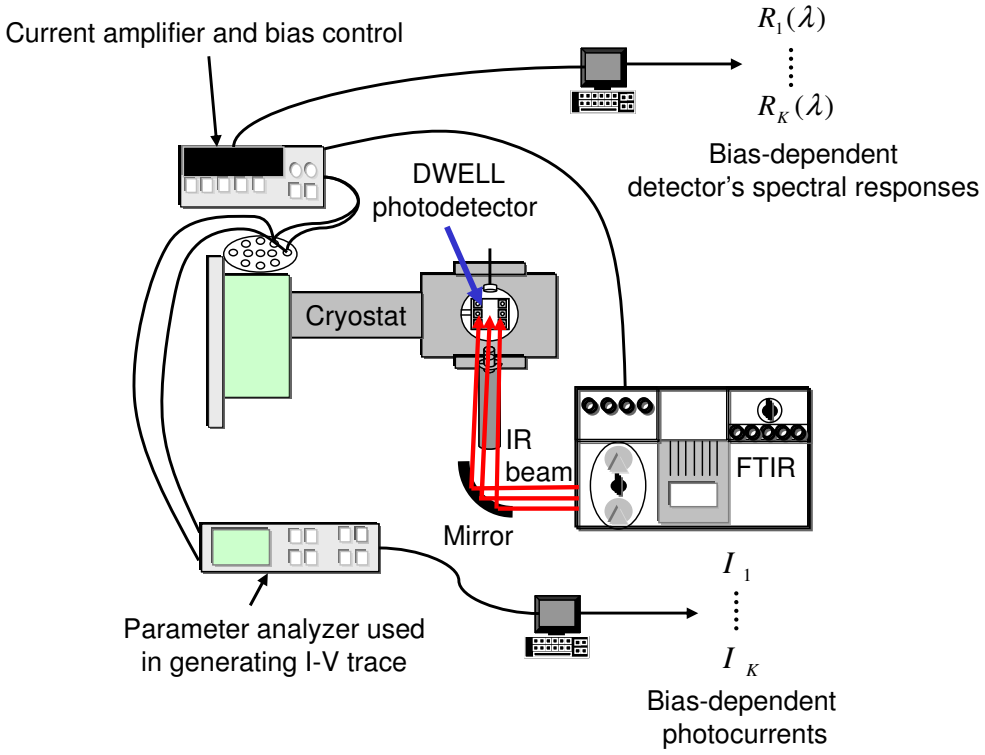

Figure 2.4: Experimental setup for device characterization

Bias-dependent spectral responses of the DWELL-1780 photodetector measured at a device temperature of 30 K are shown in Fig. 2.5, which illustrates the multicolor attribute of the DWELL in the LWIR range. Figure 2.5 also demonstrates photocurrent characteristic measured from a DWELL photodetector at different biases. A spectral shift with significant overlaps was observed from the peak wavelength of 8.5 μm with negative bias voltage to 10 μm with positive bias voltage. This demonstrates that a DWELL single photodetector can simply serve as a multicolor detector as a series of the bias voltage based spectral tunability. The spectral measurements of the optimized DWELL-1781 are illustrated in Fig. 2.6. There are two distinct peaks at LWIR region observed, one in about 9.5 μm and the other in 10.5 μm. Improvement in the performance was evident showing shifts in the operating wavelengths. The peak

operating wavelengths for negative biases shift from 8.5 μm (in DWELL-1780) to 9.5 μm (in DWELL-1781) and for positive biases they shift from 10 μm (in DWELL-1780) to 10.5 μm (in DWELL-1781). This red shift is due to the lowering of the quantum well state in the heterostructure.

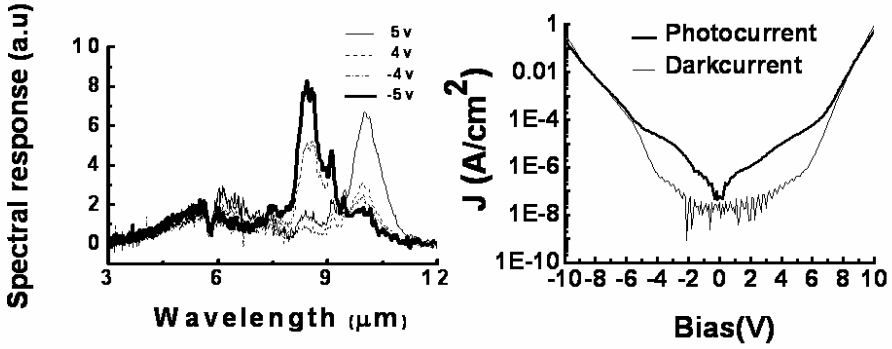

Figure 2.5: (Left) Bias-dependent DWELL-1780's spectral responses at 30 K. (Right) Photocurrent and darkcurrent characteristics obtained from a detector at different bias voltages [28].

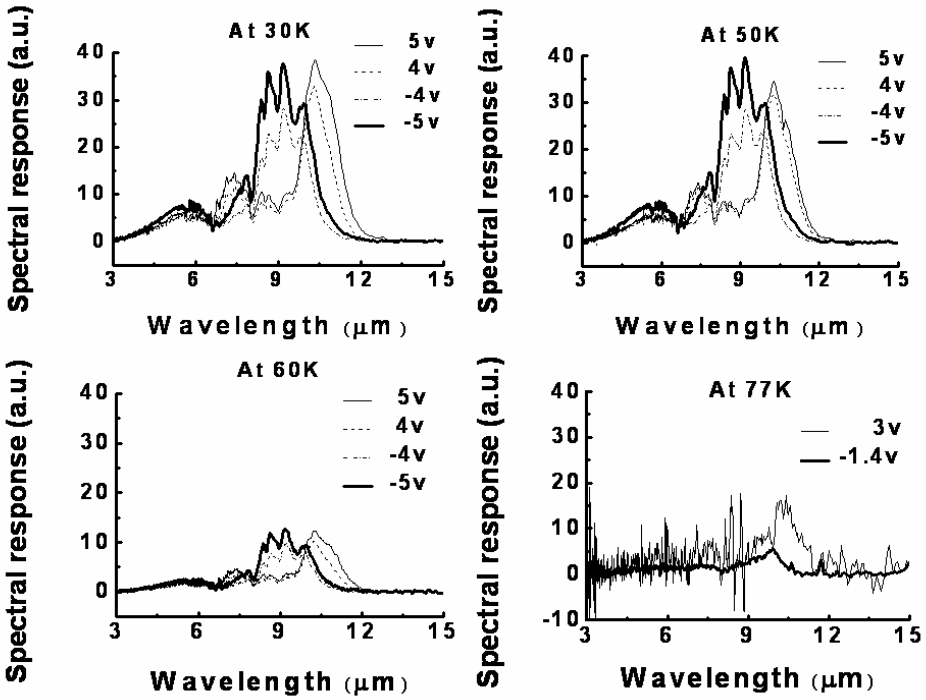

Figure 2.6: Bias-dependent spectral responses of DWELL-1781 as a function of a number of operating temperatures at 30 K (top, left), 50 K (top, right), 60 K (bottom, left), and 77 K (bottom, right) [28].

The limitation of the DWELL's operating temperature was observed due to higher dark current levels at higher device temperatures. Figure 2.6 shows the bias-dependent

spectral responses for various device operating temperatures. It is to be noted that the performance of DWELL-1781 begins to degrade dramatically as device operating temperature exceeds 60 K. At 77 K, noise dominates the spectral measurements and almost no spectral variation is observed for any bias.

As shown in Fig. 2.6, the DWELL photodetectors exhibit a high level of spectral redundancy due to their highly overlapping spectral responses as a function of bias. Also the DWELL's spectral response is too wide for high spectral resolution applications. To remedy these two drawbacks, we developed a post-processing algorithm which can reduce the redundancy by projecting the DWELL's spectral responses into a new low-dimensional function space that is capable of extracting high-resolution spectral information. The next section presents a post-processing algorithm that exploits the bias-dependent spectral tunability of DWELL to perform spectral sensing for spectrometry application.

2.2 DWELL-based algorithmic spectrometer (DAS)

In this section, we review germane aspects of the spectral-tuning algorithm theoretically developed by Sakoglu *et al*. [21-24]. This algorithm is then to be used in conjunction with the bias-tunable DWELL detector in producing the DAS.

We assume that an unknown object is probed repeatedly by the DWELL detector, each time using a different operating bias voltage, resulting in a set of bias-dependent photocurrents. The photocurrent vector represents the bias-driven MS signature vector of the object as seen by the DWELL photodetector operated at the prescribed bias set. The idea of an algorithmic spectrometer is to utilize these bias-dependent photocurrents to construct an approximation of the transmittance spectrum of the object of interest without using any physical spectrometer or optics. The implementation of algorithmic spectrometer is described as follows. First, a hypothetical narrowband tuning filter is selected with a specified center (tuning) wavelength and a specified full-width at half-maximum (FWHM) linewidth. Next, a set of weights, one for each operating bias voltage, is obtained through the use of the projection algorithm as illustrated in Fig. 2.7. These weights have the property that once used to form a weighted linear superposition of the DWELL's bias-dependent spectral responses, the resulting superposition spectral response best approximates the hypothetical tuning filter. Next, the bias-dependent photocurrents are linearly combined using the same weights, yielding an approximation

of the target's spectrum at the prescribed tuning wavelength. This superposition termed the "synthesized photocurrent" represents the reconstructed transmittance of object seen through the approximated narrowband tuning filter without any information about object of interest. The reconstruction of the transmittance spectrum of object is completed by repeating the earlier procedure for other tuning wavelengths as illustrated in Fig. 2.8.

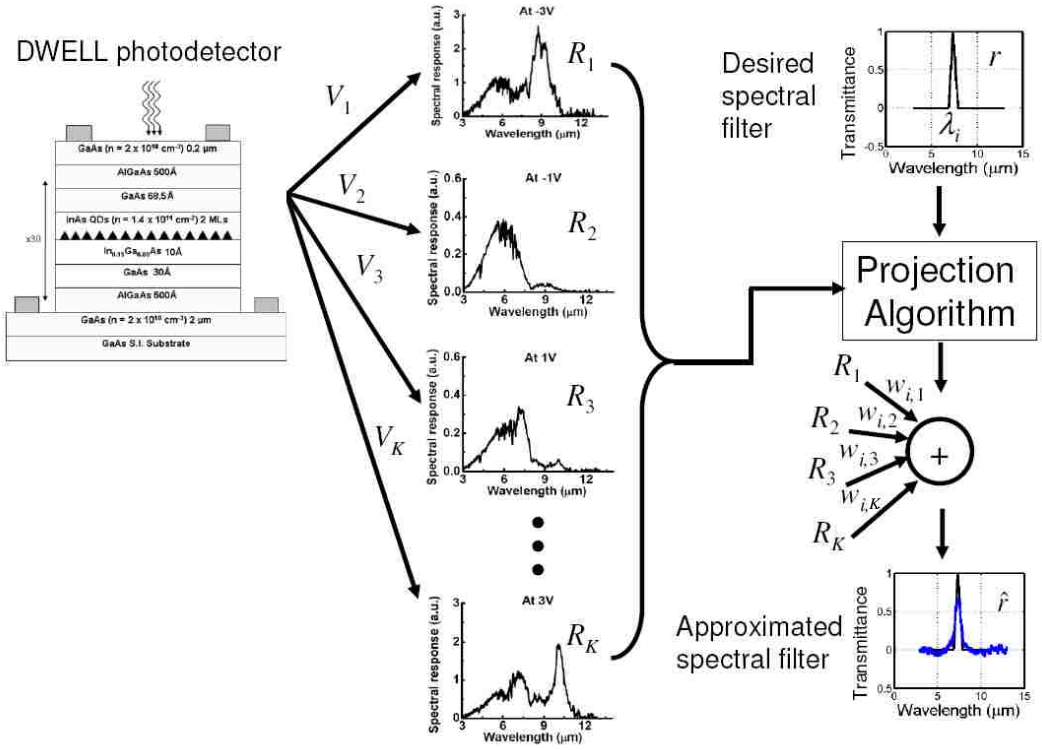

Figure 2.7: Illustration of the projection step in the algorithmic MS sensing. Desired shape of transmittance of narrowband tuning filter is approximated by forming a weighted linear superposition of the DWELL's bias-controlled spectral responses.

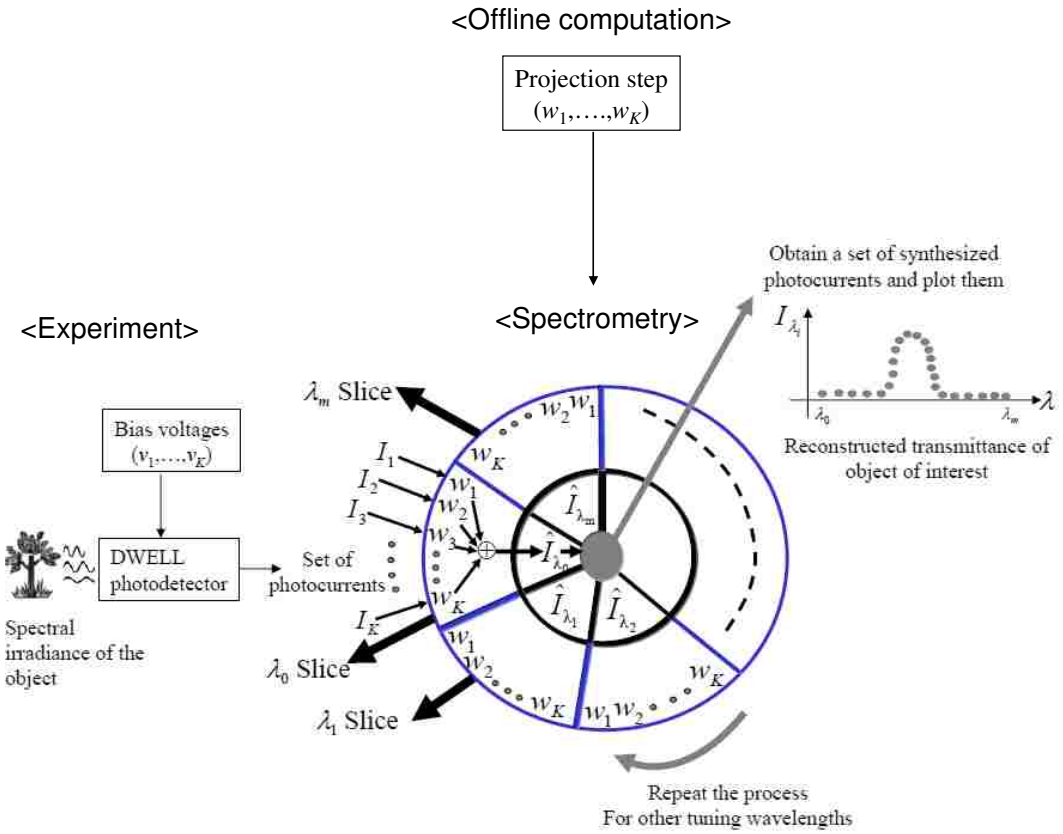

Figure 2.8: Illustration of the spectrometry step in the algorithmic MS sensing. The reconstructed transmittance of object is obtained by forming a weighted linear superposition with a set of DWELL's photocurrent measurements.

2.2.1 Review of the spectral-tuning algorithm

Consider an arbitrary object-of-interest whose transmittance in the LWIR range is represented by the function $f(\lambda)$. We assume that the object is illuminated by a black-body source. Suppose that a DWELL detector is used to probe the illuminated object using various biases, $v_1,\ldots,v_K$, yielding a set of bias-dependent photocurrents, $I_1,\ldots,I_K$, respectively. Let the detector's spectral response at the i^{th} applied bias be denoted by $R_i(\lambda)$.

Our approach for achieving an algorithmic spectrometer can be described as follows. Imagine an *ideal* (and hypothetical) narrowband LWIR tuning filter centered at wavelength λ_n and with transmittance function $r(\lambda;\lambda_n)$. (In a conventional spectrometer, as schematically shown in Fig. 2.9 (a), such a filter would be used with a broadband detector to estimate the spectrum of the object-of-interest at wavelength λ_n.) Our earlier

theoretical work [22] provides a method for calculating a set of superposition weights, $w_{n,1},\ldots, w_{n,K}$, which depends upon the choice of $r(\lambda;\lambda_n)$, so that the *synthesized photocurrent*, $\hat{I}_{\lambda_n} \equiv w_{n,1} I_1 + \ldots + w_{n,K} I_K$, best approximates the ideal photocurrent I_{λ_n} that we would have obtained if we were to sense the same target-of-interest f using an ideal broadband (spectrally flat response) detector that is looking at the object through the spectral filter $r(\lambda;\lambda_n)$. The formula for these weights reported by [22] is given as follows. The set of weights, $w_{n,i}$ for center wavelength λ_n, which we compactly write as $\mathbf{w}_n = [w_{n,1}, \ldots, w_{n,K}]^T$, is given by the formula ((18) in [22])

$$\mathbf{w}_n = [\mathbf{A}^T\mathbf{A} + \Phi + \alpha\mathbf{Q}^T\mathbf{A}^T\mathbf{A}\mathbf{Q}]^{-1}[\mathbf{A}^T\mathbf{r}_{\lambda_n}], \qquad (1)$$

where $\mathbf{A} = [\mathbf{R}_1,\ldots,\mathbf{R}_K]$ and $\mathbf{R}_k = [R_k(\lambda_{\min}),\ldots,R_k(\lambda_{\max})]^T$ for $k=1,\ldots,K$, while $\mathbf{r}_{\lambda_n} = [r(\lambda_{\min};\lambda_n),\ldots,r(\lambda_{\max};\lambda_n)]^T$. Here, the wavelengths at which the spectrum is sampled range from a minimum value of $\lambda_{\min}$ to a maximum value of $\lambda_{\max}$. Moreover, Φ is a diagonal *noise-equivalent matrix* whose kth diagonal entry is $\mathbf{R}_k^T\mathbf{R}_k/\mathrm{SNR}_k^2$, where SNR_k is the signal-to-noise ratio of the photocurrent at the kth bias v_k. The regularization term, $\alpha\mathbf{Q}^T\mathbf{A}^T\mathbf{A}\mathbf{Q}$, penalizes spurious fluctuations in the approximation [22]. In this work, the matrix $\mathbf{Q}$ is taken as a Laplacian operator and α is the corresponding regularization weight, which is selected by the user. The approximation is in the sense of minimizing the mean-squared-error (MSE) between the synthesized photocurrent $\hat{I}_{\lambda_n}$ and the ideal response I_{λ_n}. Our earlier theoretical work also teaches us that the same set of weights is characterized as that for which the *superposition spectrum*, $\hat{r}(\lambda;\lambda_n) \equiv w_{n,1}R_1(\lambda) + \ldots + w_{n,K}R_K(\lambda)$, best approximates the imaginary tuning filter $r(\lambda;\lambda_n)$ in the sense of minimizing the wavelength-integrated MSE. Now, if we repeat the above procedure while sweeping the center wavelength λ_n of the narrowband tuning filter r in a specified range of interest, we will obtain, for each center wavelength, an estimate of the spectrum of the source transmittance. Hence, as we sweep across the center wavelength λ_n of our "hypothetical" tuning filter r and apply the superposition procedure described earlier, we will reproduce the transmittance function f, albeit, within the confines of the approximation.

The above concept of an algorithmic spectrometer is schematically shown in Fig. 2.9 (b). After several repetitions for desired tuning centers, $\lambda_1,\ldots,\lambda_m$, say, the set of synthesized outputs $\hat{I}_{\lambda_1},\ldots,\hat{I}_{\lambda_m}$ is generated and regarded as the approximate reconstruction of the spectrum of the target of interest within the prescribed wavelength range. Each reconstructed value $\hat{I}_{\lambda_n}$ of the spectrum of the target-of-interest, at a desired tuning wavelength λ_n, is mathematically expressed as

$$\hat{I}_{\lambda_n} = \sum_{i=1}^{K} w_{n,i} I_i. \tag{2}$$

We reiterate that these synthesized outputs *approximate* those obtained by using an ideal IR detector in conjunction with an *actual* tunable spectral filter shown schematically in Fig. 2.9 (a). Thus, the algorithmic spectrometer shown in Fig. 2.9 (b), which uses no physical spectral filters, is functionally equivalent to the actual spectrometer schematically shown in Fig. 2.9 (a).

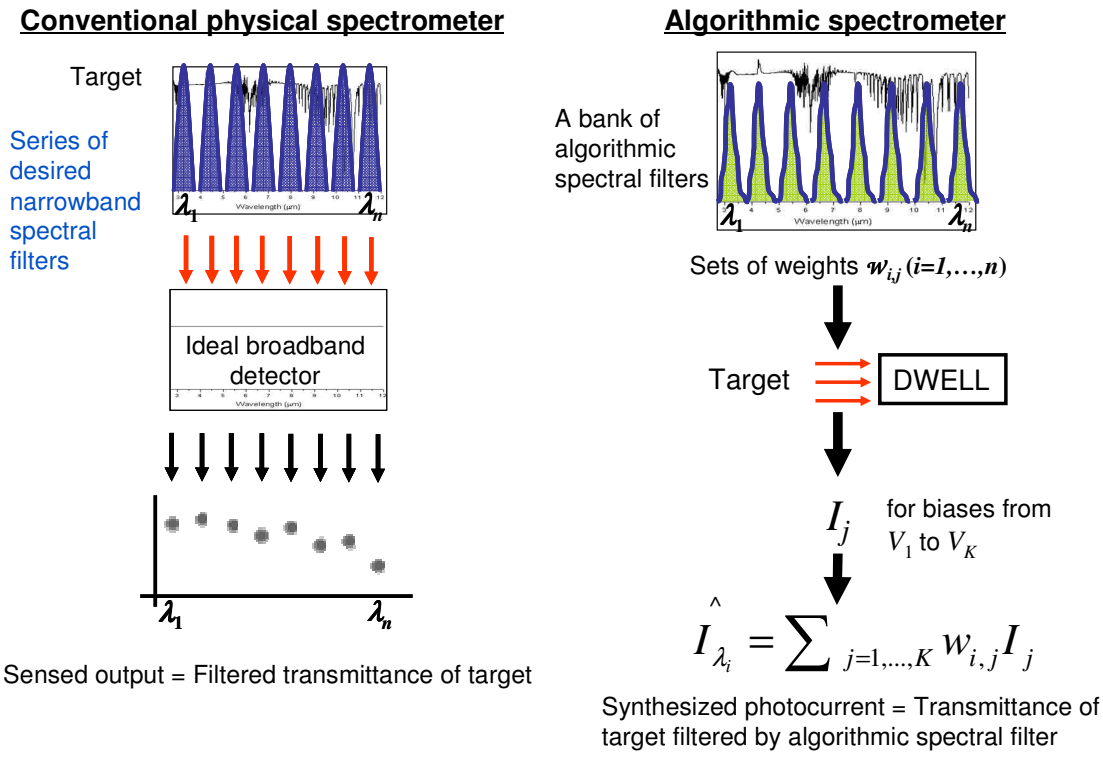

Figure 2.9: (Left) Conventional spectral sensing method using a standard broadband IR detector and a family of optical IR filters. (Right) Proposed algorithmic spectrometer equivalent of (Left). Initially, several photocurrents (of the target spectrum) are taken at different bias voltages $V_1,\ldots,V_K$. Then, the measured photocurrents are algebraically combined with pre-determined weights $w_{i,j}$ that are used to match a desired filter centered at wavelength λ_i. By changing the weights, the effect of different desired filters (similar to the ones used in (left)) is synthesized, albeit, without the use of any optical filters [28].

Before we proceed with the experimental verification of the DAS, we will show a representative example of the superposition tuning filter $\hat{r}(\lambda;\lambda_n)$ that approximates a desired triangular tuning filter with center wavelength of 8.5 μm and a FWHM width of 0.5 μm. The results corresponding to DWELL-1780 are shown in Fig. 2.10 using the bias-dependent spectral responses shown in Fig. 2.5. Note that the initial choice of α=0 (no regularization), shown in Fig. 2.10 (a), yielded a somewhat fluctuating reconstruction, which can be avoided. Much better results are obtained when regularization with α=12 is used, as shown in Fig. 2.10 (b). Generally, if the parameter α is selected too large then the reconstructed spectrum loses resolution; on the other hand, if α is selected too small, then the reconstructed spectrum exhibits spurious fluctuations.

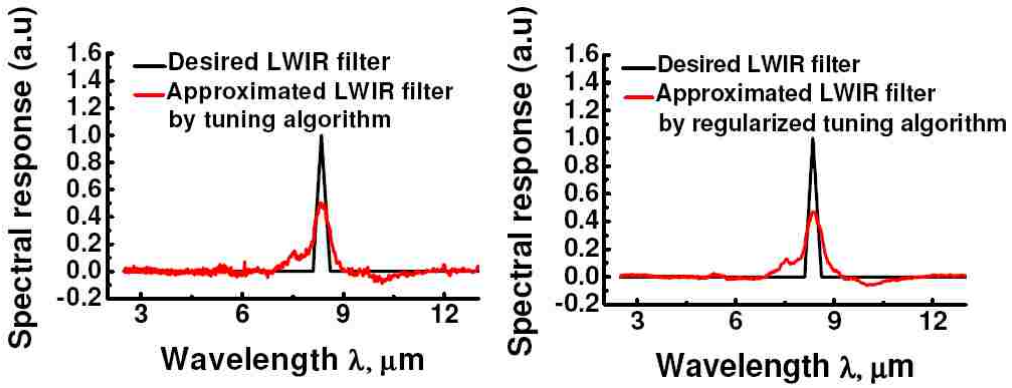

Figure 2.10: Approximation of a desired narrowband LWIR tuning filter by the DWELL-1780 spectra at 30 K shown in Fig. 2.5 with (a) $\alpha = 0$ and (b) $\alpha = 12$ [28].

The 3-D graph in Fig. 2.11 illustrates the desired tuning filter approximations over various tuning wavelengths λ_n ranging from 2.55 μm to 12.25 μm, in steps of 0.05 μm. Good approximations $\hat{r}(\lambda;\lambda_n)$ of $r(\lambda;\lambda_n)$ were observed in LWIR in the range 8–10.5 μm, showing the reconstructed peak regions of the desired tuning filter. However due to the effect of weak spectral responses from DWELL-1780 in the MWIR region (along with atmospheric absorptions), poor approximations in the range 2.55 μm to 7 μm are observed. Also the limitation of tuning filter approximation was evident beyond 11.5 μm because of the lack of spectral responses (contents) by DWELL-1780 in Fig. 2.5 (left). As a result, we anticipate that the DAS with DWELL-1780 can potentially perform well over the range 8–10.5 μm.

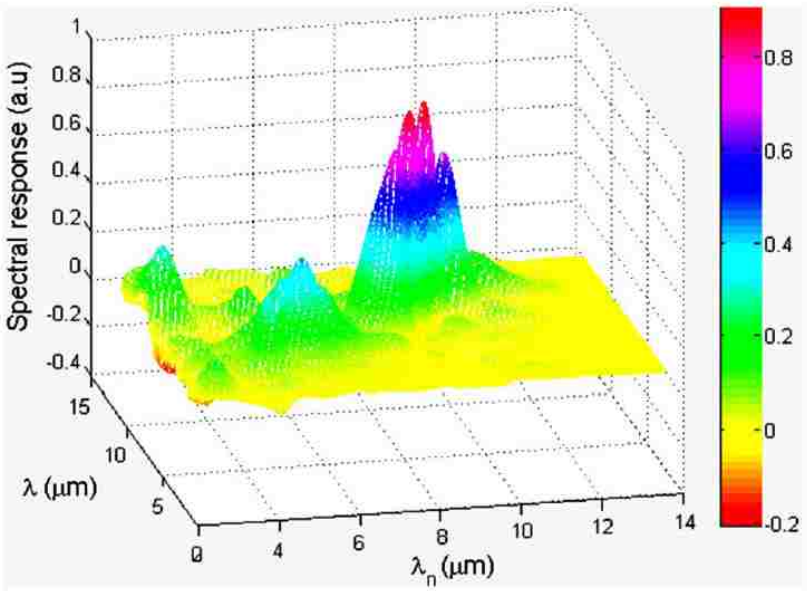

Figure 2.11: Approximation of a desired tuning filter for various tuning wavelengths λ_n (from 2.55 to 12.25 μm) with regularization parameter $\alpha = 12$ [28].

2.2.2 First experimental demonstration of DAS

For the experiments presented here, we considered four different LWIR targets, $f_1(\lambda)$, …, $f_4(\lambda)$, as depicted in Fig. 2.12 (solid curves), with different center wavelengths in the range 8-10 μm and different spectral bandwidths, $\Delta\lambda$=1.0-3.5 μm. The spectral response of the DWELL-1780 detector in Fig. 2.5 (left) was measured at detector operating temperature of 30 K for 82 bias voltages between -5 V and 5 V by using an FTIR spectrometer and a black-body source. Next, for every applied bias the photocurrent and associated dark current were measured for each one of the four targets illuminated by the global source. It is to be noted that in the experiment, the same detector was sequentially biased to generate the bias-dependent spectral response of the DWELL detector.

The SNR at each bias was estimated by utilizing a standard Poisson approximation to model the dark current [24,32] in conjunction with our experimental data for the variance of the dark current. Each quantity SNR_k (corresponding to the k^{th} bias) was calculated using

$$\text{SNR}_k = \frac{y_{p,k}}{\sigma_{N,k}}, \qquad (3)$$

where $y_{p,k}$ is the experimentally averaged photocurrent (over 100 realizations) and $\sigma_{N,k}$ is the standard deviation of the dark current, also calculated empirically from the dark current realizations. This step allows us to determine the noise-equivalent matrix Φ, as shown by (1).

Next, the algorithmic tuning procedure described earlier in Subsection 2.2.1 was followed to calculate the synthesized superposition photocurrents, one for each desired tuning wavelength. We used 195 ideal triangular tuning filters representing $r(\lambda;\lambda_n)$ (with FWHM of 0.5 μm, similar to the one shown in Fig. 2.10), whose center wavelengths range from 2.55 to 12.5 μm in steps of 0.05 μm, and calculated the corresponding weight vectors for each center wavelength according to (1). As a result, 195 synthesized photocurrents are calculated according to (2) yielding a reconstruction of each target spectrum. The best regularization parameter of $\alpha = 12$, was obtained by trial and error and used.

Figure 2.12 shows the experimentally reconstructed spectra from the DWELL-1780 detector (dotted curves) along with the actual spectra of the targets (solid curves). The figure demonstrates two key points. First, the experimental reconstructions of the target spectra are good approximations of their true spectra, validating our approach. Secondly, the limitation of the proposed approach is also evident. For example, the DWELL-1780 detector shown in Fig. 2.5 does not accurately reconstructed the long wavelength edge of target $f_2(\lambda)$ [Fig. 2.12 (b)]. This is due to the lack of response of the DWELL-1780 detector beyond 11.5 μm. It is also observed that peaks in reconstructed spectrum [Fig. 2.12 (a) and (b)] are opposed to actual flat response due to the triangular shape of tuning filter. To remedy this, we can apply the rectangular tuning filter to flatten the reconstruction around peak region.

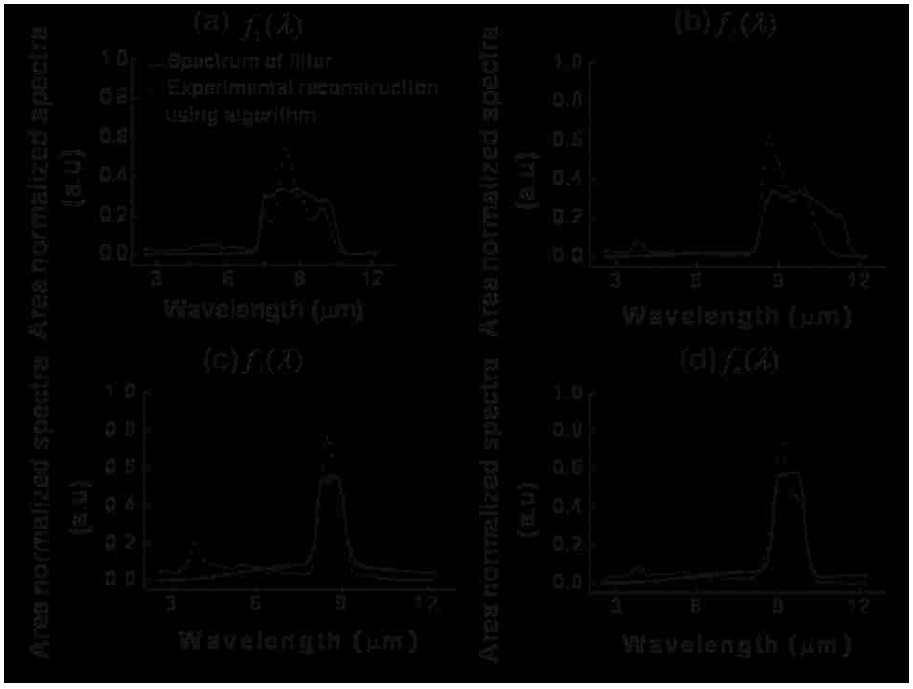

Figure 2.12: Experimental reconstructions using algorithmic spectrometer incorporated with the DWELL detector at 30 K. Solid curves represent the actual responses of the targets and the dotted curves represent the reconstructed spectra using tuning algorithm. (a) $f_1(\lambda)$. (b) $f_2(\lambda)$. (c) $f_3(\lambda)$. (d) $f_4(\lambda)$ [28].

We observe that in general, the algorithmic spectrometer works well for tuning wavelengths in the spectral range (8-12 μm) for which the DWELL's response is strong, as shown in Fig. 2.5. However, as the tuning wavelength is extended beyond 3 μm (toward near IR) or beyond 12 μm (toward very long wavelength IR), the tuning algorithm can no longer reconstruct the tuning filter properly, as seen from Fig. 2.11. This is primarily attributable to the weak response of the DWELL at these extreme wavelengths, as seen in Fig. 2.5. Consequently, we expect the performance of the algorithmic spectrometer to be poor too at these extreme wavelengths. Moreover, the sensitivity to extreme wavelengths is particularly accentuated in cases for which the SNR of the photocurrent is low (<10 dB). Thus, there is a tradeoff between the SNR and the spectral range of the algorithmic spectrometer. We therefore expect DAS to exhibit higher sensitivity to SNR at extreme wavelengths, which, in turn, would require lower operating temperatures. Additional theoretical analysis on tuning limitation is described in [21-24].

2.3 Experimental performance analysis

In previous section, we demonstrated the capability of the proposed DAS (with DWELL-1780) in the spectral sensing various LWIR targets. In this section we study the performance of the DAS (using DWELL-1781) as a function of SNR, detector's temperature variation and bias diversity. Here, we use the DWELL-1781, instead of using DWELL-1780, due to its higher operating temperature, its spectral response at longer wavelengths, and its superior tunability.

We begin by examining the dependence of the DAS performance on the photocurrent's SNR. The spectrum-reconstruction procedure used to generate Fig. 2.12 (c) for the LWIR target $f_3(\lambda)$ was repeated for various levels of the photocurrent's SNR. For each level of the SNR, a scaling factor, ρ, is used to modify the average photocurrent, $y_{p,k}$ uniformly in k, which, in turn, amplifies the photocurrent's SNR according to (3). (The noise variance in (3) is held fixed.) This analysis is useful, for instance, in examining the effect of changing the quantum efficiency of the QDIP on the performance of the algorithmic spectrometer. The results are shown in Fig. 2.13; they show that at high signal-to-noise levels (ρ>1000), the reconstruction of the spectrum $f_3(\lambda)$ is improved compared to the case shown in Fig. 2.12 (c). In particular, the approximation of the passband region is improved while the response in the stopband region is lowered. As ρ is lowered below a critical value of approximately 100, some spurious peaks emerge in the stopband region (3 μm < λ < 6.5 μm). The performance degrades slightly as ρ is lowered below 100 down to 0.1. Finally, for very poor SNRs, i.e., ρ< 0.1, the performance becomes poor in that the passband region (8-9 μm) becomes almost flat and the spurious peaks in the stopband region (3-4 μm) become amplified.

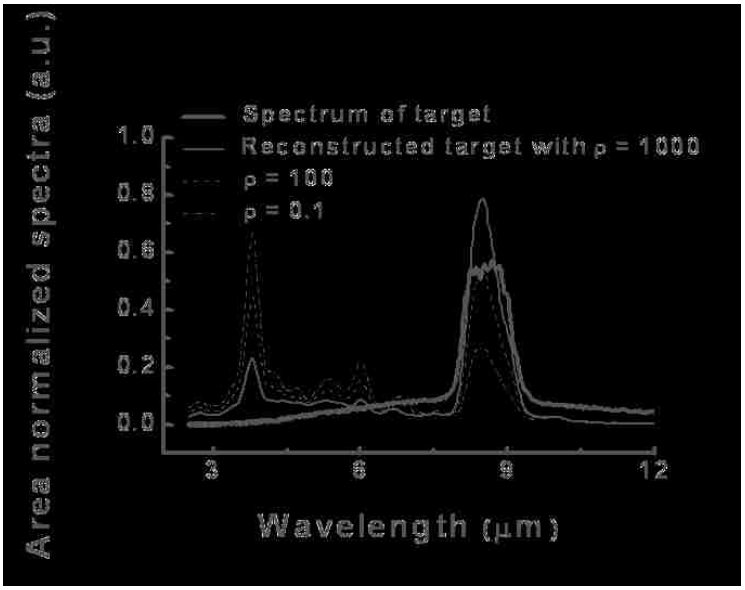

Figure 2.13: Examples of experimental reconstructions of LWIR $f_3(\lambda)$ using algorithmic spectrometer incorporated with the DWELL-1780 detector at 30 K for synthesized, high (ρ = 1000), moderate (ρ = 100), and low (ρ = 0.1) SNRs of the photocurrent as compared to SNR of the actual photocurrent [28].

Next, we investigate the dependence of the performance of the algorithmic spectrometer on the DWELL's operating temperature. Here, the procedure used to generate Fig. 2.12 (c) for the LWIR target $f_3(\lambda)$ was repeated for various operating temperatures of the DWELL detector and the results are depicted in Fig. 2.14 (dark solid curves) along with the actual spectra of the target filter (thin solid curves). As expected, the performance of the algorithmic spectrometer is degraded as the detector's temperature increases. This is a result of the increase in the dark current with temperature, which reduces the SNR, as well as the reduction in the overlap in the DWELL's spectral responses as the temperature increases (as it was pointed out in Section 2.1). While accurate reconstruction is observed at 30 K [see Fig. 2.12 (c)], as the DWELL temperature increases the reconstructed target spectra deteriorates in the passband region. For example, the performance is poor at 77 K. Thus, the algorithmic spectrometer at higher device temperatures cannot properly reconstruct the target peak even at 8-9 μm because at low SNRs the peak of the DWELL detector is buried in the DWELL's noise floor [22].

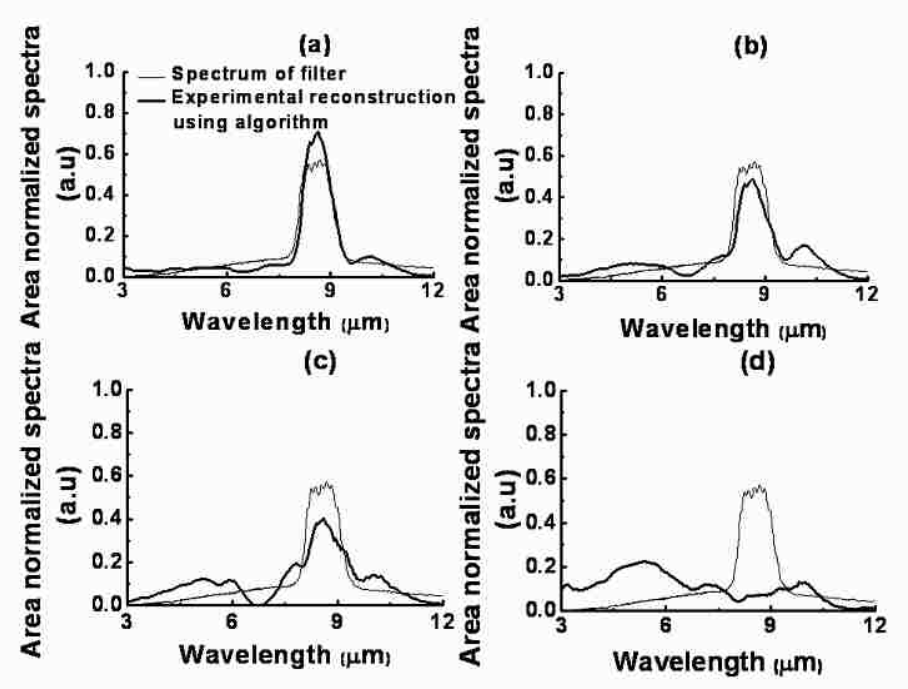

Figure 2.14: Experimental reconstructions of the spectrum $f_3(\lambda)$ using algorithmic spectrometer incorporated with the DWELL-1781 detector for various detector temperatures: (a) 30 K, (b) 50 K, (c) 60 K and (d) 77 K [28].

Finally, we examine the dependence of the performance on the diversity of the available operating biases of the DWELL-1781 detector. The bias selection is pursued to find the number of biases required to achieve acceptable target reconstruction. As a benchmark, all 82 bias-dependent spectra (i.e., 41 each at negative and positive biases from -5 to -1 V in 0.1 V step, and from 1 to 5 V in 0.1 V step) of the DWELL-1781 detector were considered to generate the LWIR target $f_3(\lambda)$. Then the reconstruction procedure was repeated for the subsampled bias voltages as follows: 40, 20, and 10. Figure 2.15 describes the reconstruction results for different bias selections. It was observed that a good target estimation was achieved even with many fewer bias voltages (for the case of ten bias voltages), showing the clear cutoff and strong response at the passband region. For consistency, the performances of DAS on the diversity of operating bias voltage were further tested with the other three LWIR filter targets $f_1(\lambda)$, $f_2(\lambda)$, and $f_4(\lambda)$ in Fig. 2.12. After applying DAS with subsampled bias voltages, target-spectrum reconstruction was achieved for these LWIR targets with an accuracy similar to that for $f_3(\lambda)$. Thus, the spectral information of original target is well maintained and preserved even with a reduced number of bias voltages. This is due to the existence of strong DWELL spectral responses at the particular bias

selections. However, the selection of weak DWELL spectral responses at biases from -1.5 to 1.5 V leads to the poor reconstructions (results not shown).

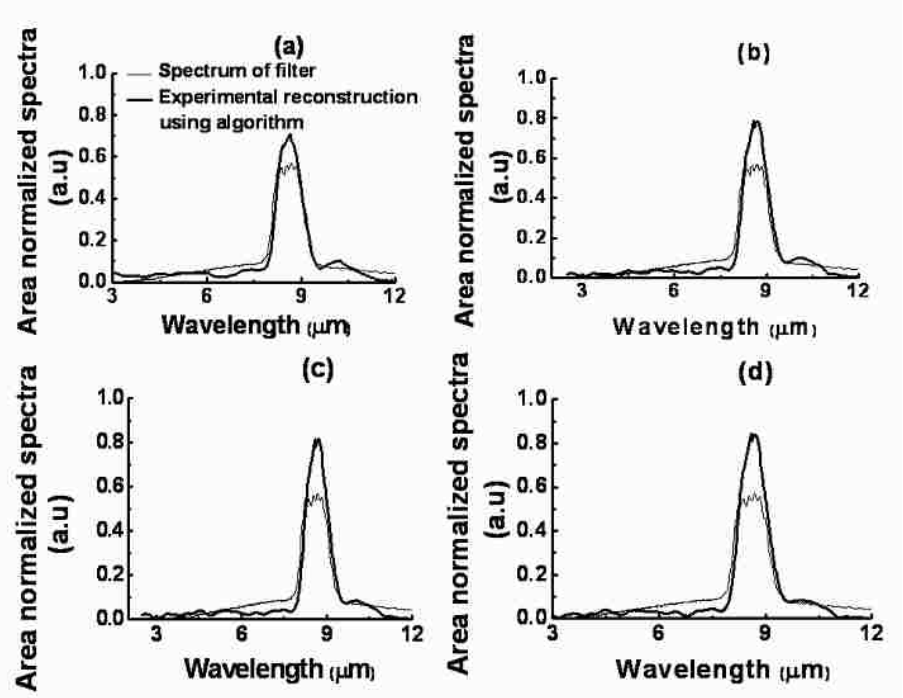

Figure 2.15: Experimental reconstructions of the spectrum $f_3(\lambda)$ using algorithmic spectrometer incorporated with the DWELL-1781 detector at 30 K for various bias selections: (a) with all 82 bias voltages (from -5 to -1 V in steps of 0.1 V, and from 1 to 5 V in steps of 0.1 V); and with a uniform subselection of (b) 40 bias voltages, (c) 20 bias voltages, and (d) 10 bias voltages [28].

2.4 Conclusions

We demonstrated an algorithmic spectrometer comprising a DWELL detector with bias-dependent spectral response, which is due to the QCSE, and a postprocessing tuning algorithm. The implementation of the algorithmic spectrometer consists of two key stages and it requires that a target is probed repeatedly by the DWELL detector at different operating bias conditions, yielding a collection of bias-dependent photocurrents. In the first stage, sets of weights are calculated using the projection algorithm reported in [22]; in particular, one set of weights is calculated for each wavelength of interest. In the second stage and for each wavelength of interest, the photocurrents are linearly combined using the very weights associated with the specific wavelength, yielding a reconstruction of the target spectrum at that wavelength. Successful algorithmic reconstructions were obtained of the spectra of four LWIR target filters validating our approach for an algorithmic spectrometer. The performance was further examined in terms of the dependences on the photocurrent's SNR, the DWELL's operating temperature, and the diversity of the available operating biases. As expected and depending upon the DWELL's operating temperature, the performance of the algorithmic spectrometer is degraded by the increase in the dark current as the detector's temperature increases above 50 K (which, in turn, reduces the SNR), and the lack of the overlap in the DWELL's spectral responses at high temperatures. The best reconstruction result was observed at 30 K. Notably, good reconstruction can be achieved even by using only ten appropriately placed biases for which strong, overlapping DWELL spectral responses exist.

Chapter 3

Multispectral Classification with Bias-tunable DWELL Focal Plane Array

In this chapter, we describe the operation principle and characterization of the DWELL FPA. Then a multispectral classification capability of the DWELL FPA is demonstrated to identify the "class" of the object of interest. The approach is validated for the filter classification problem.

3.1 Operation principle and characterization of the DWELL FPA

This section details the FPA development based on the optimized DWELL single pixel architecture. Then it is followed by the performance evaluations and comparisons of original DWELL and optimized DWELL FPAs that include spatial uniformity, responsivity and NEDT. The bias-dependent spectral tunability of DWELL FPA is also demonstrated. In addition, the DWELL FPAs are compared to the commercially available QWIP FPA.

3.1.1 FPA development and operation principle

Recently, the DWELL design was modified by maximizing the volume of the active region to improve the QE of DWELL detectors. This is accomplished by reducing the strain generated during the growth of a single DWELL stack. In an initial attempt, GaAs well was used along with an InAs QD to form the DWELL structure with $Al_{.10}Ga_{.90}As$ as the barrier. However, this structure produced poor photoluminescence (PL) intensity and the QD density was low in this structure. An $In_{.15}Ga_{.85}As$ layer was then re-introduced between the GaAs well and the InAs QDs. This modification had

shown the improvement in the QD density. Furthermore, the amount of material in the QD and doping in the dots were optimized. Also, the effect of capping the dots with a lower interfacial strain $In_{.15}Ga_{.85}As$ layer was studied for optimizing the QD optical quality. It was certainly observed that the capping of the dots with InGaAs improves the responsivity of the DWELL detector. Based upon these modifications, the optimized DWELL design (so-called the double DWELL) was achieved. This structure consists of *n*-doped InAs QDs in $In_{.15}Ga_{.85}As$/GaAs wells and $Al_{.10}Ga_{0.9}As$. With the strain reduction, the number of stacks in the active region was increased to 30. The structural progression from standard DWELL to double DWELL is well summarized in Fig. 3.1.

Figure 3.1: Progression of heterostructure from standard DWELL to double DWELL [33,34].

The spectral characteristics of double DWELL structure were also experimentally demonstrated by measuring its bias-tunable spectral responses over various device operating temperatures shown in Fig. 3.2. For this device structure, the spectral responses were obtained for a bias range from -3 to 3 V. No spectral responses were measured beyond this bias range due to the noise dominance. The spectra showed the spectral shift from 8.5 to 9.5 μm as the bias is increased form negative to positive. Some signs of shifts in MWIR were also observed in a 4~7 μm range. More importantly, improvement in device operating temperature was clearly evident since the spectral responses were obtained until at a device temperature of 120 K. This further validates that the optimizations on device growth and processing improve the responsivity and the QE without altering the bias-dependent spectral characteristics.

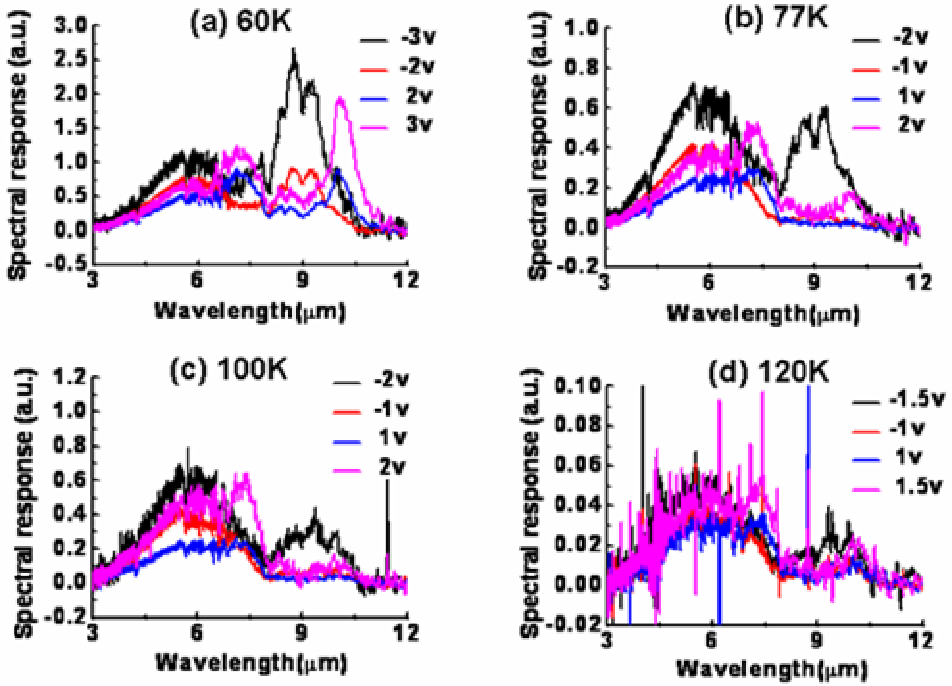

Figure 3.2: Bias-dependent spectral responses of optimized DWELL structure for different device operating temperatures at (a) 60 K, (b) 77 K, (c) 100 K and (d) 120 K [33].

The DWELL FPA samples based upon the already proven single pixel design structures were grown in a V-80 Molecular Beam Epitaxy (MBE) system, with an As_2 cracker source. After the growth, the FPA sample was then processed into a 320×256 array format with a single pixel area of 24×24 μm^2 and 30 μm pitch. The processed FPA sample was then hybridized to an Indigo 9705 Si readout integrated circuit (ROIC) with a standard bump-to-bump bonding using a FC 150 flip-chip bonder. Each pixel in FPA is essentially identical to the single pixel structure except that the substrate and bottom GaAs layer are removed and the pixel is flipped by 180°. Figure 3.3 shows the scanning electron microscope (SEM) images of fabrication procedure and the packaged FPA.

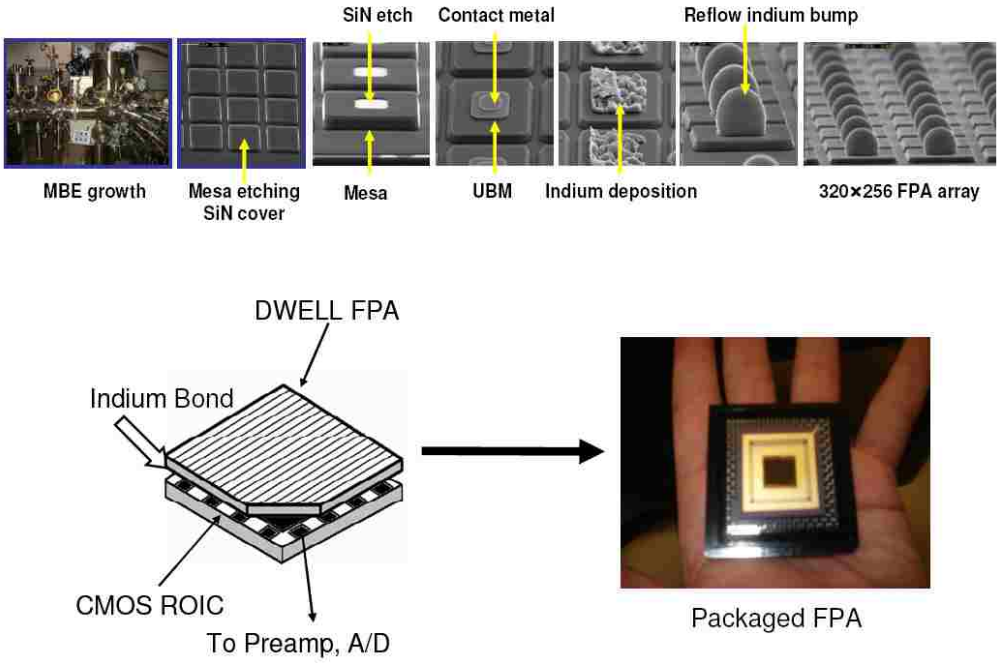

Figure 3.3: SEM images of fabrication procedure and the packaged DWELL FPA.

The DWELL FPA hybridized with ROIC was mounted in a closed-cycle dewar and cooled down. The FPA was characterized by using a commercial CamIRa^{TM} FPA demonstration system manufactured by SE-IR Corporation with an *f*/2.3 broadband (3~12 μm bandwidth) optics. This system provides the clock, the frame and line synchronizations and the bias voltages to the ROIC. The entire measurement setup is illustrated in Fig. 3.4. The ROIC then reads the pixel values of entire array and sends them serially to the computer for data processing and storage.

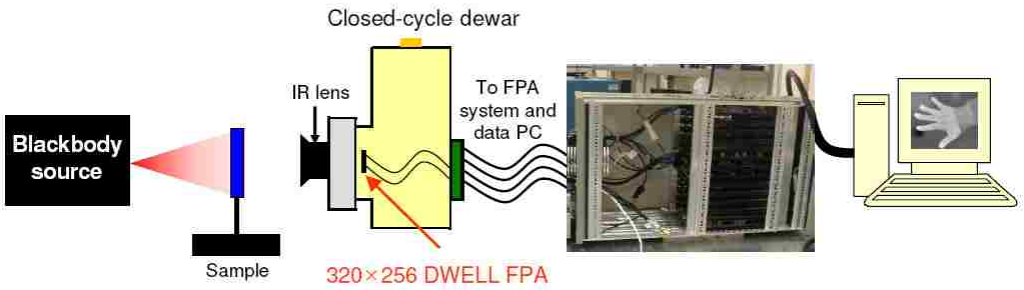

Figure 3.4: A diagram of FPA measurement setup for data acquisition.

3.1.2 Responsivity and array uniformity

The uncorrected outputs of standard DWELL and double DWELL FPAs against various blackbody temperatures were measured. The outputs were obtained as Analog-to-Digital Units (ADUs) and the maximum ADU counts for this camera system provided is 16383, corresponding to 14 bit Analog-to-Digital Converters (ADCs). During the measurements, the FPA temperature was 60 K and the applied bias was 0.82 V. Irradiance provided by a calibrated blackbody source was increased until the integration capacitors in the ROIC began to fill indicating pixels were saturated. The integration time during measurements was 11.52 ms. These values were selected in conjunction with the detector bias to maximize SNR across the observable blackbody temperature range. The results for the responsivity and the array uniformity are shown in Fig. 3.5 and compared with that of the commercial QWIP FPA.

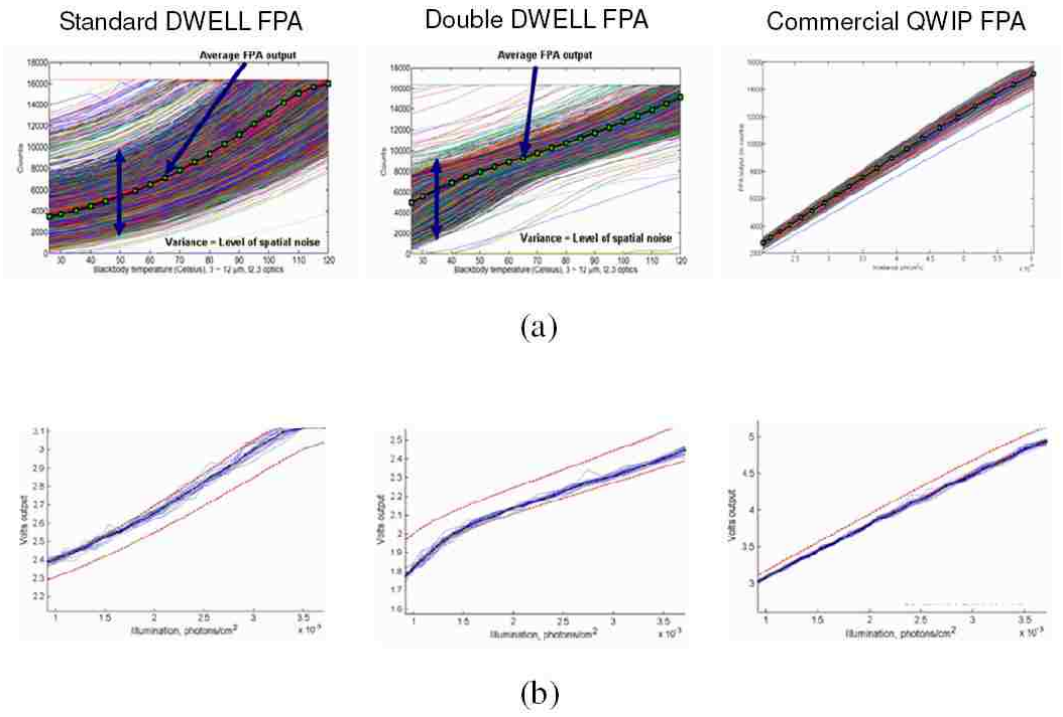

Figure 3.5: (a) FPA outputs (Counts) vs blackbody temperature for standard DWELL FPA (left), double DWELL FPA (middle) and QWIP FPA (right) over the entire array at 60 K device temperature. (b) FPA outputs (Volts) vs illumination over the 20 healthy pixels [34].

Figure 3.5 (a) displays the spatial variations of entire array and demonstrates the pixel behaviors as a function of a calibrated blackbody temperature. While the standard DWELL FPA and the QWIP FPA had a linear response, the double DWELL FPA had

shown a piecewise linear response. Based on observation by considering the variance over all pixels at each blackbody temperature, the double DWELL FPA had lower spatial deviation than the standard DWELL FPA. However, the QWIP FPA had shown the lowest spatial deviation.

The responsivity R for each FPA is proportional to the slope of FPA output (Volts) as a function of blackbody illumination in Fig. 3.5, as demonstrated by

$$R \propto \frac{dV_o}{dE_e(\lambda, T)} \quad [\text{V/W}]. \tag{4}$$

Based on (4), the responsivity was estimated and tabulated in Table 3.1.

Device	Responsivity $\propto$ (V/W)
QWIP FPA	719.46
Standard DWELL FPA	291.45
Double DWELL FPA	182.5-313.7

Table 3.1: Results for estimated responsivity for standard DWELL FPA, double DWELL FPA and QWIP FPA [34].

In Table 3.1, the QWIP FPA showed the highest responsivity and the double DWELL FPA has a range of values. This is because the double DWELL FPA showed a high responsivity at low illuminations and a low responsivity at high illuminations in a piecewise linear pixel behavior, as demonstrated in Fig. 3.5. At low illuminations, the double DWELL FPA showed a higher responsivity than the standard DWELL FPA, whereas the standard DWELL FPA had a higher responsivity than the double DWELL FPA at high illuminations.

The surface plots shown in Fig. 3.6 give further details of the uncorrected array uniformity. Aside from the large and small pixel counts (i.e. shown as sharp spikes) attributable to hot and cold pixels, respectively, remaining pixels were considered as healthy (operating) population. By visual inspection, more healthy pixels were observed on the double DWELL FPA than the standard DWELL FPA, whereas the QWIP FPA showed the largest number of healthy pixels. A linear gradient in at least one direction was clearly observed on the standard DWELL FPA as compared to the double DWELL FPA. In general, the linear gradient is caused by manufacture, possibly due to inherent non-uniformity in layer thicknesses and compositions in the MBE

growth.

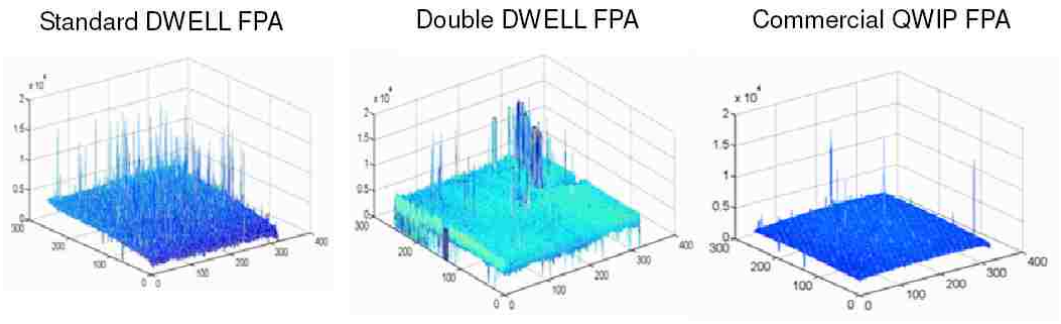

Figure 3.6: Three-dimensional surface plots of uncorrected outputs for standard DWELL FPA (left), double DWELL FPA (middle) and QWIP FPA (right) over the entire array at 60 K device temperature. Each plot was obtained when observing a blackbody source at 30°C.

3.1.3 Noise equivalent difference in temperature (NEDT)

NEDT is typically a measure of the sensitivity of a detector of thermal radiation in IR region. In other words, NEDT is a performance measure that indicates the smallest difference in uniform scene temperature that a detector can detect, so a small value is desired.

Procedure of computing NEDT is as follows, first, for each pixel of the entire 320 x 256 FPA, the device responses (output voltages) at low, T_1 and high, T_2 scene temperatures are obtained over 51 frames. Scene temperature is controlled by a calibrated blackbody source. Next, average responses R_{low} and R_{high} are calculated over 51 frames and the temporal noise voltage (N) of each pixel at T_1 is quantified by the standard deviation. Then the response to noise ratio is found by $R_s / N = (R_{high} - R_{low}) / N$. With this ratio, the NEDT between T_1 and T_2 is determined by the following expression given as,

$$\text{NEDT} = \frac{\Delta T}{R_s / N} \quad [\text{mK}], \qquad (5)$$

where ΔT is the change of blackbody temperature (i.e., $\Delta T = T_2 - T_1$).

Two kinds of NEDT were calculated: the first NEDT is the spatial average, which is the average over the 320 x 256 pixels and the second NEDT is the minimum, which represents the best value for the entire array. The results of the calculated NEDTs for the standard DWELL FPA and the double DWELL FPA were summarized in Table 3.2.

The NEDTs for the standard DWELL FPA and the double DWELL FPA were compared to that of the QWIP FPA.

Device	Parameter (mK)	60 K	80 K
QWIP FPA	Average NEDT	29.9	N/A
	Minimum NEDT	16.8	N/A
Double DWELL FPA	Average NEDT	76.9	186.1
	Minimum NEDT	44.3	N/A
Standard DWELL FPA	Average NEDT	124.5	N/A
	Minimum NEDT	71.1	N/A

Table 3.2: The minimum and average NEDTs for the standard DWELL FPA, the double DWELL FPA and the QWIP FPA.

The average NEDT for the entire FPA was measured using a blackbody source at 30°C. At 60 K FPA temperature, the average NEDT with the double DWELL FPA was lower than that with the standard DWELL FPA. The QWIP FPA showed the lowest value. In the minimum NEDT, the double DWELL FPA also demonstrated a significant improvement in NEDT over the standard DWELL FPA, although the QWIP FPA had the lowest minimum with 16.8 mK. However as a FPA temperature was raised to 80 K, both the standard DWELL FPA and the QWIP FPA were inoperable because of very high dark currents. Although the double DWELL FPA had around 186 mK, they were still operable at 80 K. The histogram plots in Fig. 3.7 give further details of NEDTs for the standard DWELL FPA and the double DWELL FPA as compared to the QWIP FPA. The low variance of histogram corresponds to the high array uniformity. The double DWELL FPA had the lower NEDT and variance over the standard DWELL FPA, while the QWIP FPA showed the lowest NEDT with the highest array uniformity. For spectral analysis, for example, material classification, the spatially uniform region associated with each object is selected. As shown in Section 3.4, each selected region was used for training the classifier and objects in the testing scenes taken at different times carrying inherent variability in the data were successfully classified. This demonstrates the robustness of sensing algorithm against the pixel variability. Details of classification results are shown in Section 3.4. To compensate for the spatially non-uniform response of the detectors within the FPA, we also perform a non-uniformity correction algorithm to radiometrically correct the pixel values at each bias voltage.

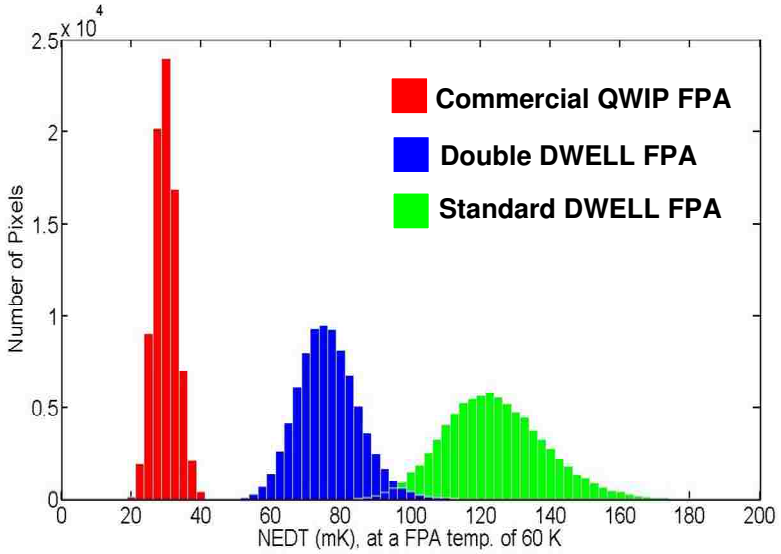

Figure 3.7: Histogram plots of NEDTs for standard DWELL FPA (green), double DWELL FPA (blue) and QWIP FPA (red) over the entire array at 60 K device temperature. Each plot was obtained when observing a blackbody source at 30°C.

3.2 Bias-tunability of the DWELL FPA

FPA imagery shown in Fig. 3.8 is used to demonstrate the bias tunability of double DWELL FPA. For imagery, the operating temperature of the DWELL FPA was set to 60 K and the integration (exposure) time was 11.5 ms. A 150°C temperature was used since such a high temperature blackbody offered a good transmittance for objects in a scene. The images are taken at 0.6, 0.8 and 1.2 V, respectively. Normalized images are shown in Fig. 3.8 (bottom row). The DWELL FPA data is normalized at each pixel by the approximate area of the multibias pixel response in order to eliminate the intensity effect in the calculations. More details about the normalization are given in Subsection 3.3.2.

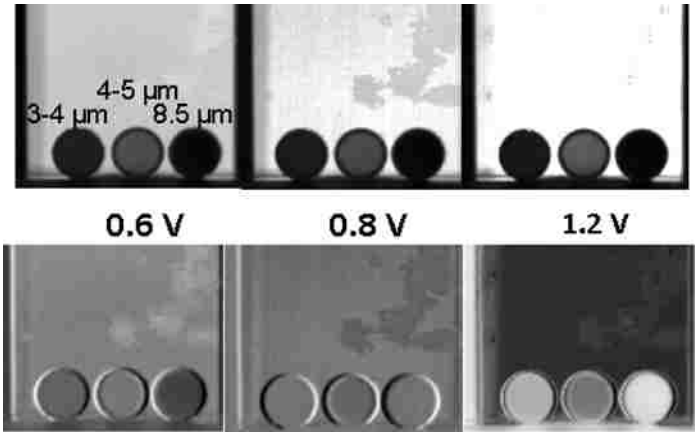

Figure 3.8: DWELL FPA images of three IR optical filters taken at 0.6 V, 0.8 V and 1.2 V bias voltages. Top figures are raw data and bottom figures are normalized data**.**

The spectral tunability of DWELL FPA had been confirmed by considering the calculated spectral ratios for pairs among IR spectral filters (at 3-4 µm, at 4-5 µm and at 8.5 µm) as shown in Fig. 3.8. Figure 3.9 shows the spectral ratios calculated for the pair of objects (filters and background) from the normalized scene in Fig. 3.8 as a function of the applied bias voltages. The spectral ratios vary between 0.4 to almost 1.4 when the applied bias voltage changes in the range from 0.3 to 1.2 V with a step of 0.1 V. Note that for bias voltages 0.7 and 0.8 V, the ratios between pair of objects are close to one, indicating low spectral separability between the objects at these particular bias voltages.

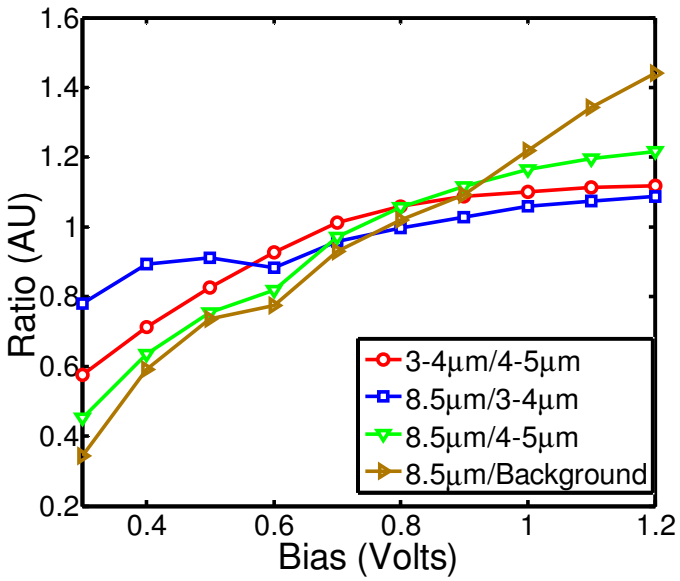

Figure 3.9: Ratio of pixel values for various pairs of the objects (filters and background) as a function of applied bias voltage.

The fact that the ratio values change from one bias to another demonstrates that the double DWELL FPA can sense different spectral contents of the materials observed in a scene simply by changing the applied bias voltage. Note that for the conventional (spectrally non-tunable) broadband FPA the spectral ratios would remain fixed as a function of the applied bias voltage. This can be demonstrated with a commercial device such as micro-bolometer, which shows a broadband and non-tunable spectral response..

3.3 Multispectral classification using bias-tunable DWELL FPA

In this section, we provide a brief overview of the mathematical model for bias-tunable multispectral sensing and discuss the classification problem.

3.3.1 Bias-tunable multispectral sensing

Mathematically, the DWELL spectral bands can be viewed as a family of functions $\{f_{v_i}(\lambda)\}$, parameterized by the applied bias voltages v_i [35]. In what follows, we denote the spectrum of an object by $p(\lambda)$. For example, $p(\lambda)$ may represent transmittance, bidirectional reflectance measurement or hemispherical reflectance data. The photocurrent for the i^{th} band of the DWELL detector sensing an object with a given spectrum $p(\lambda)$ can be written as

$$I_{v_i} = \int_{\lambda_{\min}}^{\lambda_{\max}} p(\lambda) f_{v_i}(\lambda) d\lambda + N_{v_i}. \qquad (6)$$

Here, N_{v_i} denotes additive, scene-independent noise associated with the i^{th} band, and the interval $[\lambda_{\min}, \lambda_{\max}]$ represents the common spectral support for all bands and objects. Next, for a given set of applied bias voltages $\{v_1,\ldots,v_n\}$, the output of the DWELL detector is a set of photocurrents at these bias voltages

$$\mathrm{I} = (I_{v_1}, ..., I_{v_n}). \qquad (7)$$

This set represents the multibias or multispectral signature of the object as "seen" by the DWELL detector.

Because the DWELL bands are wide and overlapping, the photocurrents in I are highly

correlated. The redundancy in the information content of the photocurrents can be reduced by a suitable postprocessing algorithm, which, in turn, can be used to improve the efficiency of the classification process. Here, we shall use the canonical correlation feature selection (CCFS) [35] algorithm to replace the *n*–dimensional multibias signature in (7) by a single feature that is optimized with respect to a given class of objects.

For a given class of objects represented by a mean spectrum $\overline{p}(\lambda)$, the output from the CCFS algorithm is a single transformed feature $\bar{I} = \sum_{i=1}^{n} a_i I_{v_i}$, which is a weighted linear combination of all features in (7). The weights a_i are optimized by the CCFS for every class of objects represented by their mean spectrum $\overline{p}(\lambda)$.

The transformed feature $\bar{I}$ can be viewed as the current generated by a "virtual" *superposition* band, $\bar{f} = \sum_{i=1}^{n} a_{v_i} f_{v_i}$; the optimal selection rule of the weights is derived rigorously in [35]. Consequently, the problem of determining the optimal current, $\bar{I}$, for a given class representative or class mean spectrum $\overline{p}(\lambda)$, is equivalent to finding a superposition band $\bar{f}$ that provides the best approximation of $\overline{p}(\lambda)$. Mathematically, $\bar{f}$ can be interpreted as an approximation of $\overline{p}(\lambda)$ in the space spanned by $\{f_{v_i}\}$, which minimizes the distance and at the same time maximizes the SNR [35].

3.3.2 Object classification problem

The classification problem considered is that of separating multiple combinations of MW and LW IR spectral filters with different bandwidths and center wavelengths. For this problem, we used the three scenes shown in Fig. 3.10 (a)–(c). The classes identified for the classification problem are summarized in Table 3.3.

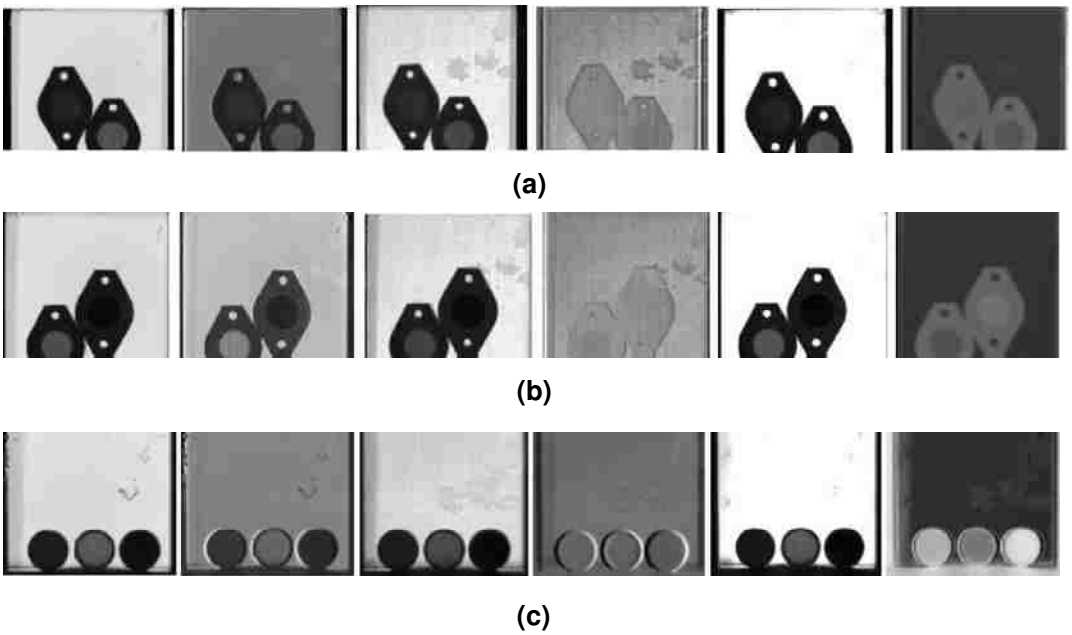

Figure 3.10: Columns one, three, and five, a-c show DWELL FPA raw imagery acquired at 0.3, 0.7, and 1.2 V, respectively. Columns two, four, and six, a-c, show the normalized imagery at 0.3, 0.7, and 1.2 V, respectively. Objects in scene; scene in row (a): filter MW_1 (left) and MW_2 (right); scene in row (b); filters MW_2 (left) and LW_3 (right); scene in row (c): filters MW_1 (left), MW_2 (center) and LW_3 (right) [36].

Classification Problem	Identified Classes
Scene (a)	MW_1, MW_2 filters, metal holder and background
Scene (b)	MW_2, LW_3 filters, metal holder and background
Scene (c)	MW_1, MW_2, LW_3 filters and background

Table 3.3: Summary of identified classes for the filter classification problem [36]

Two types of normalization techniques are applied to the raw digital numbers (DNs) that are retrieved directly from the DWELL FPA. First, at each bias voltage, pixel's DN values are radiometrically corrected by a two-point nonuniformity correction (NUC) [37] algorithm. The NUC compensates for the spatially nonuniform response of the detectors within the FPA and is an integrated part of the image acquisition process. The two-point NUC is performed using temperatures at 22℃ and 150℃. The lower temperature of 22℃ corresponds to the lens-cap's room temperature, which was used to yield the lower-temperature uniform field.

Next, for every radiometrically corrected pixel and its replicas at each bias voltage, the pixel's value is normalized as follows:

$$\underline{I}(v_j) = \frac{I(v_j)}{\Delta v \sum_{i=1}^{n} I(v_i)} \tag{8}$$

where Δv is the voltage step size used to increment the DWELL FPA's bias. Equation (8) is equivalent to normalization by the area enclosed under the multibias response of each pixel in the DWELL FPA. The normalized multibias response of a pixel can then be written as

$$\underline{\mathrm{I}} = (\underline{I}(v_1),...,\underline{I}(v_n)). \tag{9}$$

This normalization minimizes the role of broadband emissivity in the discrimination process and emphasizes the spectral contrast. The normalized images at 0.3, 0.7, and 1.2 V for the classification problem are shown in columns two, four, and six in Fig. 3.10(a)–(c), respectively.

We perform a supervised classification comprising of training and testing steps for the classification problem. To determine representative multibias signatures for each class listed in Table 3.3, we follow the same approach as used in [35]. Specifically, for each class we compute statistical mean and covariance matrix using spatially uniform regions that are visually associated with that class. Subsequently, Euclidean-distance classifier is trained by the classes' mean multibias signatures and the covariance matrices [38].

At the testing step, the trained classifiers are used to classify the objects in Table 3.3 from a set of testing scenes. These scenes capture the same images as the training scenes but were acquired at different times. As a result, the testing scenes carry inherent variability in the data due to the difference in the measurement conditions from day-to-day and the presence of ambient and system noise. The testing images are normalized in the same fashion as the training images. The size of training and testing data set for the filter classification problem are listed in Table 3.4.

Classification Problem	Number of Pixels in Training/Testing Sets
Scene (a)	MW_1: 140/235, MW_2: 140/235, metal holder: 66/161 and background: 300/300
Scene (b)	MW_2: 154/330, LW_3: 108/320, metal holder: 126/260 and background: 352/340
Scene (c)	MW_1: 400/280, MW_2: 400/280, LW_3: 400/280 and background: 336/350

Table 3.4: Number of pixels used in the training and testing data sets for the filter classification problem [36]

3.4 Theoretical and experimental classification results

The thematic maps for the filter classification problem using Euclidean-distance classifier are presented in Fig. 3.11 (a)–(c), respectively. These maps show the distribution of the derived classes over the spatial area captured by the DWELL FPA. Each map defines a partitioning of the area into sets, each including the points with identical class labels. In order to investigate the effect of the bias selection on the classification accuracy, the classification is performed for multiple combinations of biases.

The results for the filter classification problem, specified in Table 3.3, are shown in Fig. 3.11 (a)–(c), and Table 3.5 shows the calculated classification errors for various classes. The thematic maps in Fig. 3.11 (a)–(c) are obtained using four different sets of bias voltages: (i) one bias at 0.3 V; (ii) one bias at 0.7 V; (iii) two bias voltages at 0.6 and 0.7 V; and (iv) all bias voltages in the range of 0.3–1.2 V.

For the first bias voltage set, the Euclidean-distance classifier consistently shows good classification for all three scenes as shown by the thematic maps in the first column in Fig. 3.11 (a)-(c). This observation is confirmed by the classification errors in Table 3.5 for this case. In contrast, for the second bias voltage set the Euclidean-distance classifier cannot discriminate successfully between the filters, metal holders and background, as shown by the thematic maps in the second column in Fig. 3.11 (a)–(c). This result and the classification errors in Table 3.5 show that the bias voltage at 0.7 V is not a good choice for these scenes. However, adding a second bias voltage at 0.6 V to the second set (resulting in our third bias voltage set) improves the classification as shown by the thematic maps in third column in Fig. 3.11 (a)–(c). Finally, the thematic

maps in the last column in Fig. 3.11 (a)–(c) and the classification errors in Table 3.5 indicate almost perfect classification results for the fourth set of bias voltages, i.e., when all ten biases are used. In Fig. 3.11, it is also to be noted that the classifier has generated successful results regardless of the location of object (pixel variability) in a scene.

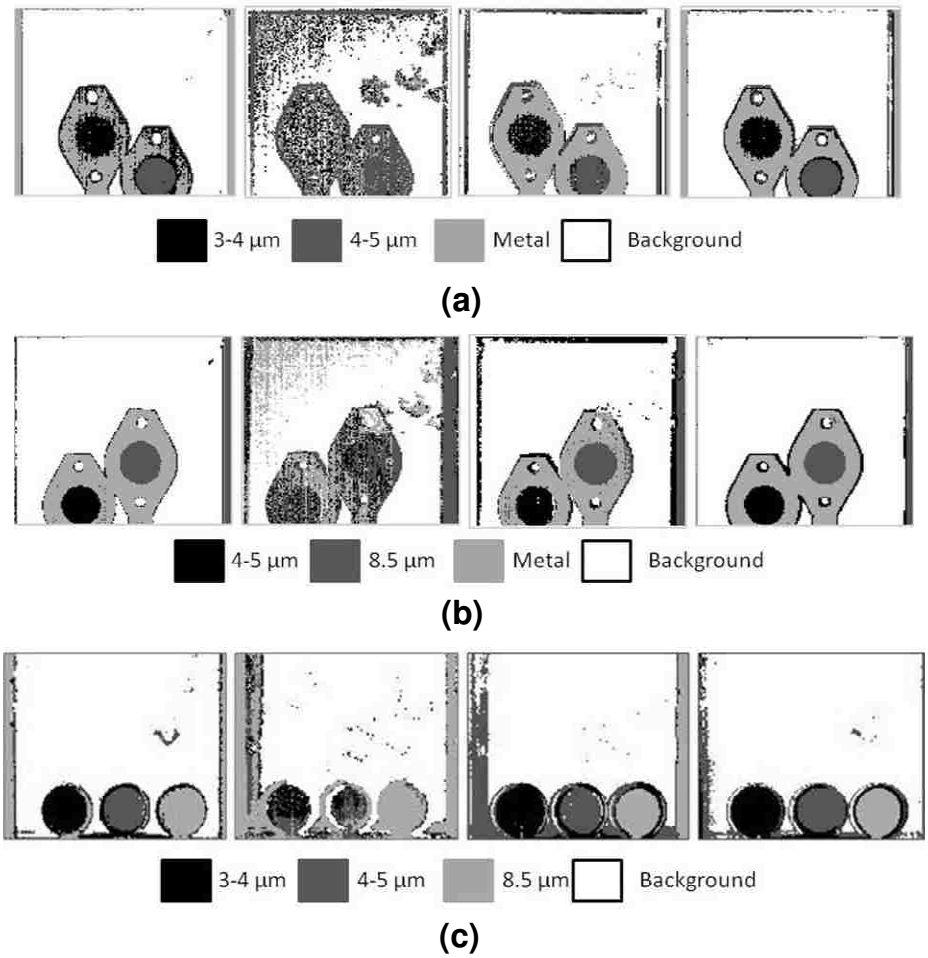

Figure 3.11: Thematic maps, from left to right: bias at 0.3 V used, bias at 0.7 V used, combination of biases at 0.6 and 0.7 V used, and all biases in the range of 0.3–1.2 V used; (a) MW_1 and MW_2; (b) MW_2 and LW_3; (c) MW_1 , MW_2 and LW_3 [36].

Classification Problem	Bias (V)	MW_1 Error (%)	MW_2 Error (%)	Metal Error (%)
Scene (a)	0.3	2	0.4	32
	0.7	63	4	70
	0.6, 0.7	15	0.8	0
	0.3-1.2	0.8	0	0
Scene (b)	**Bias (V)**	**MW_1 Error (%)**	**MW_2 Error (%)**	**Metal Error (%)**
	0.3	0	0	5
	0.7	64	44	23
	0.6, 0.7	0.5	0	7
	0.3-1.2	0	0	5
Scene (c)	**Bias (V)**	**MW_1 Error (%)**	**MW_2 Error (%)**	**Metal Error (%)**
	0.3	0	2.5	4
	0.7	42.75	58.5	4.5
	0.6, 0.7	1	2.7	1
	0.3-1.2	1.7	1.7	0

Table 3.5: Classification errors in the filter classification problem using Euclidean-distance classifier [36]

3.5 Conclusions

The DWELL FPA based on the optimized structure was developed and its performance was compared with the first-generation DWELL FPA and the commercially available QWIP FPA. Radiometric characterizations had demonstrated that this new DWELL FPA has higher device operating temperature than the first-generation FPA and the QWIP FPA. In addition, this new DWELL FPA had demonstrated the bias-dependent spectral tunability with the calculated spectral ratios for pairs among IR spectral filters.

Using this optimized DWELL FPA, we have demonstrated for the first time the MS classification capability of the DWELL FPA by exploiting the DWELL's bias tunability along with a traditional algorithm (i.e., Euclidean distance classifier). The DWELL FPA performance has been validated using a classification demonstration: separation between three mid-IR spectral filters. Our verification studies show that, as a result of its bias tunability, the DWELL FPA can successfully capture spectral contrast between different materials, which, in turn, enables their accurate classification. The results from the classification analysis demonstrate that accurate classification can be achieved by either considering a broader range of spectral information, i.e., by using all bias voltages, or by using specific biases, or combination thereof. Finally, a

customized feature-selection algorithm that specifically addresses the abundant spectral overlap and noise in the DWELL bands, such as the CCFS, can additionally enhance the MS capability of the DWELL FPA by selecting only few optimized superposition bands that yield the same classification results as when using all DWELL FPA bands.

Chapter 4

Data Compressive Paradigm for Multispectral Sensing using Tunable DWELL Mid-infrared Detectors

The algorithmic spectrometer described in Chapter 2 was designed without restricting the number of bias-dependent photocurrents to be used in forming the superposition photocurrent. For practical implementation, it may be necessary to limit the number of applied biases used (or equivalently, the number of data acquisitions) due to hardware (memory and processors), cost and/or total acquisition-time constraints. The delay associated with acquiring a high number of photocurrents sequentially is proportional to the number of biases, making the method inadequate for dynamic targets. It is therefore critical that we extend and optimize the sensing algorithms so that only a minimum number of biases are used. The ability to utilize a small number of biases can be exploited by a smart-pixel read-out circuitry in order to enable on-chip implementation of the algorithm.

In this chapter, we describe a generalized data-compressive MS sensing algorithm to substantially compress the number of necessary biases, and hence the amount of data to be sensed, subject to a prescribed performance level. A minimal set of biases identified by the algorithm enable the sensor to sense only the relevant spectral information for remote-sensing applications of interest.

4.1 Review of algorithmic spectral sensing and moving on to reducing the sensed data

In this section, we review germane aspects of our original algorithmic multispectral sensing approach [22]. The DWELL's spectral bands are denoted by the functions $R_1(\lambda),\ldots,R_K(\lambda)$, corresponding to the applied bias voltages $v_1,\ldots,v_K$. Let us consider an arbitrary target of interest with unknown spectrum, $p(\lambda)$, that is probed by the DWELL photodetector at the bias values $v_1,\ldots,v_K$. The output of the DWELL photodetector is represented by a vector of bias-dependent photocurrents, $\mathbf{I} = [i_1,\ldots,i_K]^T$; the m^{th} photocurrent, i_m, corresponds to the m^{th} bias v_m. Mathematically, i_m is expressed by

$$i_m = \int_{\lambda_{\min}}^{\lambda_{\max}} p(\lambda) R_m(\lambda) d\lambda + N_m, \tag{10}$$

where N_m denotes bias-dependent noise associated with the m^{th} band, and the interval $[\lambda_{\min}, \lambda_{\max}]$ represents the available wavelength range for all bands and objects. The photocurrent vector represents the bias-driven multispectral data vector of the object as seen by the DWELL detector operated at the prescribed bias set. Note that since the spectral bands of the DWELL detector are relatively broad and highly overlapping the bias-dependent photocurrents inherently have a high level of redundancy. As referred to Subsection 2.2.1, the spectral tuning algorithm calculates the weight vector $\mathbf{w}_n$ using (1) and the transmittance of unknown target is reconstructed by a weighted linear combination with the photocurrent vector $\mathbf{I}$, denoted by $\mathbf{w}_n{}^T\mathbf{I}$ (synthesized photocurrent)**.** This process is repeated for the entire tuning wavelengths of interest. We emphasize that the weights are calculated offline and their calculation does not involve any knowledge of the target's spectrum.

4.1.1 Challenges in reducing the number of required biases

To reiterate, the reduction in the number of required biases is needed for two reasons: (1) to minimize the substantial redundancy in the bias-dependent photocurrents as a target is probed by the DWELL detector at the different biases and (2) to make the approach amenable to near real-time implementation by reducing the data-acquisition time. There are two challenges in reducing the number of require biases that this paper aims to surmount. Firstly, if we restrict the number of biases to a small value, there needs to be a viable algorithm for selecting the actual biases from an often-large

number of available biases. The challenge here is that the complexity of a direct search approach is exponential due to the combinative nature of the problem. Secondly, even if the first challenge is overcome and we are able to generate a small set of biases for each one of the narrowband (hypothetical) tuning filters $r(\lambda;\lambda_n)$, we may obtain a different set of reduced biases for each filter. Thus, an aggregated set of biases (obtained by taking the union of the small number of biases for each filter) that guarantees good performance for all the filters may no longer be small.

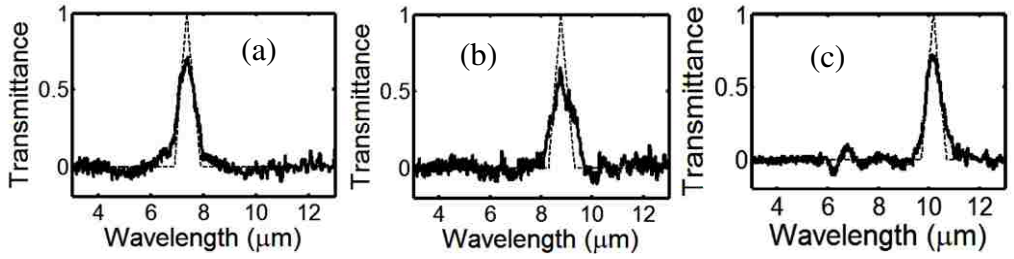

Figure 4.1: Example of three different narrowband tuning filter approximations centered at (a) 7.4 μm, (b) 8.8 μm and (c) 10.2 μm, the algorithm requires 21 out of 30 biases. The biases used are {-3.0, -2.8, -2.6, -2.2, -2.0, -1.8, -1.6, -1.4, -1.2, -0.8, -0.6, -0.4, -0.2, 0.2, 0.4, 0.6, 0.8, 1.4, 1.8, 2.4, 2.6} [31].

To help appreciating the second challenge, consider the example were we are interested in approximating three spectral filters (n = 3) as shown in Fig. 4.1. Suppose that we have a total of 30 DWELL spectral responses corresponding to the biases in the range -3 to 3 V in steps of 0.2 V. With an approximation-error metric for performance defined and specified (to be described in details in Section 4.2), we would need only eight biases for each tuning filter from 30 biases. Our calculations based on the results to be presented in Section 4.2 (the MBS approach) show that the reduced bias sets for the tuning filters (a), (b) and (c) are {-2.2, -1.2, -0.8, -0.2, 0.2, 0.4, 0.6, 0.8 V}, {-3.0, -2.8, -2.6, -1.8, -1.4, -0.6, -0.4, 1.4 V} and {-2.0, -1.6, -0.8, 0.2, 1.4, 1.8, 2.4, 2.6 V}, respectively. Thus, to approximate all three tuning filters with the same prescribed approximation error, then we would need 21 biases in total.

In the following section we will provide a solution that addresses both of the aforementioned challenges.

4.2 Uniformly-accurate compressive spectral-sensing algorithm

We begin by defining an extension of the spectral-tuning algorithm described in Subsection 2.2.1 in a generalized setting for which the set of biases and the hypothetical spectral filters (to be approximated by the DWELL spectral responses) are arbitrarily specified. Consider the collection, $\mathrm{F}_{\mathrm{DWELL}}= \{R_1,\ldots,R_K\}$, of the DWELL spectral responses corresponding to a maximal set of biases $B_{\mathrm{DWELL}} =\{v_1,\ldots,v_K\}$; namely, $R_i(\lambda)$ is the spectral response of the DWELL detector when voltage v_i is applied to it. Let $F_{\mathrm{MS}} = \{f_1,\ldots,f_M\}$ be a collection of hypothetical multispectral sensing filters designed for specific sensing problems of interest and let $b\subset\{1,\ldots,K\}$ be the index set for a specified subset of biases from B_{DWELL}. For each filter f_i, let $\hat{f}_i^{(b)} = \sum_{j\in b} w_{i,j}^{(b)} R_j(\lambda)$ be its approximation using the set of biases identified by b. In this approximation, the weight vector $\mathbf{w}_i^{(b)} = [w_{i,1}{}^{(b)}, \ldots, w_{i,|b|}{}^{(b)}]$ is calculated according to (11) with the proviso that the matrices $\mathbf{A}$ and $\mathbf{\Phi}$ are now restricted to the set of biases specified by b, which we denote as $\mathbf{A}^{(b)}$ and $\mathbf{\Phi}^{(b)}$. More precisely,

$$\mathbf{w}_i^{(b)}=[(\mathbf{A}^{(b)})^T\mathbf{A}^{(b)}+ \mathbf{\Phi}^{(b)}+ \alpha(\mathbf{A}^{(b)})^T\mathbf{Q}^T\mathbf{Q}\mathbf{A}^{(b)}]^{-1}[(\mathbf{A}^{(b)})^T f_i(\lambda)], \quad i=1,\ldots,M. \tag{11}$$

(In the absence of noise ($\mathbf{\Phi}^{(b)}\equiv 0$), the solution in (11) is simply the projection of the function f_i onto the linear space generated by the functions R_i, $i\in b$.) As a performance metric for approximating *all* the hypothetical spectral filters in F_{MS} using the index set b for the specified bias collection, we define the average approximation error

$$e_b = 100\times M^{-1}\sum_{i=1}^{M}\frac{\int_{\lambda_{\min}}^{\lambda_{\max}}\left(f_i(\lambda)-\hat{f}_i^{(b)}(\lambda)\right)^2 d\lambda}{\int_{\lambda_{\min}}^{\lambda_{\max}} f_i^{\,2}(\lambda)d\lambda}. \tag{12}$$

We finally introduce a relative error metric, $P^{(b)}$, that puts e_b in the context of the minimum error possible, $e_{\{1,\ldots,K\}}$, when using all K biases are used. Namely,

$$P^{(b)} = 100 \times |e_b - e_{\{1,\ldots,K\}}|. \tag{13}$$

The $e_{\{1,\ldots,K\}}$ is the reference (minimal) error used later for benchmarking the performance in reduced bias sets. For a given performance level θ, our goal is to find a minimal subset of biases, $B_{\min} \subset B_{\text{DWELL}}$ with $b_{\min} \subset \{1,\ldots,K\}$, for which we are guaranteed that $P^{(b_{\min})} \leq \theta$. Next, we introduce two algorithms for determining $B_{\min}$.

4.2.1 Bias-selection algorithms

Two bias-selection algorithms are reported here: the Minimal-Bias-Set (MBS) algorithm, which gives optimal results using an exhaustive search approach, and the Approximate Minimal-Bias-Set (AMBS) algorithm, which offers a suboptimal solution, based on a greedy search approach, but offers huge computational advantage over the MBS algorithm. (A minimal collection of biases may not be unique.)

The procedure of MBS algorithm is straightforward. It searches among all the minimal number of required biases q^* and a corresponding q^*-bias collection $B_{\min}$ is identified by the index set $b_{\min}$ for which the resulting error metric $P^{(b_{\min})}$ is below the prescribed error threshold $\theta \geq P^{(\{1,\ldots,K\})}$. More precisely, the exhaustive-search method for identifying the minimal bias subset $B_{\min}$ is described through the following steps.

Minimal-Bias-Set Algorithm:

1) Initialization step: set $q = 1$.

2) Calculate $\mathbf{W}_{\text{MS}}^{(b_q)} = \{\mathbf{w}_1^{(b_q)}, \ldots, \mathbf{w}_M^{(b_q)}\}$ and $P^{(b_q)}$ for all $b_q \subset \{1, \ldots, K\}$ such that $|b_q|=q$.

3) Identify the bias subset B_q^* with the index set b_q^* for which $P^{(b_q^*)}$ is at a minimum; namely, $b_q^* = \underset{b_q \subset \{1,\ldots,K\}, |b_q|=q}{\operatorname{argmin}} P^{(b_q)}$.

4) If $P^{(b_q^*)} \leq \theta$, then the minimal number of required biases, q^*, is calculated set to q and b_q^* is set to $b_{\min}$. As a result, $B_{\min} = B_q^*$. If $P^{(b_q^*)} > \theta$ and $q < K$, then increment q by 1 and go to Step 2.

Note that since $\theta \geq P^{(\{1,\ldots,K\})}$ the algorithm described in Steps 1-4 must terminate in at most K steps. Also note that in general $P^{(b_q^*)} \geq P^{(b_{q+1}^*)}$, q=1,…, K-1.

This MBS algorithm is optimal but it is computationally feasible only when q is reasonably small (e.g., q = 4 and K = 30 as in the example considered in Section 4.3.) since the identification of each b_q^* involves $\binom{K}{q}$ calculations of $P^{(b_q)}$. For large q values the number of bias combinations to consider becomes enormous, which results in unrealistically large computing times. As an alternative, we can employ a greedy approach we referred to as AMBS, which is suboptimal, where the biases for the q+1 are selected by augmenting the q biases from an earlier stage of the selection process by a single bias that is selected optimally from the remaining K-q biases. The number of searches for each q is therefore reduced from $\binom{K}{q}$ to K-q. To avoid falling in local minima early on in the selection process, we start the process by first performing the exhaustive-search bias selection process for a small q value (typically q=3 in our examples) and then employ the greedy approach. The AMBS algorithm in determining a suboptimal minimal bias subset, $\tilde{B}_{\min}$, is described through the following steps.

Approximate Minimal-Bias-Set Algorithm:

1) Initialization step: select a (small) initial value, q_0, and use the exhaustive search method to identify the bias subset $B_{q_0}^*$ with the index set $b_{q_0}^*$ for which $P^{(b_{q_0}^*)}$ is at a minimum. Set $q = q_0$. If $P^{(b_q^*)} \le \theta$, b_q^* is $\tilde{b}_{\min}$. Then $\tilde{B}_{\min} = B_q^*$ and the search process is complete. If $P^{(b_q^*)} > \theta$ then go to Step 2.

2) Calculate $j_q = \arg\min_{j \in K \setminus b_q^*} P^{(b_q^* \cup \{j\})}$ and define the augmented bias subset $\tilde{B}_{q+1}^* = B_q^* \bigcup \{B_{j_q}\}$. Here, $K \setminus b_q^*$ is the set of all integers that are in K but not in b_q^*. If $P^{(\tilde{b}_{q+1}^*)} \le \theta$ then set $q^* = q$+1 and $\tilde{b}_{\min} = \tilde{b}_{q^*}^*$. As a result, $\tilde{B}_{\min} = \tilde{B}_{q^*}^*$, which completes the search process.

3) If $P^{(\tilde{b}_{q+1}^*)} > \theta$ and $q < K$, increment q by 1 and go to Step 2.

Note that since $\theta \ge P^{(\{1,\ldots,K\})}$, the algorithm described in Steps 1-3 must terminate in at most K steps.

The AMBS approach falls in the more general category of *matching pursuit algorithms* reported by [39,40]. Both approaches are based upon a greedy principle and share the common objective of searching for a sparse solution to represent the signal based upon a suboptimal forward search. In both approaches, a search is made through a "dictionary" in an iterative fashion rather than solving the optimal approximation problem. However, there are two key differences in the implementation of the search processes used in the AMBS and that used by the matching pursuit algorithms. The AMBS algorithm selects the vector (or subset) from a given dictionary based upon minimizing the "first-order residual," which simply corresponds to the error between the true signal and the projected signal. On the other hand, the matching pursuit algorithm chooses the vector from the set of dictionary vectors iteratively by sub-decomposing the residual to represent the original signal, thereby considering "higher-order residuals," as explained in [39,40]. Another key difference is that the AMBS involves an important initialization step, based on exhaustive search, for finding a good initial value in order to avoid falling in local minima early on in the selection process. The greedy process then follows the initial step.

4.2.2 Uniformly-accurate compressive spectral sensing algorithm

The uniformly-accurate compressive spectral sensing (UCSS) algorithm is summarized in Fig. 4.2. There are three inputs specified by the user. The first input is the collection, $\mathtt{F}_{\mathrm{DWELL}}$ and the corresponding maximal set of biases B_{DWELL}. The second input is the collection F_{MS} of hypothetical multispectral sensing filters for the specific sensing problems of interest. The third and final input is the user-prescribed worst-case error threshold, θ, for the error metric $P^{(b)}$.

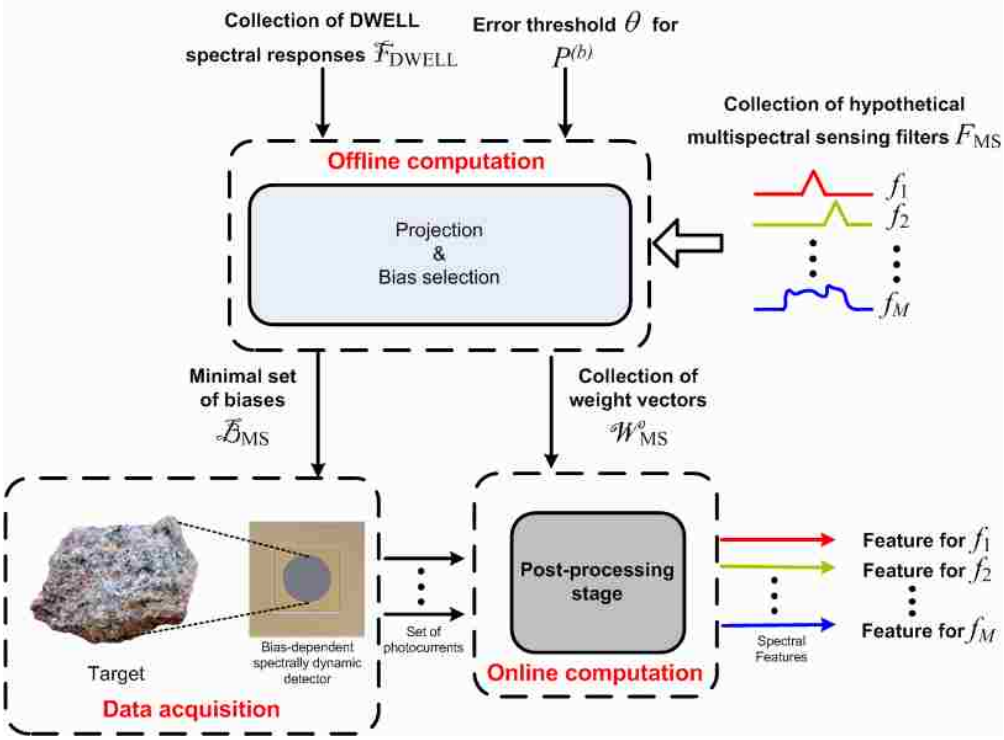

Figure 4.2: Illustration of the remote-sensing applications of data compressive UCSS algorithm [31]

Here the threshold θ is selected such that it is achievable, namely, $\theta \geq P^{([1,\ldots,K])}$. The set of indices, $b_{\min} \subset \{1,\ldots,K\}$, is obtained from either MBS or AMBS algorithms described in Subsection 4.2.1, and it defines a minimal set of biases $\mathcal{B}_{\text{MS}}$. The optimal collection of weight vectors corresponding to with $b_{\min}$ and F_{MS} is $\mathbf{W}_{\text{MS}} = \{\mathbf{w}_1^{(b_{\min})}, \ldots, \mathbf{w}_M^{(b_{\min})}\}$ (here M is the number of spectral filters in F_{MS}). Note that each weight vector is of length $|B_{\min}|$. In the final stage of the UCSS algorithm, the photocurrents from the spectrally tunable detector sensing a target at the minimal bias-set $\mathcal{B}_{\text{MS}}$; these photocurrents are the most relevant spectral dataset for any specific application represented by F_{MS}. The photocurrents are then linearly combined according to the subset of weight vectors from $\mathbf{W}_{\text{MS}}$, corresponding to the spectral filters in F_{MS}, to yield the desired features equivalent to those that we would have obtained had we used a broadband detector in conjunction with the spectral filters in F_{MS}.

4.2.3 Generalization to linear space generated by the collection of hypothetical multispectral sensing filters

Suppose that we are interested in sensing using a hypothetical filter, $\tilde{f}$, a linear superposition of individual filters in the collection F_{MS}: $\tilde{f}(\lambda) = \sum_{i=1}^{M} \beta_i f_i(\lambda)$ where β_i's are scaling factors that are chosen to control the shape of $\tilde{f}(\lambda)$). For example, if M = 2, β_1 = -1 and β_2 = 1, then $\tilde{f}(\lambda) = f_2(\lambda) - f_1(\lambda)$, which yields the differences of the spectral features at λ_2 and λ_1. Is it possible to extend the ST algorithm to accommodate this scenario without the need for redoing the bias-selection optimization problem (Subsection 4.2.1) for the extended filter set $F_{MS} \cup \{\tilde{f}\}$? Indeed, the linear nature of the sensing problem at hand dictates that the required weight vector $\tilde{\mathbf{w}}^{(b_{\min})}$ associated with $\tilde{f}$ is nothing but a linear superposition of the scaling factors of the individual filter elements in F_{MS}:

$$\tilde{\mathbf{w}}^{(b_{\min})} = \sum_{i=1}^{M} \beta_i \mathbf{w}_i^{(b_{\min})} \tag{14}$$

This can be seen by simply applying the formula in (11) to the function $\tilde{f}(\lambda) = \sum_{i=1}^{M} \beta_i f_i(\lambda)$ and a simplifying the result to obtain

$$\tilde{\mathbf{w}}^{(b_{\min})} = \sum_{i=1}^{M} \beta_i [(\mathrm{A}^{(b_{\min})})^{\mathrm{T}} \mathrm{A}^{(b_{\min})} + \Phi^{(b_{\min})} + \alpha (\mathrm{A}^{(b_{\min})})^{\mathrm{T}} \mathrm{Q}^{\mathrm{T}} \mathrm{Q} \mathrm{A}^{(b_{\min})}]^{-1} [(\mathrm{A}^{(b_{\min})})^{\mathrm{T}} f_i(\lambda)],$$

which is simply $\sum_{i=1}^{M} \beta_i \mathbf{w}_i^{(b_{\min})}$. With $\tilde{\mathbf{w}}^{(b_{\min})}$ available, the hypothetical filter $\tilde{f}$ is approximated by

.

$$\hat{\tilde{f}}(\lambda) = \sum_{j=1}^{|b_{\min}|} \left(\mathbf{w}_i^{(b_{\min})} \right)_j R_j(\lambda). \tag{15}$$

4.3 Case study on optimal bias selection

4.3.1 Specification of sensing filters and their approximations by a minimal bias set

We experimentally measured the bias-dependent spectral responses of the DWELL photodetector, $\mathbb{F}_{\mathrm{DWELL}}=\{R_1(\lambda),R_2(\lambda),\ldots,R_{30}(\lambda)\}$, with 30 different biases corresponding to the bias set $B_{\mathrm{DWELL}}=\{-3, -2.8, -2.6, \ldots, 3\ \mathrm{V}\}$. We also set the error threshold, θ, to 8 %, and further specified F_{MS} as the collection of six spectral sensing filters $\{f_1(\lambda), f_2(\lambda),\ldots,f_6(\lambda)\}$. Specifically, $f_1(\lambda)$, $f_2(\lambda)$ and $f_3(\lambda)$ are defined as three disjoint hypothetical narrowband triangular sensing filters centered at 7.4 μm, 8.8 μm and 10.2 μm, each with a full-width at half maximum of 0.5 μm. We select the filters $f_4(\lambda)$, $f_5(\lambda)$ and $f_6(\lambda)$ to be the actual transmittances of three optical filters in the ranges 7.5-10.5 μm, 8.0-9.0 μm and 8.5-11.5 μm. For the generalization in Subsection 4.2.3, we specified two linearly superpositioned filters: a spectral integrator $\tilde{f}_1(\lambda)$ and a spectral differentiator $\tilde{f}_2(\lambda)$. The filter $\tilde{f}_1(\lambda)$ is the sum of $f_1(\lambda)$, $f_2(\lambda)$ and $f_3(\lambda)$, and the filter $\tilde{f}_2(\lambda)$ is the difference between $f_2(\lambda)$ and $f_1(\lambda)$, as shown in the dotted lines in Fig. 4.3 (c). The UCSS algorithm was invoked and a minimal set of four biases was obtained by using the MBS algorithm: $B_{\mathrm{MS}}=\{-3, -0.8, 1.0, 2.8\ \mathrm{V}\}$ (with the corresponding set of indices, $b_{\min}$). The corresponding collection of six weight vectors $\mathbf{W}_{\mathrm{MS}}=\{\mathbf{w}_1^{(b_{\min})},\ldots,\mathbf{w}_6^{(b_{\min})}\}$ was also found, resulting in a relative error metric $P^{(b_{\min})}$ = 6.7%, which satisfies the prescribed error threshold of $\theta=8\%$. Approximations of the member of F_{MS} are shown in solid blue lines of Fig. 4.3 (a) for $f_1(\lambda)$, $f_2(\lambda)$ and $f_3(\lambda)$, and in solid blue lines in Fig.4.3 (b) for $f_4(\lambda)$, $f_5(\lambda)$ and $f_6(\lambda)$. Since an error metric is only 6.7%, shapes of approximated F_{MS} using minimal four biases are very similar to the reference (the approximated F_{MS} using entire 30 biases) shown in solid red lines of Fig. 4.3. This demonstrates that the use of minimal biases selected by the MBS algorithm does not sacrifice performance. Also note that as compared to the result in Fig. 4.1 by the original ST algorithm (which uses 21 biases), the use of the MBS algorithm has significantly reduced the number of required biases down to four, resulting in a reduction by a factor of 7.5 in the required biases for

sensing. The weight vector $\tilde{\mathbf{w}}_1^{(b_{\min})}$ associated with the spectral integrator $\tilde{f}_1(\lambda)$ is obtained by solving (14) with W_{MS} and the scale factors $\beta_1 = \ldots = \beta_3 = 1$ and $\beta_4 = \ldots = \beta_6 = 0$. Similarly, for the spectral differentiator $\tilde{f}_2(\lambda)$, the weight vector $\tilde{\mathbf{w}}_2^{(b_{\min})}$ is found by solving (14) with W_{MS} and the scale factors $\beta_1 = -1, \beta_2 = 1$ and $\beta_3 = \ldots = \beta_6 = 0$. Approximations of $\tilde{f}_1(\lambda)$ and $\tilde{f}_2(\lambda)$ are shown in Fig. 4.3 (c).

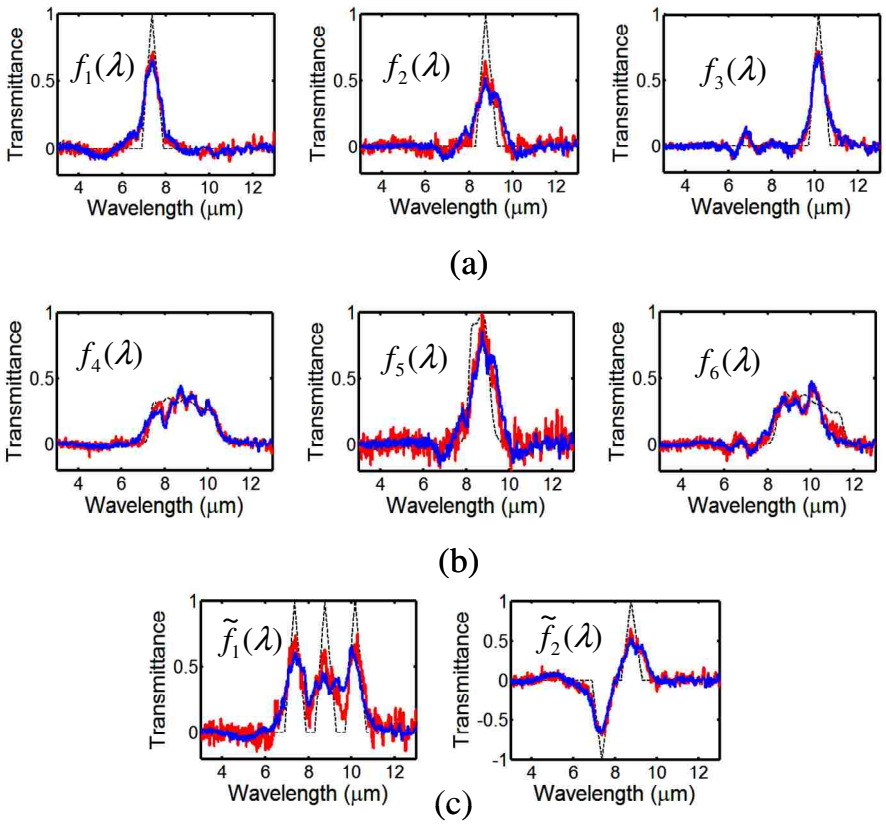

Figure 4.3: The MBS algorithm is used to approximate the specified spectral-filter collection F_{MS}: (a) $f_1(\lambda)$, $f_2(\lambda)$ and $f_3(\lambda)$ are hypothetical narrowband triangular sensing filters and (b) $f_4(\lambda)$, $f_5(\lambda)$ and $f_6(\lambda)$ are spectral matched filters using only minimal four biases B_{MS} out of K = 30 biases, B_{DWELL}. The successful approximations using minimal four biases are shown in blue, which corresponds to the error metric $P^{(b_{\min})}$ = 6.7% as compared to the approximations using all 30 biases shown in red. The approximations (in blue) of two superposition filters, the spectral integrator $\tilde{f}_1(\lambda)$ and the spectral differentiator $\tilde{f}_2(\lambda)$, are shown in (c) along with the approximations using all 30 biases in red [31].

Performance of the AMBS algorithm for F_{MS}:

In this subsection, we evaluate the performance of the AMBS algorithm for approximating the specified collection F_{MS}. The results from the AMBS are also compared to those of the MBS. For evaluation purposes, we applied the AMBS algorithm to three different cases by specifying three different error thresholds: (i) $\theta = 8\%$, (ii) $\theta = 6\%$ and (iii) $\theta = 5\%$. Results for all three cases are given in Tables 4.1, 4.2 and 4.3, respectively. We observed that the minimal bias set identified by the AMBS algorithm does not exactly match that obtained by the MBS algorithm in all three cases. However, the error metrics $P^{(B_{\min,AMBS})}$ (7.1%, 5.4% and 4.6%) for the AMBS are all within 0.5% of $P^{(B_{\min,MBS})}$ (6.7%, 5.1% and 4.4%) for the MBS, demonstrating almost identical performance. Also note that for all three cases, the search time by the AMBS algorithm is faster than the MBS algorithm. Particularly, in case (iii), the search time by the AMBS algorithm is 69 times faster than the MBS algorithm. Thus, the AMBS algorithm can be a good alternative to the MBS algorithm since it can generate comparable results with less computational effort.

MBS	Minimal bias set (V)	$B_{MS,\ MBS}$ = {-3, -0.8, 1, 2.8}
	Minimal error metric (%)	$P^{(B_{\min,MBS})} = 6.7$
	Bias search time (sec)	233.4
AMBS	Minimal bias set (V)	$B_{MS,\ AMBS}$ = {-3, -1.4 , 1.4 , 2.8}
	Minimal error metric (%)	$P^{(B_{\min,AMBS})} = 7.1$
	Bias search time (sec)	62.1
	Improvement factor in time	233.4/62.1 = 3.8

Table 4.1: Summary of results for case (i) comparing between MBS and AMBS algorithms for the approximations of F_{MS} [31].

MBS	Minimal bias set (V)	$B_{MS,\ MBS}$ = {-3, -1.4, -0.8, 1, 2.8}
	Minimal error metric (%)	$P^{(B_{\min,MBS})} = 5.1$
	Bias search time (sec)	1323.5
AMBS	Minimal bias set (V)	$B_{MS,\ AMBS}$ = {-3, -1.4 , -0.4 , 1.4 , 2.8}
	Minimal error metric (%)	$P^{(B_{\min,AMBS})} = 5.4$
	Bias search time (sec)	56.7
	Improvement factor in time	1323.5/56.7 = 23.4

Table 4.2: Summary of results for case (ii) [31]

MBS	Minimal bias set (V)	$B_{MS,\ MBS}$ ={ -3, -1.4, -0.8, 0.8, 2.2, 3}
	Minimal error metric (%)	$P^{(B_{\min,MBS})} = 4.4$
	Bias search time (sec)	4008.5
AMBS	Minimal bias set (V)	$B_{MS,\ AMBS}$ = {-3, -1.4 , -0.4 , 1 , 1.4 , 2.8}
	Minimal error metric (%)	$P^{(B_{\min,AMBS})} = 4.6$
	Bias search time (sec)	57.9
	Improvement factor in time	4008.5/57.9 = 69.2

Table 4.3: Summary of results for case (iii) [31].

4.3.2 Flexibility in the minimal bias selection

In Subsection 4.3.1 we identified a minimal set of four biases. However, we have seen some level of tolerance to these bias values with a minimal penalty in performance. In this subsection we generate four groups of biases that offer a more flexible specification of the minimal set of required biases. In particular, an alternative minimal set of biases can be obtained by selecting a bias from each group of biases.

To introduce flexibility in the bias selection, we allowed the MBS algorithm to find the top-twenty ranked bias sets instead of single minimal bias set B_{MS}. The tolerance in the error metric is set to 0.2% as compared to the original error metric of $P^{(b_{\min})} = 6.7\%$. With this procedure, we generated 10 biases in total (there are at most 80 biases that can be generated but many of these where duplicates). We can then list all these 10 biases and identify four groups. The significance of each bias out of the 10 biases is determined by the number of times it is selected by the top-twenty bias sets. The significance of the 10 biases is illustrated by the histogram shown in Fig. 4.4. By visual inspection, four different bias groups G_1, G_2, G_3, and G_4, are identified and listed in Table 4.4. Note that the originally selected optimal biases are members of these groups, as identified by thick text in Table 4.4.

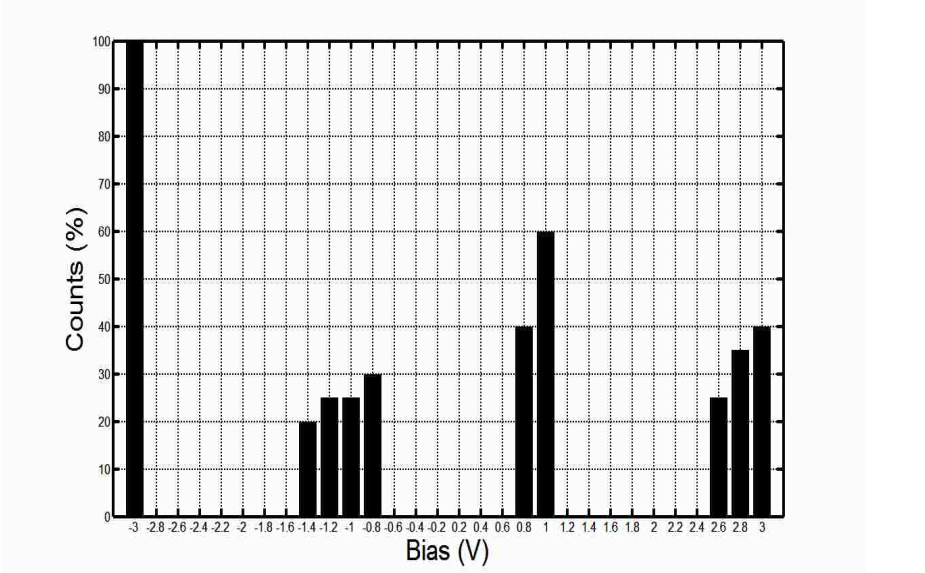

Figure 4.4: The histogram illustrates the significance of each bias member in the set of 10 biases. By visual inspection, we identified four distinct bias groups [31].

Bias group	Identified member
G_1	{**-3** V}
G_2	{-1.4, -1.2, -1, **-0.8** V}
G_3	{0.8, **1.0** V}
G_4	{2.6, **2.8**, 3 V}

Table 4.4: Identified members in four bias groups for approximating the specified filter collection F_{MS}. Values in thick text are those selected by the MBS bias-selection algorithm [31].

Our ability to identify the populated bias group, for example G_4, is attributable to the similarity in the DWELL's spectral responses at these three biases and their comparable SNRs. The corresponding spectral responses are compared in Fig. 4.5, showing the similarity among them. It is interesting to note that the collections of biases, {-2.8, -2.6, -2.4, -2.2, -2, -1.8, -1.6 V}, {-0.6,-0.4, -0.2, 0.2, 0.4, 0.6 V} and {1.2, 1.4, 1.6, 1.8, 2.0, 2.2, 2.4 V} are never selected due to the fact they have little overlap with the members of F_{MS} as well as their relatively low SNRs. We have verified that the SNRs for the bias collection {-2.8, -2.6, -2.4, -2.2, -2, -1.8 V} are much lower (< 80) than those for -3 V (> 300), which explains why -3 V is always selected while its neighboring biases are not selected. Moreover, the biases -0.2, 0.2, 0.4, and 0.6 V are never selected because their SNRs (< 10) are the lowest among all the biases.

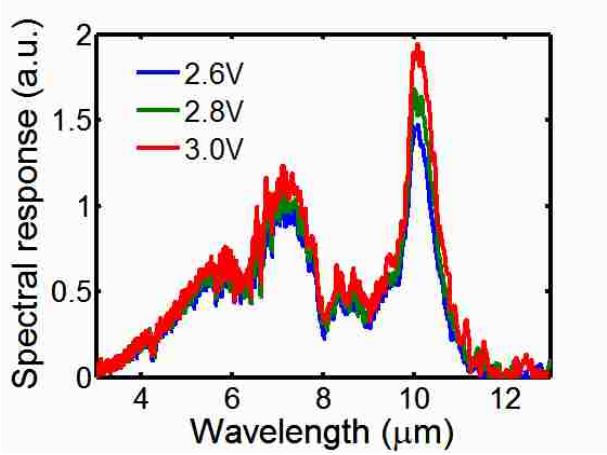

Figure 4.5: Similarity of the DWELL's spectral responses at 2.6, 2.8 and 3 V [31].

The histograms in Fig. 4.6 further show the contribution of each bias component in the group for cases (ii) and (iii) in Subsection 4.3.1 compared to case (i) as shown in Fig. 4.4. In Figs. 4.6 (b) and (c), we find five and six bias groups for cases (ii) and (iii) respectively. Also in Fig. 4.6, we observed that the group 2 in case (i) is divided into two groups (i.e., groups 2 and 3) in case (ii). Likewise, the group 5 in case (ii) is split

into groups 5 and 6 in case (iii). These are certainly expected results since the MBS bias-selection algorithm offers more bias groups as we move from case (i) to (iii). It means that the user can select biases in a broader range as more groups become available.

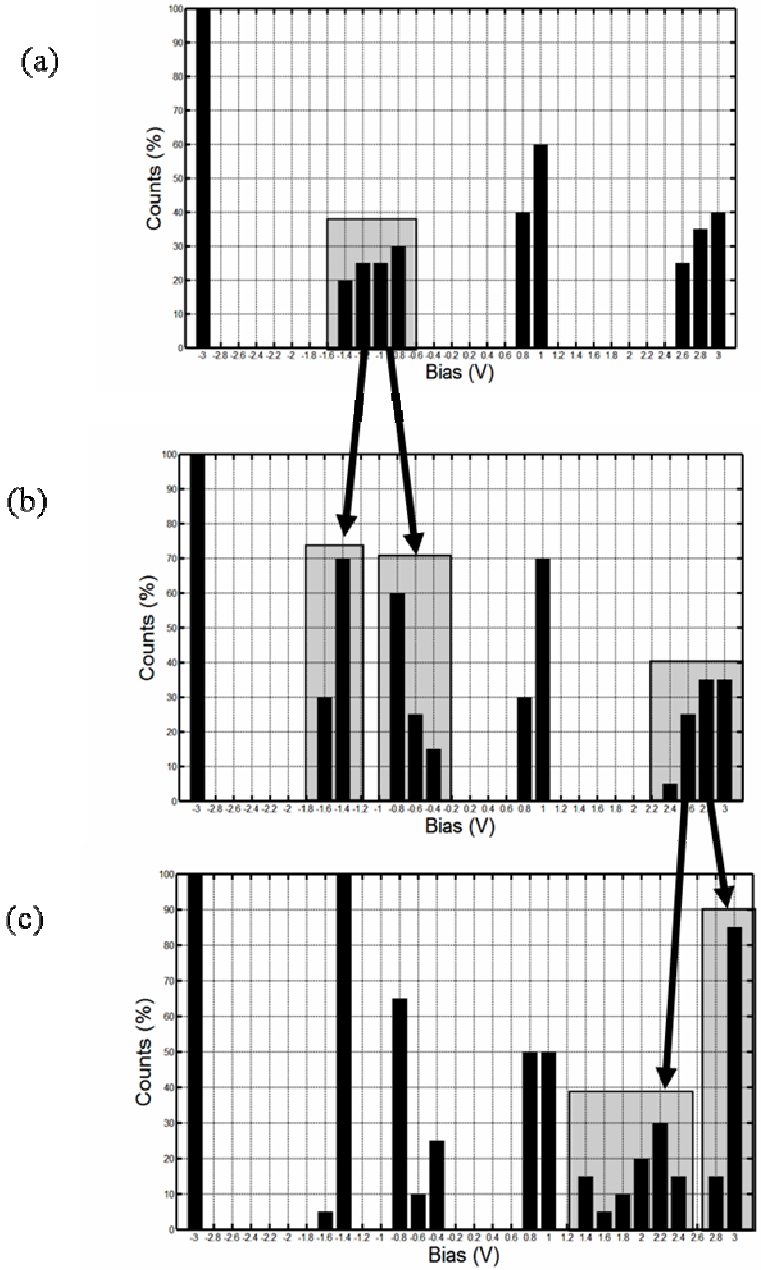

Figure 4.6. Histograms demonstrating the contribution of each bias member in a group for case (i), (ii) and (iii) shown in (a), (b) and (c) respectively. Shaded areas point out the trends that group 2 in case (i) is split to two groups (groups 2 and 3) in case (ii) and group 5 in case (ii) is split into two groups (groups 5 and 6) in case (iii).

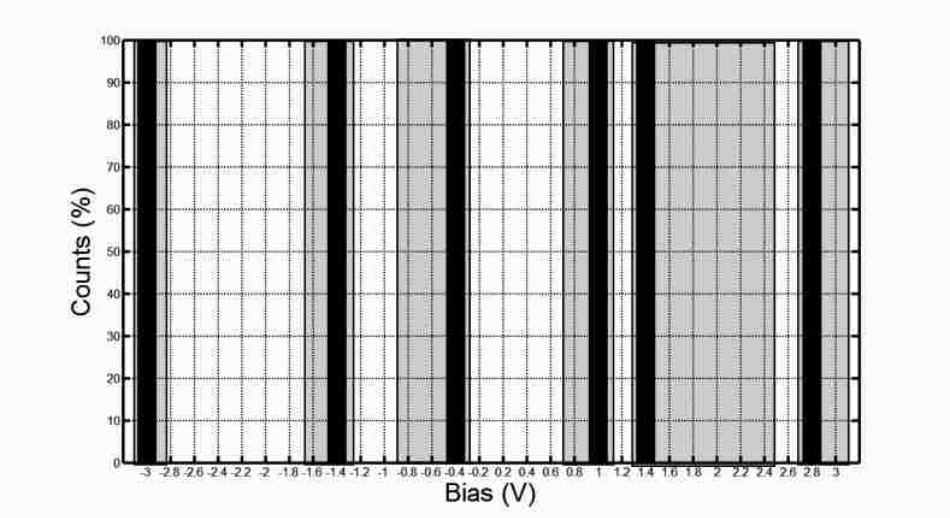

Figure 4.7. Histogram showing six selected biases (solid bar) by the AMBS algorithm. Shaded regions correspond to six bias groups selected by the MBS algorithm. Since these all six biases are within groups, two bias-selection algorithms are consistent in performance.

4.4 Experimental results on spectrometry and classification

In order to experimentally demonstrate the multispectral sensing capability of the UCSS algorithm, we have applied the collection, F_{MS}, of filters described in Subsection 4.3.1 to two common remote-sensing applications. The first application is spectrometry, termed algorithmic spectrometry here. It aims to reconstruct samples of the spectra of any *unknown* target of interest at prescribed tuning wavelengths without the use of any physical dispersive elements or optics. This is done by means of forming a weighted linear superposition of the bias-dependent photocurrents, measured by the DWELL detector, according to a predetermined set of weights obtained from the UCSS algorithm. The measured photocurrents are obtained by probing the unknown target by the DWELL detector using a minimal bias set provided by the MBS algorithm. The result of this weighted-superposition process is a set of "superposition photocurrents" that represent samples of the transmittance at desired tuning wavelengths. In addition to sampling the spectrum of the unknown target, we can also extract more general spectral features, such as an spectral average over multiple wavelengths or slope of the spectrum at specified wavelengths, by performing weighted superposition using other predetermined weights (also from the UCSS algorithm) applied to the same bias-dependent photocurrent.

The second application is the classification of a probed unknown object as that having one of multiple known transmittance spectra (the spectra are selected from the members of F_{MS}), based on the concept of algorithmic spectral matched filtering. The idea of spectral matched filtering is to use multiple weight vectors (as many as the number of candidate transmittance spectra) obtained from the UCSS algorithm that can be used by a "classifier" to perform a weighted linear superposition of the measured bias-dependent photocurrents. The measured photocurrents in this case results from probing the unknown target whose transmittance spectrum is any one of multiple possible spectra. The result is a set of extracted "superposition features," which the classifier further converts to the "label" of the unknown object (label of its spectrum). Details of the experimental procedure and results for these two remote-sensing applications are given next.

4.4.1 Experimental results on target spectrometry

Three spectral filters, $f_1(\lambda)$, $f_2(\lambda)$ and $f_3(\lambda)$ (members of F_{MS}), are selected to sample the transmittance of the unknown target centered at λ_1=7.4 μm, λ_2=8.8 μm and λ_3=10.2 μm. The unknown target was selected as the spectral filter in the range 7.5-9.5 μm, whose transmittance spectrum is shown in Fig. 4.8, solid red line.

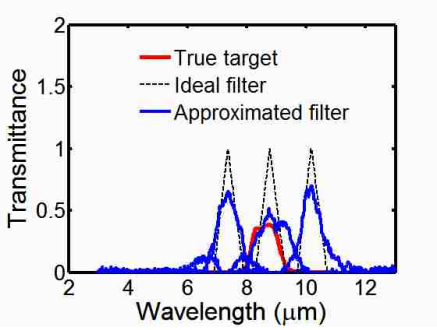

Figure 4.8: Three spectral filters, $f_1(\lambda)$, $f_2(\lambda)$ and $f_3(\lambda)$ in the filter collection F_{MS} are used to sample the unknown target, whose transmittance is shown in red. For reference, the ideal triangular spectral filters are also shown in dashed line. Approximated filters in blue line were obtained by the UCSS algorithm using minimum four biases -3.0, -0.8, 1.0, 2.8 V selected by the MBS algorithm [31].

We measured the photocurrent vector, $\mathbf{I}_{spec}$, as the DWELL photodetector sequentially probed the unknown filter target using the minimal set of four biases {-3.0, -0.8, 1.0, 2.8 V} selected by the MBS algorithm as described in Section 4.3. For comparison, the photocurrent measurement was also repeated for the following auxiliary bias sets: the best-five bias set {-3, -1.4, -0.8, 1, 2.8 V}, the best-six bias set {-3, -1.4, -0.8, 0.8, 2.2, 3 V} and the complete bias set consisting of all 30 biases. Note that in the best-five and

best-six bias set cases the biases were selected using the MBS algorithm described in Section 4.2 by constraining the number of biases to 5 and 6, respectively. Specifically, the measured $\mathbf{I}_{\text{spec}}$ is linearly combined with each weight vector, yielding a superposition photocurrent $\hat{I}_i = (\mathbf{w}_i^{(b_{\min})})^T \mathbf{I}_{\text{spec}}$, where i = 1,2, 3. As referred to [28], this superposition photocurrent $\hat{I}_i$, termed "experimental reconstruction" best approximates the transmittance of unknown target that we would have obtained if we look at the same target through the ideal triangular spectral filter. Recall that in Subsection 4.3.1, the UCSS algorithm generated three weight vectors: $\mathbf{w}_1^{(b_{\min})}, \mathbf{w}_2^{(b_{\min})}$ and $\mathbf{w}_3^{(b_{\min})}$ corresponding to $f_i(\lambda)$, i=1, 2 and 3.

The experimental reconstructions using minimal four biases are shown in Fig. 4.9 (blue circle) and represent the sampled transmittances of target at λ_1, λ_2 and λ_3. We also generated the estimated transmittances resulting from sampling the true target transmittance by ideal triangular filters centered at λ_1, λ_2 and λ_3, shown in Fig. 4.9 (red square), and used them as a reference for accurate comparison. Results show that both the reconstruction and the reference at λ_1 and λ_3 are close to zero. These values are consistent with the true target transmittance shown in Fig. 4.8 (red) since λ_1 and λ_3 correspond to the stopband where the transmittance is zero. At λ_2= 8.8 μm, the reconstructed transmittance is within 30% error as compared to the corresponding reference (0.123 and 0.171 in Table 4.5). Also for a comparison, the true target transmittance at 8.8 μm in Fig. 4.8 (red) is 0.381, which is the ground truth. Note that the ultimate goal of our algorithmic sensing approach is to estimate this true transmittance in the best way possible; the use of the narrowest "triangular filter" is just a one way for achieving this goal.

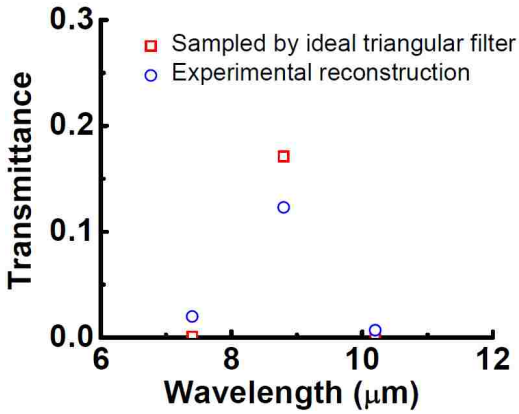

Figure 4.9: Experimentally reconstructed transmittances (blue circle) at 7.4 μm, 8.8 μm and 10.2 μm extracted by the UCSS algorithm using minimum four biases -3.0, -0.8, 1.0, 2.8 V selected by the MBS algorithm were obtained. Results are compared to the sampled transmittances by the ideal triangular spectral filters (red square) considered as the reference [31].

Results from the other bias selections (best-five and best-six bias sets) by the MBS algorithm are also shown in Table 4.5. Here, we observed that the reconstructions at 7.4 μm and 10.2 μm are close to zero for all bias selections. At 8.8 μm, the reconstructions for all bias selections are within 8%. Thus, the use of minimal four biases does not sacrifice the performance of UCSS algorithm in successfully extracting the narrowband feature.

Experimental reconstruction	Number of selected biases				Transmittance sampled by ideal triangle
	Min. 4 biases	Best-5 biases	Best-6 biases	All 30 biases	
at 7.4 μm	0.02	0.021	0.021	0.021	0.001
at 8.8 μm	0.123	0.126	0.128	0.133	0.171
at 10.2 μm	0.007	0.007	0.008	0.008	0.001

Table 4.5: Comparison of experimental reconstruction of the transmittance at three wavelengths using the minimal four biases by the MBS algorithm and the associated reconstruction errors to those using other bias selections by the MBS algorithm (best-5 biases, best-6 biases and all 30 biases) [31].

Note that in Table 4.5 we find the error between the experimental reconstruction and the ideal reconstruction (using ideal triangular filters) starts to increase at some point as more biases are used. As we explained in our prior work [22], this observation is not contradictory to the optimality of the algorithm since sets of weights determined in the spectral tuning algorithm do not guarantee minimizing the error between the actual target spectrum and the reconstruction. Instead, what these weights do guarantee is that the error between the ideal triangular tuning filter and the approximate triangular tuning filter is minimized. Indeed, the error in the synthesized triangular filters do

decrease monotonically in the number of biases used, achieving a minimum error when all 30 biases are used. Note that the quality of the reconstructed transmittance not only depends on the quality of approximation of the triangular filter but also on actual transmittance (its variation as a function wavelength within the passband of the triangular filter). We also suspect that for the case of reconstructing spectral content at $\lambda_3 = 10.2$ μm, when the algorithm uses all 30 biases, those biases beyond the fifth bias selected have weak signal content and their inclusion simply adds more noise to the estimate, hence increasing the reconstruction error.

Moving onto the superposition filter case (as described in Subsection 4.3.1), the UCSS algorithm found two weight vectors, $\tilde{\mathbf{w}}_1^{(b_{\min})}$ and $\tilde{\mathbf{w}}_2^{(b_{\min})}$, that approximated the spectral integrator $\tilde{f}_1(\lambda)$ and the spectral differentiator $\tilde{f}_2(\lambda)$, respectively. Each weight vector is linearly combined with $\mathbf{I}_{\text{spec}}$, obtaining the reconstructed spectral features $\hat{\tilde{\mathbf{I}}}_i = (\tilde{\mathbf{w}}_i^{(b_{\min})})^T \mathbf{I}_{\text{spec}}$. Recall that for $\tilde{f}_1(\lambda)$, $\hat{\tilde{\mathbf{I}}}_1$ approximately represents the sum of reconstructed transmittances at λ_1, λ_2 and λ_3, as illustrated in Fig. 4.10 (a). The average of reconstructed transmittances can be obtained after dividing $\hat{\tilde{\mathbf{I}}}_1$ by the number of center wavelengths (i.e., dividing by 3). In the case of $\tilde{f}_2(\lambda)$, $\hat{\tilde{\mathbf{I}}}_2$ represents the difference in the transmittance values at λ_1 and λ_2, as shown in Fig. 4.10 (b). As a result, the slope of the transmittance curve can be approximated by dividing $\hat{\tilde{\mathbf{I}}}_2$ by λ_2-λ_1.

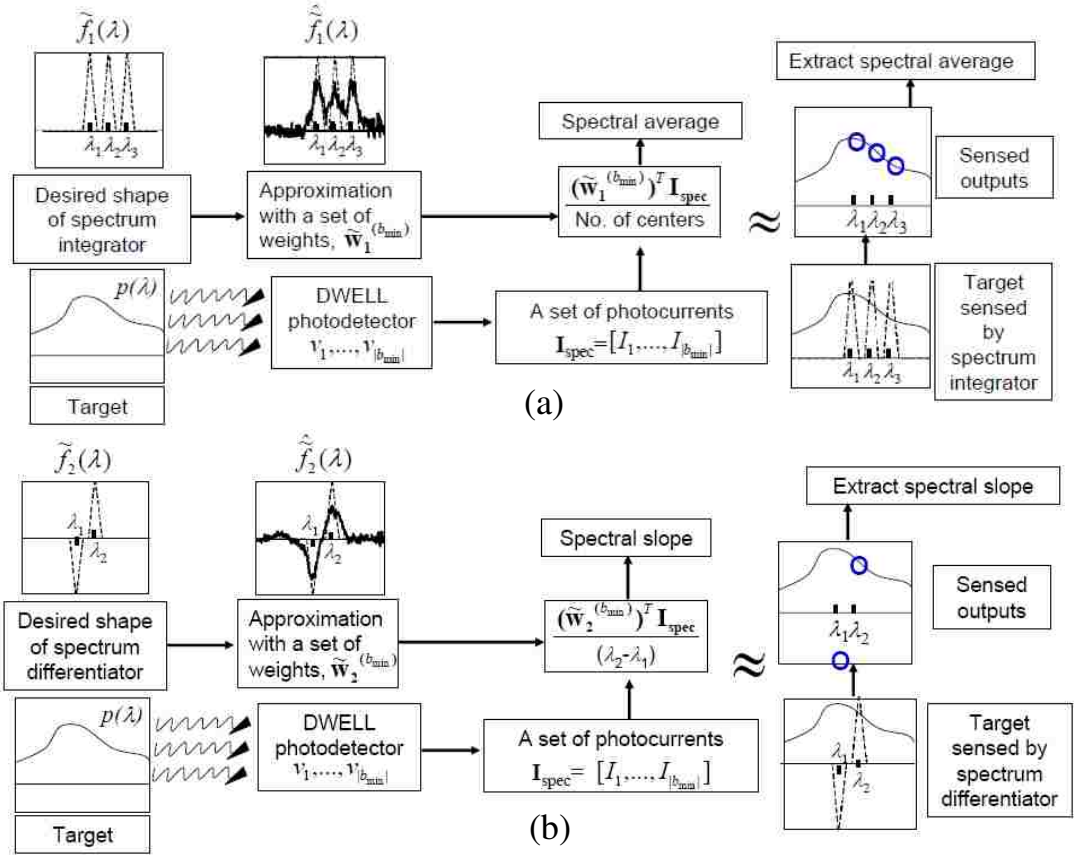

Figure 4.10: Applications of two linearly superpositioned filters (i.e., (a) the spectral integrator $\tilde{f}_1(\lambda)$ and (b) the spectral differentiator $\tilde{f}_2(\lambda)$) to the spectrometry problem of unknown filter target. Approximations $\hat{\tilde{f}}_1(\lambda)$ and $\hat{\tilde{f}}_2(\lambda)$ can extract the spectral average and slope of unknown target, respectively [31].

The experimentally extracted values of the averaged transmittance values (captured by $\hat{\tilde{f}}_1(\lambda)$) and the approximated slope of transmittance (captured by $\hat{\tilde{f}}_2(\lambda)$) are listed in Table 4.6. The experimental reconstructions are compared to the values obtained by using ideal spectral integrator and differentiator (shown in dotted line of Fig. 4.3 (c)). For $\hat{\tilde{f}}_1(\lambda)$, the estimate of the averaged transmittance is within 14% error as compared to the ideal value (i.e., 0.058 in Table 4.6). For $\hat{\tilde{f}}_2(\lambda)$, the estimated slope is within 40% error as compared to the reference (i.e., 0.121 in Table 4.6). In addition, we

observed that the use of the minimal four biases by the MBS algorithm yields consistent results with less than 9% error as compared to values for the other (larger) bias selections

Experimental reconstruction	Number of selected biases				Ideal value
	Min. 4 biases	Best-5 biases	Best-6 biases	All 30 biases	
Averaged transmittance	0.05	0.052	0.052	0.054	0.058
Slope of transmittance	0.073	0.075	0.076	0.08	0.121

Table 4.6: Experimentally extracted averaged transmittance captured by $\hat{\hat{f}}_1(\lambda)$ and slope of transmittance captured by $\hat{\hat{f}}_2(\lambda)$ for different bias selections: minimum four biases, best-five biases, best-six biases and all 30 biases. Results are compared to the reference values obtained by using the ideal spectral integrator and differentiator [31].

4.4.2 Experimental results on target classification

Here, the target spectral filters comprising the classes of spectra are selected as $f_4(\lambda)$ $f_5(\lambda)$ and $f_6(\lambda)$ (7.5-10.5 μm, 8.0-9.0 μm and 8.5-11.5 μm). The photocurrent vector $\mathbf{I}_{\text{class}}$ was measured as the DWELL photodetector was exposed to radiation transmitted through three target filters, $f_4(\lambda)$, $f_5(\lambda)$ and $f_6(\lambda)$ using the same bias sets used in the spectrometry problem of Subsection 4.4.1. For each filter, photocurrent measurements were repeated at least 20 times and averaged to minimize the temporal variability of DWELL photodetector. Recall that the use of the three weight vectors, $\mathbf{w}_4^{(b_{\min})}, \mathbf{w}_5^{(b_{\min})}$ and $\mathbf{w}_6^{(b_{\min})}$ in Subsection 4.3.1 had resulted in optimal matching of the reconstructed transmittances to the actual transmittances $f_4(\lambda)$, $f_5(\lambda)$ and $f_6(\lambda)$. We denoted the corresponding reconstructed matched filters as $\hat{f}_4(\lambda)$, $\hat{f}_5(\lambda)$ and $\hat{f}_6(\lambda)$. For the classification problem, each matched filter is labeled with a specific class number: Class-1 corresponding to $f_4(\lambda)$, Class-2 corresponding to $f_5(\lambda)$, and Class-3 corresponding to $f_6(\lambda)$. In the classifier, $\mathbf{w}_4^{(b_{\min})}, \mathbf{w}_5^{(b_{\min})}$ and $\mathbf{w}_6^{(b_{\min})}$ are linearly combined with the incoming test data, $\mathbf{I}_{\text{class}}$, resulting in three synthesized features: $F_1 = (\mathbf{w}_4^{(b_{\min})})^T \mathbf{I}_{\text{class}}$, $F_2 = (\mathbf{w}_5^{(b_{\min})})^T \mathbf{I}_{\text{class}}$ and $F_3 = (\mathbf{w}_6^{(b_{\min})})^T \mathbf{I}_{\text{class}}$. We denote the

feature vector formed by these synthesized features by $\mathbf{F} = (F_1, F_2, F_3)$. Finally, the classifier assigns this $\mathbf{F}$ to class i^* whose feature value, F_{i^*}, is the highest among the three features; more precisely, $i^* = \arg\max_{i \in \{1,2,3\}} F_i$.

With the minimal four-bias set used, the results show that the classifier has correctly assigned all three test data ($\mathbf{I}_{\text{class}}$) to their respective classes, as shown in Fig. 4.11. In our experimental demonstration, our classifier yielded 100% accuracy. This perfect classification was obtained owing to the fact that the three target spectral filters were reasonably separable. However, if targets are not separable to begin with (i.e., if the extracted features from multiple targets are similar), then we would expect the accuracy of classifier to be reduced.

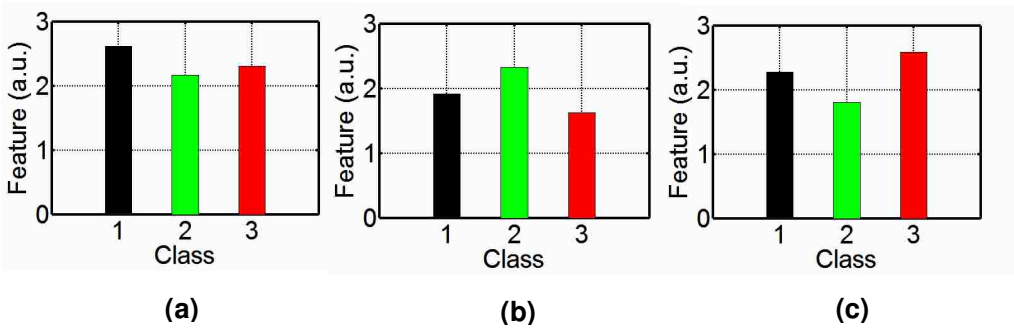

Figure 4.11: Classification results for identifying three experimental test data, $\mathbf{I}_{\text{class}}$. The classifier has successfully assigned the data to Class-1 (see (a)), the data to Class-2 (see (b)), and the data to Class-3 (see (c)) [31].

When we use the best-five biases (gray bars in Fig. 4.12), the best-six biases (blue bars in Fig. 4.12) and all 30 biases (green bars in Fig. 4.12), we also obtain 100% accuracy. This implies that the use of the minimal four biases in the classification problem produced equivalent performance as compared to the result using all the 30 biases.

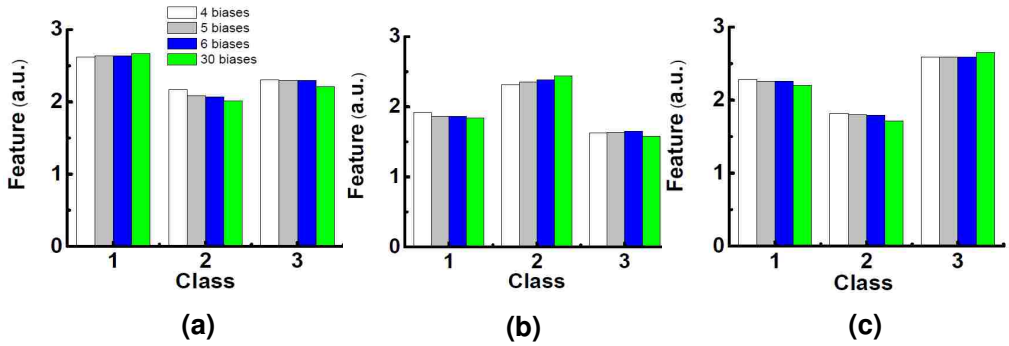

Figure 4.12: Comparison of classification results for minimal four biases (white) to other bias selections: best-five biases (gray), best-six biases (blue) and all 30 biases (green) for identifying the three experimental test data, $\mathbf{I}_{class}$ to (a) Class-1, (b) Class-2 and (c) Class-3. Note that the use of minimum four biases obtained by the MBS algorithm in the UCSS algorithm achieved almost identical result compared to the case using all 30 biases [31].

It is important to mention, that we have observed that the temporal variation of the test data affects the outcome of the classifier if insufficient number of photocurrent measurements is available. For example, over 30% classification error was obtained when we used only 9 photocurrent measurements (per class and averaged). However, when we use 10 or more photocurrent measurements, the classification error was highly improved; for example, with 16 or more photocurrents measurements, 100% classification was achieved.

4.5 Conclusions

We developed a novel data compressive spectral sensing algorithm in conjunction with the bias-dependent spectrally tunable DWELL photodetector that identifies and employs a minimal set of required biases subject to a specified performance level. The identification of a minimal bias set enables the detector to sense only the most relevant and least noisy bias-dependent spectral bands for specific sensing applications. Moreover, the minimal bias set provides a uniformly accurate solution across the collection of specified spectral sensing filters, which captures the corresponding multispectral features for remote-sensing applications of interest. We implemented the algorithm to approximate the collection of six spectral sensing filters and the algorithm identified the minimal set of only four biases for successful approximation of the filter collection. By sensing using the DWELL at these four biases only, we successfully performed two remote-sensing applications that utilize the six spectral sensing filters; these applications were spectrometry of unknown filter target and the classification of three filter targets. In the spectrometry problem, we were able to successfully reconstruct three samples of the transmittance of an unknown test target. In addition, we are able to reconstruct the average of the transmittance across three wavelengths and the slope of the transmittance spectrum at a given wavelength. For the classification problem, we were able to use the DWELL measurement using the four applied biases to successfully classify three spectral filters selected from the collection of six spectral filters.

It is to be noted that in essence, what our approach is capable of doing is to synthesis the effect of an arbitrary optical filter by solely using the optoelectronic properties of the DWELL. The ability to do so successfully gives optical filtering a fresh perspective. Our approach can potentially be used beyond the DWELL sensor; it can be applicable to traditional multi-color infrared detectors, especially if there is overlap in the spectral bands. For example, our approach can potentially be applied to quantum-well detectors which already demonstrated voltage tunable multicolor detection reported in [41]. From a device perspective, this work helps us understand rigorously the reach of the spectral diversity of the DWELL device.

We wish to point out that the MBS and AMBS algorithms can be further enhanced by introducing an extra preliminary stage that eliminates insignificant spectral bands, based on certain SNR requirement, before applying either the MBS or AMBS

algorithms. This can be achieved by building such de-selection process in the metrics used by the MBS and AMBS algorithms.

Finally, effort is underway to implement this new data-compressive DWELL-based sensing paradigm in a focal-plane-array (FPA) platform using a novel custom-designed readout integrated circuit, which can directly output spectral signatures or object classes in near real-time spectral sensing. In Chapters 5 and 6 we take this work to the next level by investigating a sensitivity of data-compressive sensing algorithm and developing a continuous time-varying biasing approach under an acquisition time constraint for hardware (FPA) implementation.

Chapter 5

Sensitivity Analysis of Generalized Data Compressive Multispectral Sensing Algorithm

Recently, the "smart" pixel readout integrated circuit (ROIC) has been developed by incorporating the signal and image processing algorithms to extract and process the captured data in real time. Traditional ROICs [42] were mainly simple interfaces between the FPA and the image capture and processing hardware. Hence, the smart-pixel FPA can be more versatile than its predecessors through the implementation of various programmable modes of operation. The research group at MIT Lincoln Laboratory has developed new Digital-pixel FPA ROICs [43] with the on-chip processing capability, which can implement non-uniformity correction, image stabilization and more. Recently, Prof. Zarkesh-ha and colleagues at the UNM have proposed a reconfigurable and intelligent ROIC (iROIC) [44] with a low cost and a small volume for low electrical power consumption, as shown in Fig. 5.1 (a). The iROIC can offer variable or adaptive biasing to electrically-tunable DWELL FPA at pixel level with a large bipolar bias swing (in a range of +/- 5V). In addition, the iROIC provides the arithmetic capability at pixel level through a programmable analog function unit as shown in Fig. 5.1 (b). Specifically, the analog function unit allows the computation of weighted sum between the pixel's analog outputs (the photocurrents) and a set of analog coefficients (a set of prescribed weights). Our main objective is to implement the compressive spectral sensing algorithm (the UCSS algorithm described in Chapter 4) on the UNM's iROIC for real time target detection and classification.

Preliminary test results with the iROIC prototype showed a noise level around 10 mV, which results in restricting the number of bits to represent weights to be maximum 9 bits for the digital-to-analog conversion in the analog function unit. If 10-bit

representation is used, the last bit corresponds to around 9.8 mV, which is less than the 10 mV noise floor. As a result, this last bit simply becomes a noise-dominant bit and is of no use for further processing. More bits are wasted as we use 11 bits or higher. Also in the design of analog function unit, as a larger number of bits is used, the required area for the transistors is increased immensely, for example, the required area for n bits is 2^{n-1}A, where A is the area for n = 1. Thus, the use of 10 bits or more results in a high cost and large power dissipation ROIC.

In order to implement the UCSS algorithm on the iROIC, we need to verify the sensitivity of algorithm weights against the bit-number representation by addressing two following questions: (1) can we successfully perform the UCSS algorithm with weights represented in 9 bits or less? and (2) what is the minimum number of bits required? This chapter addresses these two questions by demonstrating the algorithm through two MS sensing applications.

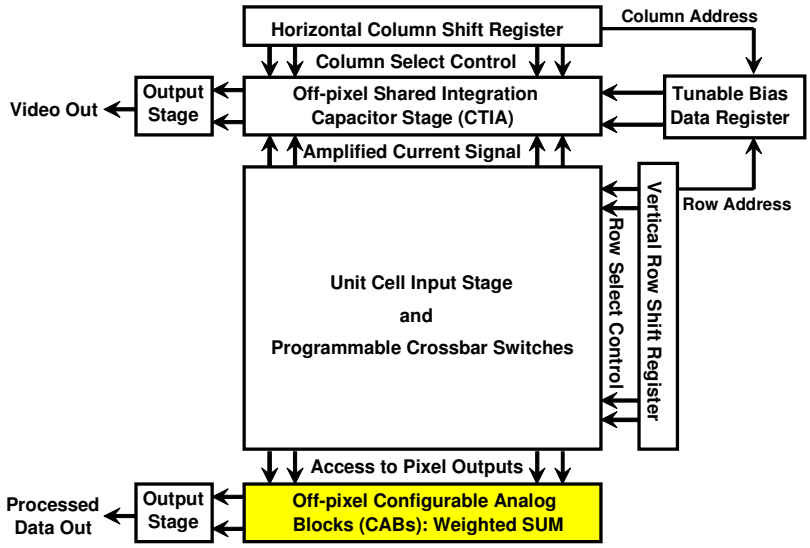

(a)

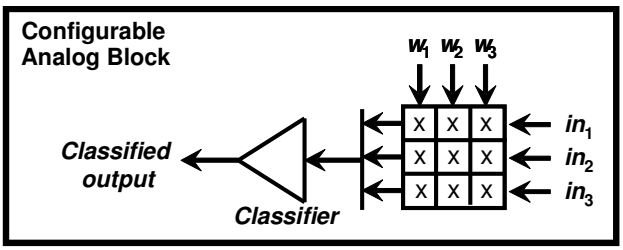

(b)

Figure 5.1: (a) Block diagram of the entire architecture of iROIC. The programmable analog block within iROIC is shown in yellow. (b) Functions of the analog block: weighted superposition of photocurrent inputs (in_1, in_2 and in_3) with weights (w_1, w_2 and w_3) and classification among three weighted superpositions [44].

5.1 Sensitivity of algorithm weights against bit-number representation

The sensitivity of UCSS algorithm against the bit representation was validated for target spectrometry and classification problems. For a spectrometry problem, we considered two LWIR targets: a broadband filter centered at 9.0 μm as shown in Fig. 5.2 (black dotted line) and a narrowband filter centered at 8.5 μm as shown in Fig. 5.3 (black dotted line). According to the experiment procedure in Subsection 4.4.1, two photocurrent vectors ($\mathbf{I}_1$ and $\mathbf{I}_2$) were measured by the DWELL photodetector using minimal four biases (i.e. {-3.0, -0.8, 1.0, 2.8 V}). With photocurrent vectors, the spectrum-reconstruction procedure of UCSS algorithm (i.e. $\hat{I}_{i,n} = \mathbf{w}_n{}^T\mathbf{I}_i$ at λ_n and i=1,2) as described in Subsection 4.4.1 was followed to reconstruct transmittances of both targets. The reconstructed targets are shown in Figs 5.2 (solid blue line) and 5.3 (solid blue line).

To identify the minimum number of bits for acceptable target reconstruction, the weight vector $\mathbf{w}_n$ were converted to six different bit-number representations (i.e. from 6 to 12 bits). Since $\mathbf{w}_n$ consists of positive and negative numbers, the signed number representation is required to encode negative numbers. A range of signed numbers is defined by -2^{N-1} to $(2^{N-1}-1)$ for N-bit integer. The bit-number representation process is described as follows. First, the minimum weight $w_{\min,n}$ within $\mathbf{w}_n$ is identified. Second, we compute a scaling factor by taking a ratio (i.e. $-2^{N-1}/w_{\min,n}$) if $w_{\min,n}$ is negative or a ratio (i.e., $(2^{N-1}-1)/w_{\min,n}$) if $w_{\min,n}$ is positive. Finally, $\mathbf{w}_n$ is normalized by the scaling factor and is then quantized, denoted by $\mathbf{w}_{N,n}$ for N-bit integer. We obtained $\mathbf{w}_{N,n}$ for N = 6, 8, 9, 10, 11, 12 bits.

With $\mathbf{w}_{N,n}$, targets were reconstructed as shown in Figs 5.2 (solid red lines) and 5.3 (solid red lines). By visual inspection, results show that for 6-bit representation, reconstructions in Figs 5.2 (a) and 5.3 (a) were poor as compared to those obtained with $\mathbf{w}_n$ (i.e. Figs 5.2 (solid blue line) and 5.3 (solid blue line)). This is due to a large weight error between $\mathbf{w}_{6,n}$ and $\mathbf{w}_n$. For 8-bit or higher, good reconstructions as shown in Figs 5.2 (b-f) and 5.3 (b-f) were obtained as a result of significant reduction in the weight error. To accurately quantify the weight error, we computed the relative error e between the original reconstruction $f(\lambda)$ by $\mathbf{w}_n$ (solid blue line in Figs 5.2 and 5.3) and

the reconstruction $\hat{f}(\lambda)$ by $\mathbf{w}_{N,n}$ (solid red line in Figs 5.2 and 5.3) defined by the following formula,

$$e = 100 \times \frac{\int_{\lambda_{\min}}^{\lambda_{\max}} \left(f(\lambda) - \hat{f}(\lambda) \right)^2 d\lambda}{\int_{\lambda_{\min}}^{\lambda_{\max}} f^2(\lambda) d\lambda}. \quad (17)$$

Calculated errors for all six bit-number representations are tabulated in Table 5.1. We confirmed that using $\mathbf{w}_{6,n}$ (6-bit representation), poor reconstructions were observed having over 50% error. With $\mathbf{w}_{8,n}$ (8-bit representation), the error was significantly reduced down to less than 30%. Thus, we demonstrated the UCSS algorithm using minimum 8 bits can successfully reconstruct the transmittance of target on the iROIC. Next, we use minimum 8 bits to represent weight vectors for classifying three matched filter targets.

Experimental reconstruction	*e* (%)					
	6 bit	8 bit	9 bit	10 bit	11 bit	12 bit
(a) Broadband filter	50.9	22.6	11.2	6.4	4.2	2.2
(b) Narrowband filter	64.4	28.3	12.8	8.6	5.5	3.1

Table 5.1: Relative error *(e)* between the original reconstruction $f(\lambda)$ by $\mathbf{w}_n$ and the reconstruction $\hat{f}(\lambda)$ by $\mathbf{w}_{N,n}$ for six different bit-number representations.

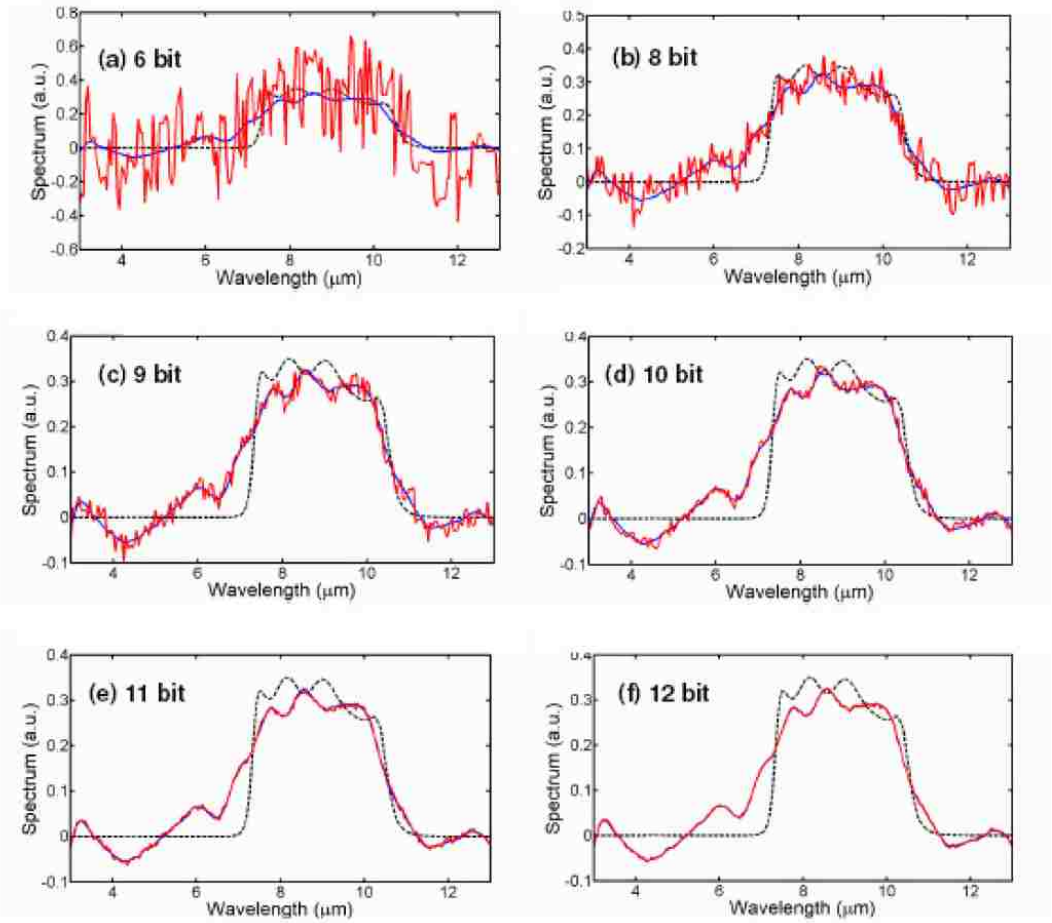

Figure 5.2: Experimental reconstructions (solid red lines) of the broadband filter target using the UCSS algorithm with minimal four biases (out of 30) and weights represented in (a) 6-bit integer, (b) 8-bit integer, (c) 9-bit integer, (d) 10-bit integer, (e) 11-bit integer and (f) 12-bit integer. Dotted black lines represent the actual filter transmittance and solid blue lines represent the reconstructed filter transmittance using original weights $\mathbf{w}_n$ without bit-number representation.

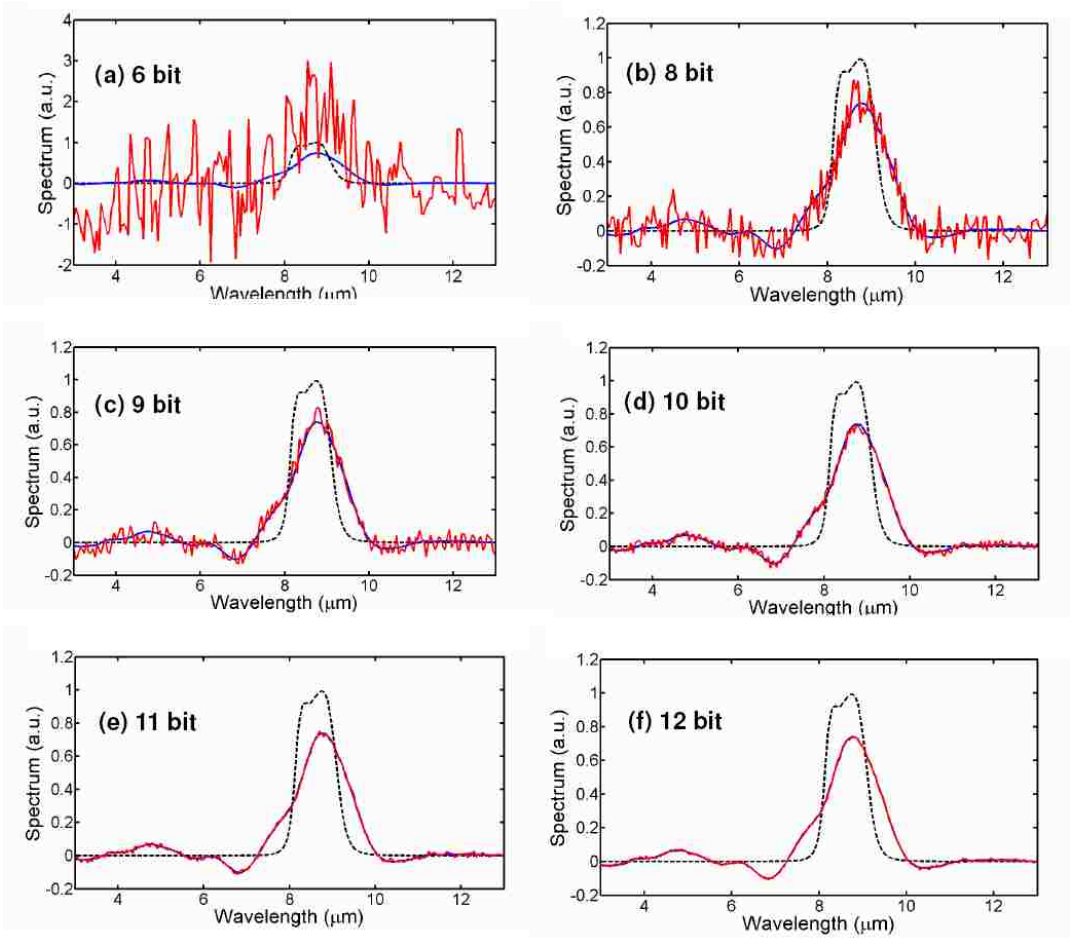

Figure 5.3: Experimental reconstructions (solid red lines) of the narrowband filter target using the UCSS algorithm with minimal four biases (out of 30) and weights represented in (a) 6-bit integer, (b) 8-bit integer, (c) 9-bit integer, (d) 10-bit integer, (e) 11-bit integer and (f) 12-bit integer. Dotted black lines represent the actual filter transmittance and solid blue lines represent the reconstructed filter transmittance using original weights $\mathbf{w}_n$ without bit-number representation.

We selected the same problem of classifying three spectral matched filters, $f_4(\lambda)$ $f_5(\lambda)$ and $f_6(\lambda)$ using minimal four biases {-3.0, -0.8, 1.0, 2.8 V} as demonstrated in Subsection 4.4.2. Also recall that $\mathbf{w}_4^{(b_{\min})}, \mathbf{w}_5^{(b_{\min})}$ and $\mathbf{w}_6^{(b_{\min})}$ were the corresponding weight vectors, which successfully approximated the transmittances of matched filter targets. To test the sensitivity of classification weights against the bit-number representation, $\mathbf{w}_4^{(b_{\min})}, \mathbf{w}_5^{(b_{\min})}$ and $\mathbf{w}_6^{(b_{\min})}$ are now represented in 8-bit integer denoted by $\boldsymbol{w_4}$, $\boldsymbol{w_5}$ and $\boldsymbol{w_6}$ as shown in Table 5.2.

Original weight vectors	Weight vectors in 8-bit integer
$\mathbf{w}_4^{(b_{\min})}$ = [0.294 -2.084 0.601 0.191]	$\boldsymbol{w_4}$ = [15 -109 32 10]
$\mathbf{w}_5^{(b_{\min})}$ = [0.462 -1.203 -0.095 -0.152]	$\boldsymbol{w_5}$ = [24 -63 -5 -8]
$\mathbf{w}_6^{(b_{\min})}$ = [0.218 0.055 -2.438 0.456]	$\boldsymbol{w_6}$ = [11 3 -128 24]

Table 5.2: (Left) original weight vectors obtained by the UCSS algorithm with minimal four biases for approximating three matched filters $f_4(\lambda)$ $f_5(\lambda)$ and $f_6(\lambda)$ and (Right) weight vectors in 8-bit representation.

$\boldsymbol{w_4}$, $\boldsymbol{w_5}$ and $\boldsymbol{w_6}$ are linearly combined with the test data (the pixel output) in the classifier, extracting a feature vector. The classifier then assigns a feature vector to a respective class by finding the largest feature. Results in Fig. 5.4 demonstrate that the classifier with 8-bit weights has correctly assigned all three incoming test data to respective classes.

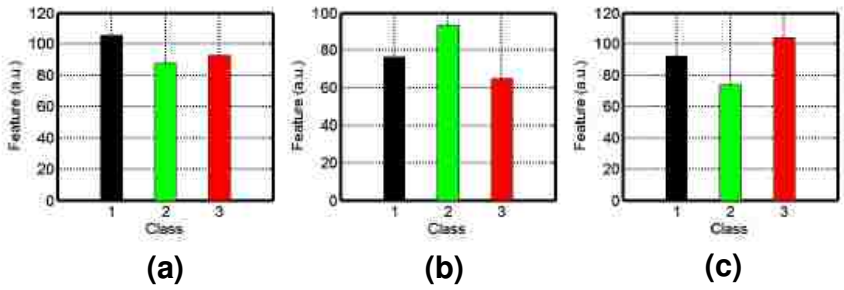

Figure 5.4: Classified outputs for three experimental test data. The classifier has correctly assigned the data to Class-1 (shown in (a)), the data to Class-2 (shown in (b)), and the data to Class-3 (shown in (c)). Results demonstrate that the UCSS algorithm using minimum 8 bits can successfully perform matched filter-based classification on the iROIC.

5.2 Conclusions

To implement the algorithm on the iROIC, we identified the minimum number of bits, by applying our compressive spectral sensing algorithm for object spectrometry and classification problems with varying weights in six different bit-number representations (from 6 to 12 bits). By simulation, we successfully reconstructed transmittances of two filter objects and correctly classified three experimental test objects with a minimum 8 bits. The minimum 8 bits satisfies the design requirement of iROIC, which is constrained to use 9 bits or less.

Recently, we have found that the analog unit on the iROIC can be further simplified by eliminating the multiplication and superposition processes of our spectral tuning algorithm. This can be achieved by generalizing the algorithm to find a continuous time-varying bias waveform, which can also be a solution for a specific MS sensing application. Traditionally, the emissivity of an object was reconstructed by performing the weighted superposition of photocurrents by the spectral tuning algorithm using discrete set of static biases. Unlike the traditional approach, a continuous time-varying biasing approach reconstructs the object's emissivity by accumulating the photocurrent of an object based on a prescribed bias waveform without requiring data-processing steps associated with weights. In the next chapter, we report the generalized spectral tuning algorithm for a continuous-time biasing approach and validate this new algorithm for object spectrometry and classification problems and results are compared to the conventional spectral tuning algorithm.

Chapter 6

Continuous Time-varying Biasing Approach for Spectrally Tunable Infrared Detectors

In the algorithmic spectral tuning approach, demonstrated earlier in Chapters 2 and 4, the reconstruction of an object's emissivity at an arbitrarily specified spectral-sensing window of interest in the long-wave infrared region was achieved by forming an off-sensor weighted superposition of the bias-dependent photocurrents of a DWELL photodetector. In this approach, the acquisition time was held constant for each of the applied biases. Here, a generalization of this approach is introduced that duplicates the capabilities of the algorithmic spectral-tuning approach by applying a continuously varying bias-voltage function, designed for each spectral-sensing window of interest, over a fixed acquisition time without the need to perform a weighted superposition. This generalization is particularly relevant to the on-sensor implementation of the algorithmic spectral tuning approach in DWELL FPAs, where the photocurrent integration time is governed by the frame rate and on-sensor processing is undesirable. The continuous-time biasing can be easily implemented in the readout circuit of the FPA. The approach is validated by means of simulations, in the context of spectrometry and object classification, using real experimental data for the DWELL's bias-dependent spectral response, photocurrent, and SNR.

6.1 Motivation of the continuous time-varying biasing approach

As demonstrated in Chapter 2, the DWELL photodetector developed by our group offers electrically controlled spectrally tunable responses in the mid-IR region as shown in Fig. 6.1. (We will use the spectral data of this device throughout this chapter as we demonstrate the sensing algorithms to be developed.) Specifically, a single DWELL photodetector can perform the task of a multispectral (MS) IR detector by changing its bias voltage without requiring optical-filter wheels. The DWELL's spectral tunability, as it stands, however, is not sufficient to provide the high resolutions required by many spectral-sensing problems.

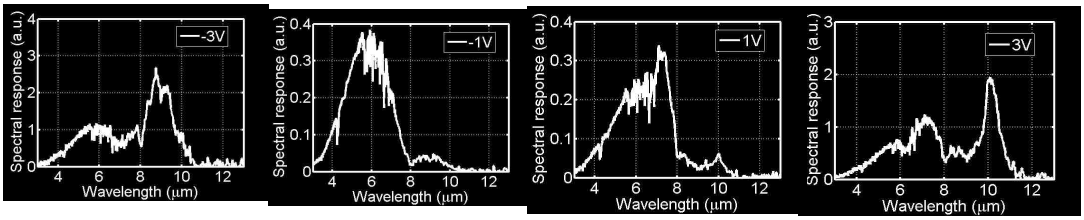

Figure 6.1: Bias-tunable spectral responses of the DWELL photodetector at 60K device temperature by varying applied biases in the range from -3 to 3 V [31].

To extend the MS capability of the DWELL photodetector, the DWELL's bias-controlled spectral tunability was substantially enhanced by means of a post-processing technique, termed here as the spectral tuning (ST) algorithm [21,22,24]. The extended MS capabilities demonstrated by the ST algorithm include high-resolution, narrowband spectral filtering, as well as object spectrometry and classification [28,31]. We emphasize that none of these capabilities involved the use of spectral filters. The underlying principle of the ST algorithm is to sense an object with the DWELL photodetector sequentially at prescribed bias voltages, yielding a set of bias-dependent photocurrents. Then, the ST algorithm performs a linear superposition of photocurrents with a set of weights to reconstruct the emissivity of an object at a given wavelength. Each set of weights is designed by the ST algorithm for a specific spectral filter of interest. For each spectral filter of interest, the so-called superposition photocurrent best approximates the ideal photocurrent that would have been obtained while using a combination of a broadband detector and the desired spectral filter. To date, the ST algorithm has been developed and demonstrated using a discrete set of static biases. The three data-processing steps involved include the calculation of weights corresponding to

each spectral tuning filter, multiplication of weights with sensed photocurrents and the superposition of the weighted photocurrents to yield the superposition photocurrent.

In this chapter we develop the concept for novel implementation of the ST algorithm within the readout circuit (ROIC) of a DWELL-based FPA without resorting to multiplying photocurrents by or performing photocurrent additions algebraically. Motivated by the electronics of a trans-impedance amplified based ROIC, works, namely by feeding the photocurrent at each bias into an integrating capacitor that yields an integrated photocurrent (charge) for each integration time [46-48], the idea here is to absorb both the multiplications (by weights) and additions of the ST algorithm in the photocurrent integration process by appropriately adjusting the bias of the DWELL continuously in sync within the integration time. For example, if we have only two photocurrents, corresponding to two bias levels v_a and v_b, with infinite SNRs, multiplying the first and second by the weights 1 and 5, respectively, and summing up the two can be done in one step via the integration of the first photocurrent over a certain duration followed by the integration of the second photocurrent over five times the integration time of the first one while keeping the total integration time fixed. In this simple example the bias is held constant at level v_a for one unit of time and then changed to level v_b for five units of time, as the photocurrent is integrated seamlessly over the acquisition time. To achieve this effect for more general superposition schemes while incorporating the effects of signal-to-noise, we will need to generalize the ST algorithm to allow for continuous, time-varying biases within a fixed integration time. As a result of the generalization, the algorithm will yield, for each desired spectral filter, a time-varying bias waveform.

Since the sign of weights can be positive or negative, two waveforms are generally obtained that together span the integration time: a “positive” waveform corresponding to the positive weights and a “negative” waveform corresponding to the negative weights. The integrated photocurrent corresponding to the “positive” waveform is added to the negative of the integrated photocurrent corresponding to the “negative” waveform, yielding the subtracted photocurrent. With this approach, the superposition photocurrent representing the spectral measurement is directly extracted from the ROIC [43,44] as the ROIC can be configured to apply the positive and negative bias waveforms sequentially at the two integrated photocurrents at each detector in the FPA. This chapter will focus on the algorithmic aspects of the proposed ST technique.

6.2 Review of the spectral tuning algorithm and application to object spectrometry and classification

In this section, we begin by reviewing germane aspects of the ST algorithm drawing freely from Chapters 2 and 4. As you may find, the ST algorithm had been reviewed earlier in Chapters 2 and 4. However it is important to review its concept and applications again in this chapter since we will further generalize the algorithm to perform a new continuous time-varying biasing. We consider an object of interest, f, whose emissivity in the LWIR region is denoted by $e(\lambda)$. Suppose that a DWELL photodetector is used to probe the object illuminated by a blackbody at the bias voltages, $v_1,\ldots, v_m$, yielding a set of bias-dependent photocurrents, $I_1,\ldots, I_m$. In principle, the photocurrent I_k corresponding to the k^{th} bias can be expressed as an inner product between the emissivity of an object and each one of the DWELL's spectral responses with the bias-dependent noise [22,31,35]

$$I_k = \int_{\lambda_{\min}}^{\lambda_{\max}} e(\lambda) R_k(\lambda) d\lambda + N_k, \tag{18}$$

where $R_k(\lambda)$ is the spectral response of DWELL at the k^{th} bias in the wavelength interval $[\lambda_{\min}, \lambda_{\max}]$, and N_k is the noise associated with $R_k(\lambda)$.

We specify the transmittance of a *desired* tuning filter $r(\lambda;\lambda_n)$ that would be used to estimate $e(\lambda)$ at the tuning wavelength λ_n. For $r(\lambda;\lambda_n)$, the ST algorithm [22,28] calculates a weight vector, $\mathbf{w}_n = [w_1,\ldots,w_m]$ using (1) in Chapter 2, which is linearly combined with the spectral responses $R_1,\ldots,R_m$, yielding the *algorithmic tuning filter* $\hat{r}(\lambda;\lambda_n)$. The weights are derived so that the algorithmic tuning filter $\hat{r}(\lambda;\lambda_n)$ best approximates the hypothetical tuning filter $r(\lambda;\lambda_n)$ in the sense of minimizing the wavelength-integrated mean squared error. Then, the weight vector $\mathbf{w}_n$ is linearly synthesized with the photocurrents, $I_1,\ldots, I_m$, yielding the superposition photocurrent $\hat{\mathrm{I}}$ as expressed by

$$\hat{\mathrm{I}} = \sum_{i=1}^{m} w_i I_i. \tag{19}$$

The superposition photocurrent, $\hat{\mathrm{I}}$, is usually computed with positive and negative signs since weights in $\mathbf{w}_n$ can be either positive or negative. It reconstructs the ideal photocurrent that we would have captured by the DWELL photodetector looking at the

object through the tuning filter $r(\lambda;\lambda_n)$. It is to be noted that if the width of the filter $r(\lambda;\lambda_n)$ is sufficiently narrow, then the ST algorithm reconstructs the emissivity of an object at λ_n without utilizing any physical spectral filters.

To demonstrate the ST algorithm, we will show two representative MS sensing examples: (1) spectrometry of LWIR filter object and (2) statistical classification of LWIR filter object based on the spectral matched filtering [31].

For the spectrometry example, we considered a triangular narrowband tuning filter as $r(\lambda;\lambda_n)$ with 0.5 μm width and λ_n = 8.8 μm to sample the emissivity of LWIR filter object, $e(\lambda)$, at λ_n as illustrated in Fig. 6.2. Using (1) in Chapter 2, we calculated $\mathbf{w}_n$ for the algorithmic tuning filter $\hat{r}(\lambda;\lambda_n)$ using minimal four biases, {-3.0, −0.8, 1.0, 2.8 V}, selected by the Minimal-Bias-Set (MBS) algorithm [31]. The MBS algorithm is the bias selection algorithm based on an exhaustive search approach, which identifies a minimal set of biases required for multiple sensing applications of interest. The search process of MBS algorithm is described in Subsection 4.2.1 of Chapter 4. The algorithmic tuning filter $\hat{r}(\lambda;\lambda_n)$ is shown in Fig. 6.2 (solid black). We also simulated photocurrents, $I_1,\ldots, I_4$, for these four biases using (18) with actual noise values available from the DWELL's SNRs. The reconstructed sample $\hat{e}(\lambda;\lambda_n)$ was then obtained by forming a linear superposition between $\mathbf{w}_n$ and photocurrents ($I_1,\ldots, I_4$) according to (19). We also generated the estimated emissivity, $e(\lambda;\lambda_n)$, resulting from sampling $e(\lambda)$ by $r(\lambda;\lambda_n)$, which is used as a reference measurement for the ST algorithm. The reconstructed emissivity $\hat{e}(\lambda;\lambda_n)$ by the ST algorithm is 0.134 and as compared to the benchmark value ($e(\lambda;\lambda_n)$ = 0.171), $\hat{e}(\lambda;\lambda_n)$ is within 22% error.

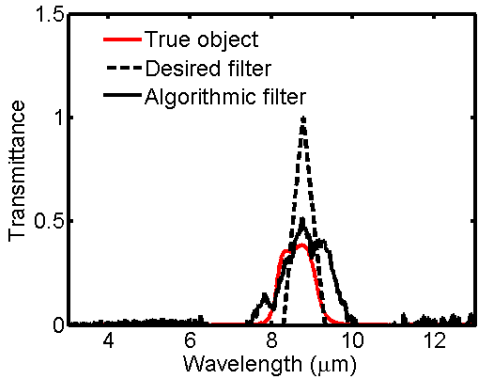

Figure 6.2: Desired triangular narrowband tuning filter, $r(\lambda;\lambda_n)$ with λ_n = 8.8 μm, whose transmittance is shown by the dashed line. Transmittance of algorithmic tuning filter, $\hat{r}(\lambda;\lambda_n)$, as shown in solid black line, was obtained by the ST algorithm [22,28] using the minimal set of four biases, {-3.0, –0.8, 1.0, 2.8 V} identified by the MBS selection algorithm reported in [31]. The algorithmic tuning filter $\hat{r}(\lambda;\lambda_n)$ is implemented via post processing (without using any physical spectral filters) to reconstruct sample of the emissivity of an object (in red) at λ_n = 8.8 μm.

For the classification example, we selected three actual spectral filters, $r_1(\lambda;\lambda_1)$, $r_2(\lambda;\lambda_2)$ and $r_3(\lambda;\lambda_3)$ with centers at λ_1 = 9 μm, λ_2 =8.5 μm and λ_3 = 10 μm as shown in Fig. 6.3 (dashed line), as objects that need to be classified once each one of them is probed by the DWELL detectors using a set of prescribed biases. The classification is based on the spectral matched filtering technique, which uses multiple weight vectors (as many as the number of spectral matched filters considered) obtained from the ST algorithm to initialize a classifier. The classifier then performs a weighted linear superposition of the bias-dependent photocurrents, yielding superposition features. Based on the extracted features, the classifier labels the object of interest. In this example, we selected $r_1(\lambda;\lambda_1)$ as the test object of interest to be classified. The classification process is described as follows.

Using (1) in Chapter 2, while using the same bias set as before, {-3.0, –0.8, 1.0, 2.8 V}, we obtained the corresponding three weight vectors, $\mathbf{w}_1$, $\mathbf{w}_2$ and $\mathbf{w}_3$, which yield the approximated spectral filters, $\hat{r}(\lambda;\lambda_1)$, $\hat{r}(\lambda;\lambda_2)$ and $\hat{r}(\lambda;\lambda_3)$, that are optimally matched to $r_1(\lambda;\lambda_1)$, $r_2(\lambda;\lambda_2)$ and $r_3(\lambda;\lambda_3)$, respectively. The approximated filters $\hat{r}(\lambda;\lambda_1)$, $\hat{r}(\lambda;\lambda_2)$ and $\hat{r}(\lambda;\lambda_3)$ are termed *algorithmic spectral matched filters* to be used to classify the test filter object, $r_1(\lambda;\lambda_1)$. Transmittances of three spectral matched filters are shown in Fig. 3 (solid black line).

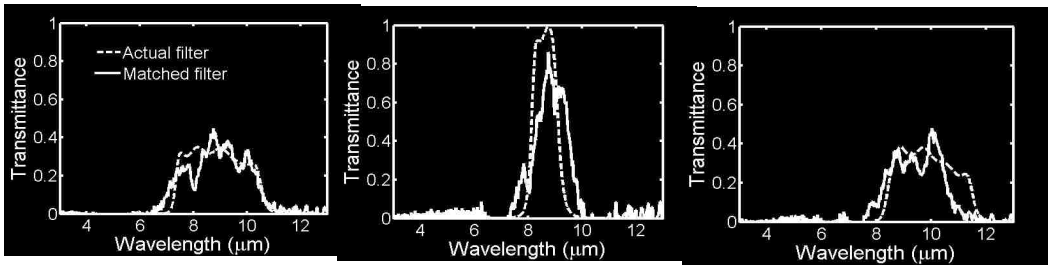

Figure 6.3: Transmittances of three spectral matched filters [31], $\hat{r}(\lambda;\lambda_1)$ (left), $\hat{r}(\lambda;\lambda_2)$ (middle) and $\hat{r}(\lambda;\lambda_3)$ (right) in solid black line were obtained by the ST algorithm using same minimal set of four biases, {-3.0, –0.8, 1.0, 2.8 V}. Transmittances of actual spectral filters, $r_1(\lambda;\lambda_1)$, $r_2(\lambda;\lambda_2)$ and $r_3(\lambda;\lambda_3)$ are shown in dashed line. These three matched filters are used to classify the filter object, $r_1(\lambda;\lambda_1)$.

We simulated the photocurrent vector, $\mathbf{I}_{\text{class}}= [I_1,\ldots, I_4]$, with (18) just as the DWELL photodetector probed the emissivity transmitted through the test filter object, $r_1(\lambda;\lambda_1)$ using the biases, {-3.0, –0.8, 1.0, 2.8 V}. We considered $\mathbf{I}_{\text{class}}$ as the test data to classify. For the classification, we labeled three matched filters, $\hat{r}(\lambda;\lambda_1)$, $\hat{r}(\lambda;\lambda_2)$ and $\hat{r}(\lambda;\lambda_3)$ with Class 1, Class 2 and Class 3 respectively. Based on (19), $\mathbf{w}_1$, $\mathbf{w}_2$ and $\mathbf{w}_3$ were linearly combined with $\mathbf{I}_{\text{class}}$, extracting three synthesized features,

$$F_1 = (\mathbf{w}_1)^T \mathbf{I}_{\text{class}} = 0.519, \quad F_2 = (\mathbf{w}_2)^T \mathbf{I}_{\text{class}} = 0.428 \quad \text{and} \quad F_3 = (\mathbf{w}_3)^T \mathbf{I}_{\text{class}} = 0.457.$$

The feature vector was formed by $\mathbf{F} = [F_1, F_2, F_3] = [0.519, 0.428, 0.457]$ as shown in Fig. 6.4. Based upon the following classification rule, $i^* = \arg\max_{i\in\{1,2,3\}} F_i$ reported in [31], the classifier assigned this $\mathbf{F}$ to Class 1 since the feature value F_1 was the highest among the three features. As a result, the classifier has successfully classified the test data $\mathbf{I}_{\text{class}}$ by assigning it to Class 1.

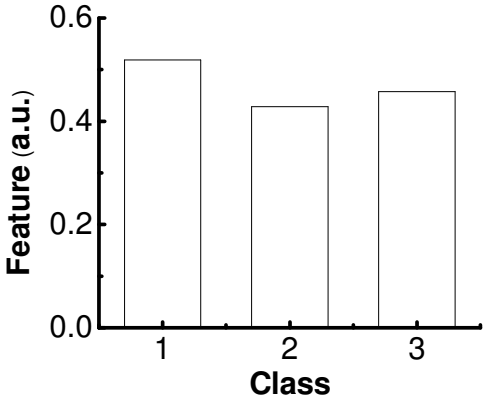

Figure 6.4: Feature vector $\mathbf{F}$ for classifying the simulated test data, $\mathbf{I}_{\text{class}}$. Based on $\mathbf{F}$, the classifier has correctly assigned $\mathbf{I}_{\text{class}}$ to Class 1.

6.3 Generalized spectral tuning algorithm

In this section, we describe the generalized spectral tuning (GST) algorithm to achieve a continuous time-varying biasing with acquisition time constraint. Our solution to the generalization is based upon a discrete-time approximation of the continuous-time problem.

Any continuous time-varying function can be approximated by a piecewise-constant function with jumps occurring at fixed time increments; an example is shown in Fig. 6.5.

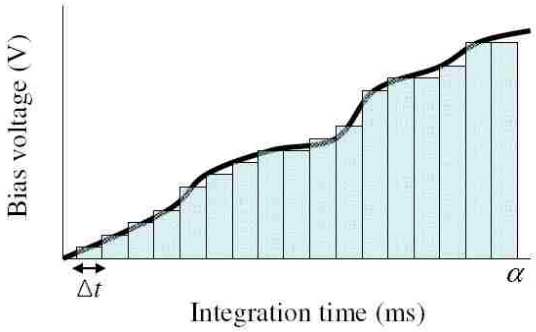

Figure 6.5: Approximation of a continuous time-varying biasing waveform (solid black line) by the discretization (blue shaded region) with a constant interval Δt within the total integration time α.

For an arbitrary bias function $V(t)$, $t \in [0,\alpha]$, let $I_V(t)$ represent the dynamic photocurrent of the DWELL when it is driven by the bias function V. Now consider a desired spectral filter f that we can approximate with a superposition spectral filer according to the bias set $B(f)= \{B_1(f),\ldots, B_k(f)\}$, each applied for a duration Δt, such that

$$\hat{f} = \sum_{i=1}^{k} w_i R_{B_i(f)}(\lambda), \tag{20}$$

where w_i and $R_{B_i(f)}(\lambda)$ are the weight and the spectral response of DWELL at $B_i(f)$.

Based on this continuous-time approximation, the superposition photocurrent $\hat{I}$ in (19) can be reinterpreted as the integration of weighted photocurrents over α. As such, (19) can be cast as

$$\hat{I} = \int_0^{\alpha} w_f(t) I_{B(f)}(t)\, dt, \tag{21}$$

where the piece-wise constant weight function $w_f(t)$ and piece-wise constant

photocurrent $I_{B(f)}(t)$ are defined as $w_f(t) = w_i$ and $I_{B(f)}(t) = I_i$ for $(i\text{-}1)T_{i-1} \le t \le iT_i$, with $\Delta t = iT_i - (i\text{-}1)T_{i-1}$, $i = 1,\ldots, k$.

Motivated by the form of (21), we can further extend (21) to find $\hat{I}$ without performing multiplications and superpositions with $w_f(t)$ as expressed by

$$\hat{I} = \int_0^{\alpha} I_{\hat{B}(f)}(t)dt, \tag{22}$$

where $\hat{B}(f)$ is a bias function designed so that it absorbs the factor, $w_f(t)$ in (21). The idea is to embed the multiplication and superposition processes in the photocurrent integration by properly adjusting the integration time Δt within α instead of scaling each photocurrent with $w_f(t)$. A key task is now to find $\hat{B}(f)$.

The question is then should we simply scale Δt with the corresponding weight in order to blend the weight information into the integration time? The answer is no. As shown in (1), the weights are calculated by the ST algorithm using the detector's SNRs. It is to be noted that the SNR is proportional to the integration time of the detector [22], so, for instance, if Δt is reduced according to some weight factor, so does the SNR of the integrated photocurrent. The new SNR, if lower than the old value, could result in the error in reconstructing the emissivity of an object. We next provide a solution to $\hat{B}(f)$.

We begin by normalizing entire set of weights $\{w_i\}$ by their absolute minimum,

$$\hat{w}_i = \frac{w_i}{\min_{i=1,\ldots k} | w_i |}. \tag{23}$$

Then each Δt is scaled by the absolute normalized weight $| \hat{w}_i |$ denoted by $b_i = | \hat{w}_i | \Delta t$, where $i = 1,\ldots, k$ and k is the number of bias-time intervals (or bias slots). This weight normalization guarantees each b_i to be equal to or greater than Δt so that the SNR corresponds to b_i will not be reduced. In addition, b_i indicates that the important bias has a longer bias-time interval than the weak bias. The total integration time, $\tau(\Delta t)$, is then calculated using the following equation

$$\tau(\Delta t) = \sum_{i=1}^{k} b_i = \Delta t \sum_{i=1}^{k} | \hat{w}_i |, \qquad (24)$$

which is greater than Δt. As a result, a continuous time-varying biasing waveform $\hat{\mathrm{B}}(f)$ with adjusted integration time is obtained as illustrated in Fig. 6.6. It is to be emphasized that $\hat{\mathrm{B}}(f)$ is obtained without using any knowledge from the target in a scene (source independent). The weights absorbed in $\hat{\mathrm{B}}(f)$ guarantee the optimal approximation of a desired spectral filter *f*.

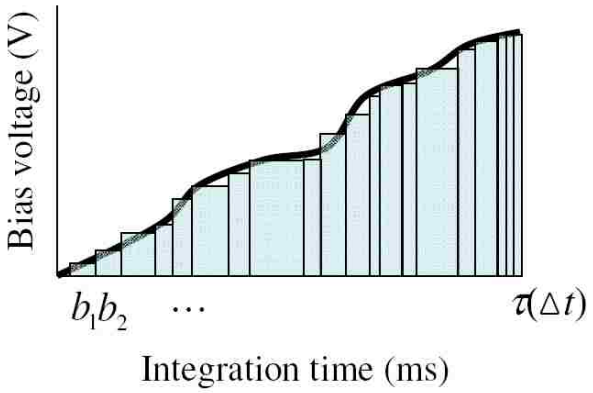

Figure 6.6: Illustration of a continuous time-varying biasing waveform $\hat{\mathrm{B}}(f)$ (blue shaded region) obtained by the GST algorithm using the adjusted integration time b_i within the total integration time $\tau(\Delta t)$.

As we mentioned before, the sign of the weights can be either positive or negative, so two types of waveforms for integrating photocurrents, $I_{\hat{\mathrm{B}}(f)}(t)$, are obtained: (1) a negative waveform corresponding to negative sign of weights and (2) a positive waveform corresponding to positive sign of weights. In order to find $\hat{\mathrm{I}}$, we subtract the integrated photocurrent corresponding to the negative waveform from the integrated photocurrent corresponding to the positive waveform, mimicking the superposition of the probed photocurrents as in (19).

The challenge here is that $\tau(\Delta t)$ may exceed the given total integration time α and the question is how do we adjust $\tau(\Delta t)$ so that $\tau(\Delta t) \leq \alpha$? To address this challenge, we further optimize the GST algorithm.

Recall that Δt is an arbitrary integration time for each bias (bias-time interval) and α is the desired integration time. As defined in (24), $\tau(\Delta t)$ is the integration time combined with weights, which it is assumed to be continuous. However, $\tau(\Delta t)$ may not be monotonic. In fact, there is a critical Δt, call it t^* such that $\tau(t^*) = \alpha$, illustrated in Fig. 6.7. Ideally, t^* is the solution to $\tau(\Delta t) = \Delta t$.

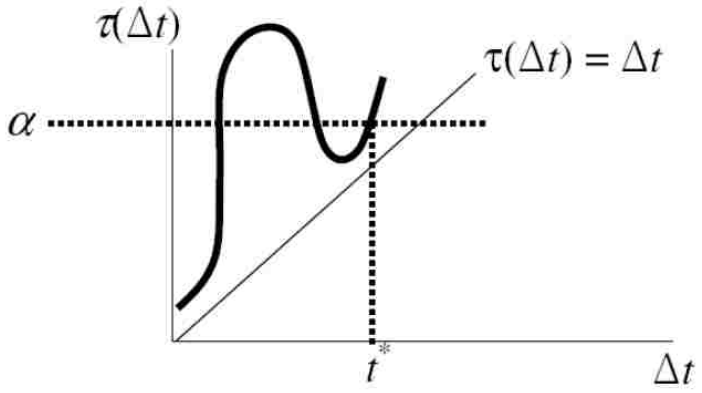

Figure 6.7: Illustration of non-monotonic $\tau(\Delta t)$ as a function of Δt for finding a critical point t^*, which satisfies $\tau(t^*) = \alpha$.

As an approximation, t^* can be solved by satisfying

$$t^* = \sup\{\Delta t : (1-\varepsilon)\alpha \le \tau(\Delta t) \le \alpha\}, \qquad (25)$$

where ε is the tolerance of α, usually ε = 0.02 gives good results.

The computational procedure to search t^* is described as follows.

1) The normalized weight $\hat{w}_i$ is obtained by using (23) and then each Δt is scaled by $|\hat{w}_i|$, yielding a weighted bias time b_i.

2) With b_i available from Step 1, $\tau(\Delta t)$ is calculated by using (24) and if $\tau(\Delta t) = \alpha$, the search is complete with $t^* = \Delta t$ and the corresponding biasing waveform is obtained. Otherwise, go to the next step.

3) Set $\Delta t = \Delta t/2$ and $\tilde{t} = 2\Delta t$.

4) Recalculate $\hat{w}_i$ and b_i.

5) Compute $\tau(\Delta t)$: if $\tau(\Delta t) > \alpha$, then go back to Step 3; if $\tau(\Delta t)$ satisfies (25), then $t^* = \Delta t$. Otherwise, set $\Delta t = (\Delta t + \tilde{t})/2$ and go back to Step 4.

6.4 Simulation results on spectrometry and classification

For validation, we applied the GST algorithm for the same MS sensing problems as demonstrated for the ST algorithm in Section 6.2. For the spectrometry problem, the continuous time-varying bias waveform, which consists of negative and positive waveforms, was obtained by the GST algorithm as shown in Fig. 6.8. According to these two waveforms, we integrated two photocurrents. The progression curves for integrating photocurrents corresponding to negative and positive waveforms are shown in Fig. 6.9. The integrated photocurrent for negative waveform, $\hat{I}_{neg}$, is 0.472 and the integrated photocurrent for positive waveform, $\hat{I}_{pos}$, is 0.619. To reconstruct the emissivity of an object at 8.8 μm, we simply subtracted $\hat{I}_{neg}$ from $\hat{I}_{pos}$, yielding $\hat{I} = \hat{I}_{pos} - \hat{I}_{neg} = 0.147$. By comparison, this reconstructed emissivity (0.147) by the GST algorithm is closer to the ground truth (0.171 shown in Table 6.1) than the value (0.134 shown in Table 6.1) obtained by the ST algorithm in Section 6.2. Thus, the GST algorithm performs better than the original ST algorithm in successfully extracting the narrowband spectral feature. Specifically for this problem, the GST algorithm reconstructed the emissivity of an object with a 14% of error rather than the ST algorithm, which achieved a 21% error for the same reconstruction.

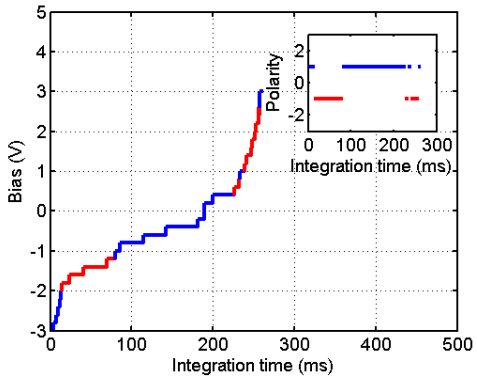

Figure 6.8: Continuous time-varying biasing waveform obtained by the GST algorithm for the spectrometry problem. This bias waveform consists of negative waveform (shown in red) and positive waveform (shown in blue), which are used to integrate photocurrents. Inset shows the negative and positive signs of weights over the integration time.

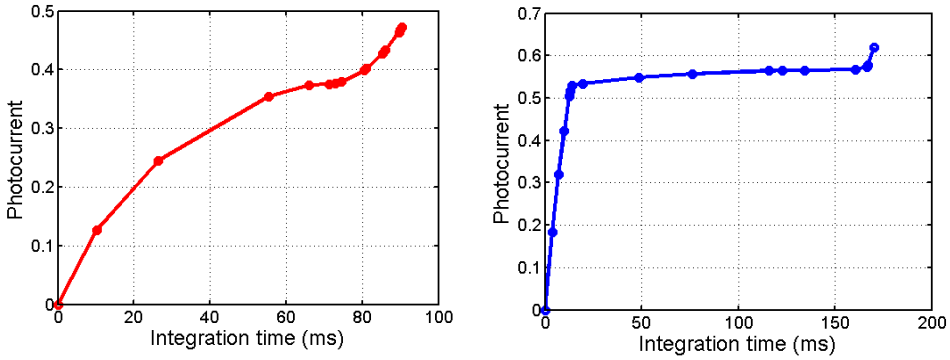

Figure 6.9: Integrated photocurrents, $\hat{I}_{neg}$ and $\hat{I}_{pos}$, based on negative waveform (left) and positive waveform (right). Subtraction of $\hat{I}_{neg}$ from $\hat{I}_{pos}$ gives a reconstruction of the emissivity of an object sampled at 8.8 µm using the spectral filter.

Reconstructed sample of emissivity	Methods		True value (Sampled transmittance by ideal triangle)
	ST algorithm	GST algorithm	
at 8.8 µm	0.134	0.147	0.171

Table 6.1: Comparison of reconstructed emissivity at 8.8 µm between the conventional ST algorithm and the GST algorithm. Results are also compared to the true value of the emissivity.

For the classification problem, three bias waveforms were computed by the GST algorithm as shown in Fig. 6.10. Each bias waveform includes negative (Fig. 6.10 (red)) and positive (Fig. 6.10 (blue)) waveforms that were used to successfully design each algorithmic matched filter as shown in Fig. 6.11. Three algorithmic matched filters were then labeled with the appropriate class number (Class 1, Class 2 and Class 3).

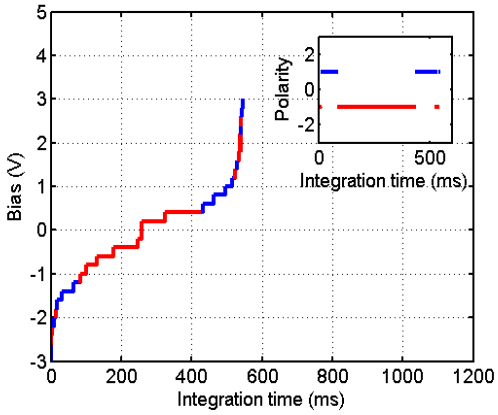

(a)

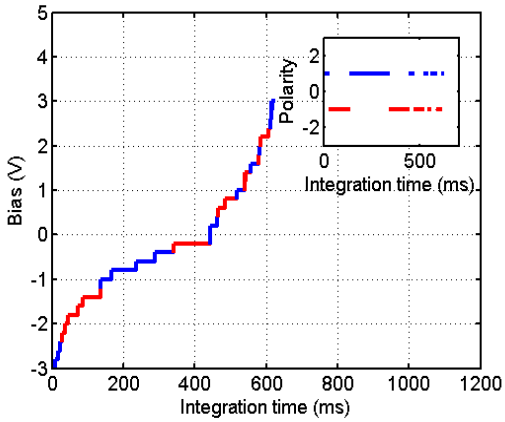

(b)

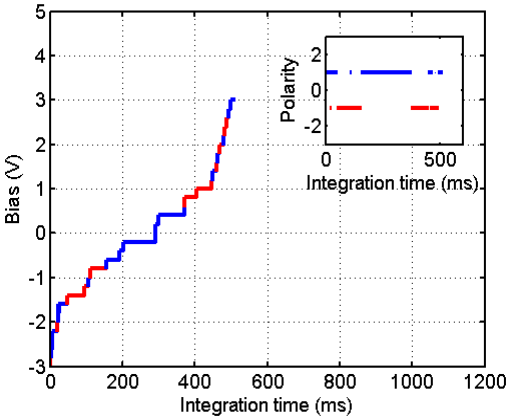

(c)

Figure 6.10: Three bias waveforms each including negative (in red) and positive (in blue) waveforms for three algorithmic matched filters, (a) $\hat{r}(\lambda;\lambda_1)$, (b) $\hat{r}(\lambda;\lambda_2)$ and (c) $\hat{r}(\lambda;\lambda_3)$. Inset shows the negative and positive signs of weights over the integration time.

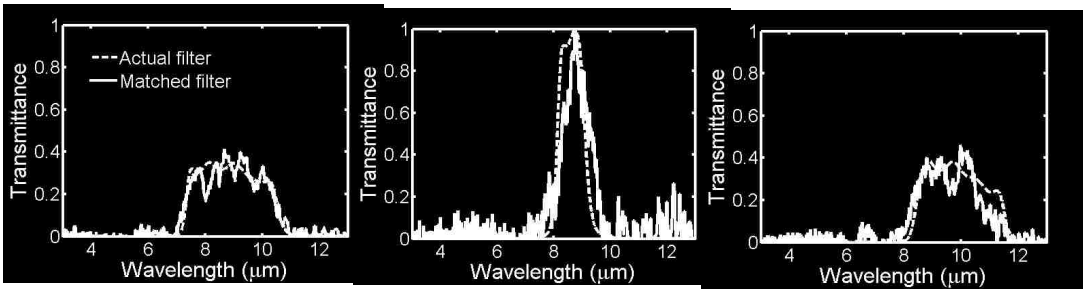

Figure 6.11: Transmittances of three algorithmic spectral matched filters, $\hat{r}(\lambda;\lambda_1)$ (left), $\hat{r}(\lambda;\lambda_2)$ (middle) and $\hat{r}(\lambda;\lambda_3)$ (right) in solid black line were obtained by the GST algorithm using the bias waveforms as shown in Fig. 6.10. Actual filter transmittances, $r_1(\lambda;\lambda_1)$ (left), $r_2(\lambda;\lambda_2)$ (middle) and $r_3(\lambda;\lambda_3)$ (right) are shown in dashed line.

Based on the bias waveforms shown in Fig. 6.10, the curves showing the integration of photocurrents were obtained. Each curve represents the process of continuously probing the test filter object, $r_1(\lambda;\lambda_1)$ with the DWELL photodetector controlled by the bias waveforms in Fig. 6.10.

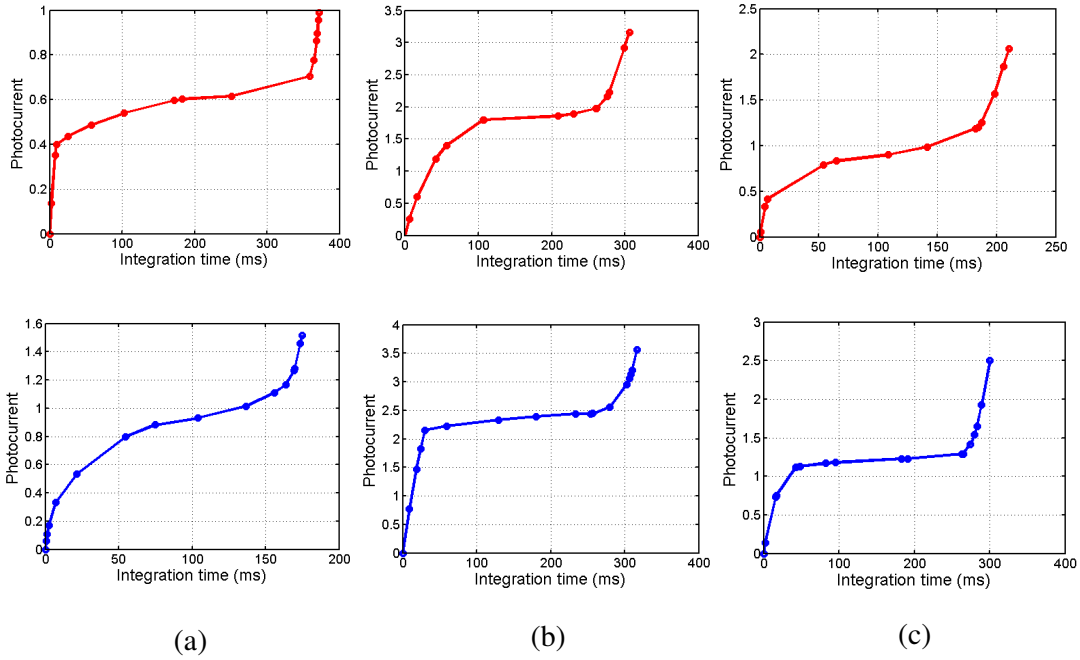

Figure 6.12: Integrated photocurrents, $\hat{I}_{neg,class}$ (from red curve) and $\hat{I}_{pos,class}$ (from blue curve) for (a) Class 1, (b) Class 2 and (c) Class 3 based on the bias waveforms as shown in Fig. 6.10.

From the curves shown in Fig. 6.12 (a), the integrated photocurrents for negative and positive bias waveforms, $\hat{I}_{\text{neg, class 1}}$ and $\hat{I}_{\text{pos, class 1}}$, are 0.99 and 1.515 for Class 1, respectively. For Class 2, the integrated photocurrents, $\hat{I}_{\text{neg, class 2}}$ and $\hat{I}_{\text{pos, class 2}}$, are 3.164 and 3.563 obtained from Fig. 6.12 (b). For Class 3, the integrated photocurrents, $\hat{I}_{\text{neg, class 3}}$ and $\hat{I}_{\text{pos, class 3}}$ are 2.064 and 2.504 obtained from Fig. 6.12 (c). To perform the feature extraction for each class, we subtracted the integrated photocurrent corresponding to negative waveform from the one corresponding to positive waveform, in the same way as we did for the spectrometry example, yielding three features ($F_1 = \hat{I}_{\text{pos, class 1}} - \hat{I}_{\text{neg, class 1}} = 0.525$, $F_2 = \hat{I}_{\text{pos, class 2}} - \hat{I}_{\text{neg, class 2}} = 0.399$, $F_3 = \hat{I}_{\text{pos, class 3}} - \hat{I}_{\text{neg, class 3}} = 0.44$). These three features then form a feature vector **F** (**F**=[F_1, F_2, F_3]). According to the classification rule, $i^* = \arg\max_{i \in \{1,2,3\}} F_i$ as mentioned in Section 6.2, the classifier assigned **F** to Class 1 since feature value (F_1) in **F** is the largest among three features. Thus, the classifier correctly identified the test filter object, $r_1(\lambda;\lambda_1)$ by assigning it to Class 1. The plot for the feature vector **F** is shown in Fig. 6.13 (blue). By comparison with the reference, the classification results shown in Fig. 6.13 demonstrate that classifiers by both algorithms have correctly assigned the test object to Class 1 based on extracted feature vectors.

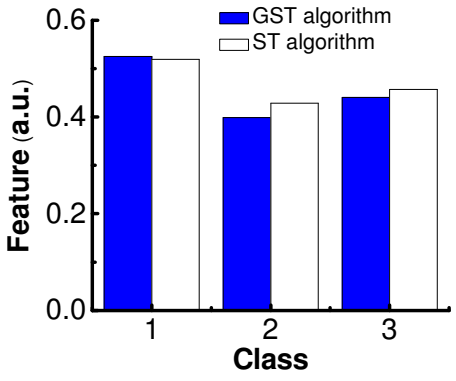

Figure 6.13: Classification results for the GST algorithm (blue) compared to the conventional ST algorithm (white) for identifying the test filter object, $r_1(\lambda;\lambda_1)$. Results show that the classifier has successfully classified the test object to Class 1 using both algorithms.

6.5 Conclusions

We have generalized the spectral tuning algorithm to yield a continuous time-varying bias waveform, which enables the detector to extract the most relevant spectral feature for a specific multispectral sensing application in a limited integration time. As a result of generalization, the algorithm extracts the feature by integrating the photocurrent with appropriately adjusted biases based on a prescribed bias waveform instead of forming a weighted superposition of photocurrents. It is to be emphasized that the impact of generalization is to significantly simplify the conventional spectral tuning algorithm by absorbing its data-processing steps such as multiplications and superpositions in the photocurrent integration process, making the algorithm available for hardware implementation. In addition, the reduction of data-processing steps can greatly simplify the design of required multispectral sensing system such as the ROIC of the FPA system, which, in turn, would reduce the required cost of a system.

We successfully validated the algorithm by means of simulation for two multispectral sensing problems: the spectrometry of a target spectral filter and the classification among three LWIR filter targets based on algorithmic spectral matched filters. Results were comparable to the reference obtained by the conventional spectral tuning algorithm. The next step is to implement our generalized spectral tuning algorithm on the actual hardware system (the reconfigurable ROIC-based FPA) to demonstrate multispectral spectrometry and classification applications in real time.

Summary of Dissertation

The electrical tunability of DWELL has been exploited through post-processing algorithms enabling target spectrometry and spectral matched filtering for material classification, without using any physical spectral filters. Algorithms provide the functionality of spectral filtering with spectral resolutions well beyond the limits offered by the normal operation of the DWELL detector.

In this dissertation, the DWELL-based algorithmic spectrometer (DAS) based on the concept of algorithmic spectral tuning was demonstrated experimentally for the first time. The DAS was implemented in three steps. First, the DWELL detector probed an unknown object of interest sequentially at different applied biases, yielding the set of bias-dependent photocurrents. Second, the set of photocurrents was linearly combined with the pre-calculated weights for the specific tuning wavelength. Such synthesized photocurrent is the reconstructed transmittance of object at that wavelength. Last, the second step was repeated for the entire tuning wavelength range of interest to obtain the continuous transmittance waveform of unknown object without using any physical spectrometer. The DAS successfully reconstructed the transmittances of various LWIR filter targets and was further investigated for the SNR, the DWELL's operating temperature, and the diversity of available operating biases. The DAS was also successfully demonstrated by an other collaborating research group. The DAS can be potentially applied to traditional multi-color infrared detectors (e.g., quantum-well detectors), especially if there is overlap in the spectral bands.

The spectral tuning algorithm was further extended to perform the data-compressive spectral sensing by identifying a minimal set of required biases subject to a prescribed performance level. This minimal bias set is a uniformly-accurate solution across arbitrarily specified spectral sensing problems beyond spectrometry, including spectral matched filtering and slope sensing. As a result, the detector can sense the object of interest using only the most relevant spectral responses for multiple sensing applications. The algorithm was implemented to approximate the collection of six different spectral filters and identified the minimal set of only four biases out of 30 available DWELL biases. The use of minimal four biases successfully approximated all six spectral filters. For demonstration, the algorithm with these four biases was applied to two remote-sensing problems: (1) spectrometry of unknown filter target and (2) classification of three matched filter targets. Successful results were obtained for

both problems using only four biases.

Finally, the spectral tuning algorithm was generalized to offer a continuous time-varying biasing, which mimics the multispectral capabilities of the conventional algorithmic spectral tuning without performing a weighted superposition of the DWELL's bias-dependent photocurrents. As a result of generalization, the process of spectral tuning algorithm was greatly simplified by absorbing the required data-processing steps (multiplications and superpositions associated with weights) in the photocurrent integration process using a continuous time-varying bias function under the integration time constraint. This generalization is particularly relevant to the algorithm implementation on the hardware (FPA) system, where the photocurrent integration time and the bias voltage are controlled by the readout circuit.

Future Works

1. Implementation of algorithmic sensing modalities to a programmable ROIC

The intelligent read-out integrated circuit (iROIC) [44] is capable of the pixel-level bias control as well as the data computation in the programmable analog function blocks. The main objective is to perform the spectral sensing modalities within iROIC. Sensing modalities are the algorithmic parallel spectrometer (APS) and the algorithmic parallel matched filtering (APMF). The APS consists of the bias-tunable FPA hybridized with the iROIC, programmed to perform in parallel the operation of data-compressive algorithmic spectrometry. The idea of APS is illustrated in Fig. 1. Consider that templates are placed in uniform regions consisting of the same type of target in a scene. Within each template, the iROIC applies different bias in the prescribed minimum bias set (by the compressive spectral sensing algorithm) to each pixel, generating the minimum set of photocurrents. In this way, we can extract out the most relevant spatial and spectral information of target of interest simultaneously within a single frame. Then the processor within iROIC can compute in parallel a weighted superposition of the photocurrents obtained from the spectral bands (controlled by the minimal bias set), generating the amplitude of the spectrogram of the target probed for a specific tuning wavelength. Then it is repeated for the entire wavelength range of interest to obtain the complete spectral profile of the target. The second modality, APMF consists of the iROIC programmed to perform in parallel the matched filtering with the prescribed minimal bias set for spectral classification. The main idea is to perform the classification with just two frames. One frame is for training and activating the classifier and the other frame is for classifying the incoming test data with the trained classifier. For both modalities, performing algorithm at the pixel level and within the iROIC can potentially enable fast and high-performance processing, thereby extracting the compressed and important spectral feature directly.

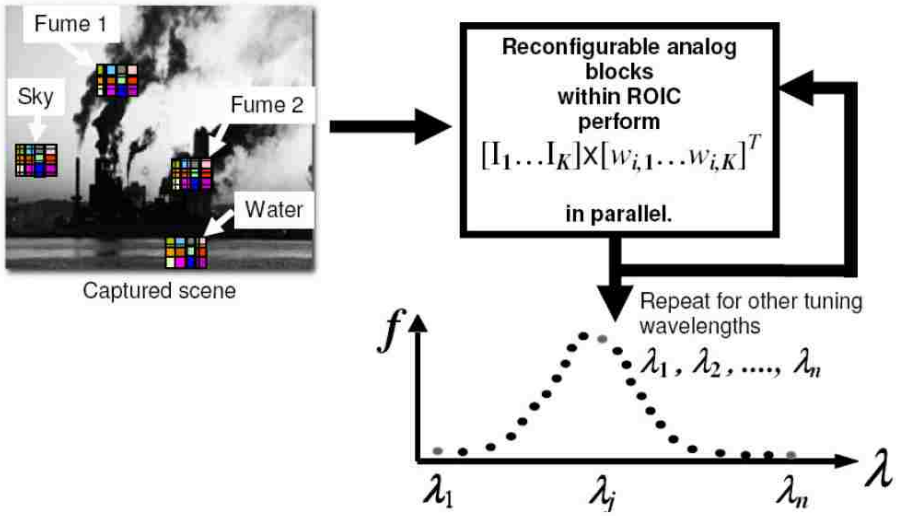

Figure 1: Idea of the algorithmic parallel spectrometer (APS). As the iROIC hybridized FPA probes a scene, the spectrogram of different regions of interest can be produced directly as an output of the device. The templates shown represent different groups of pixels; each group sees a region consisting of a uniform target.

2. Application of algorithmic sensing modalities on the plasmonic and tunable DWELL detector

Recently, our group had demonstrated for the first time a plasmon integrated DWELL FPA (SP-FPA) [45] using near field spectrally-resonant coupling of the surface plasmon-polaritons (SPPs) with mid-IR absorption in the quantum dots. The entire structure consists of a 2-D periodic hole array (as a SP structure) coupled on top of a DWELL absorber structure.

This structure showed improvement in spectral response at all the plasmonic resonances used on the FPA, as shown in Figure 2 (a) and (b). Figure 2 (a) shows the spectral response of SP-FPA (blue) and the spectral response of FPA (black), while Figure 2 (b) shows the difference plot between the spectral responses of SP-FPA and FPA. Figures 2 (d)-(g) show the visual demonstration of the resonant enhancement with a series of visual images.

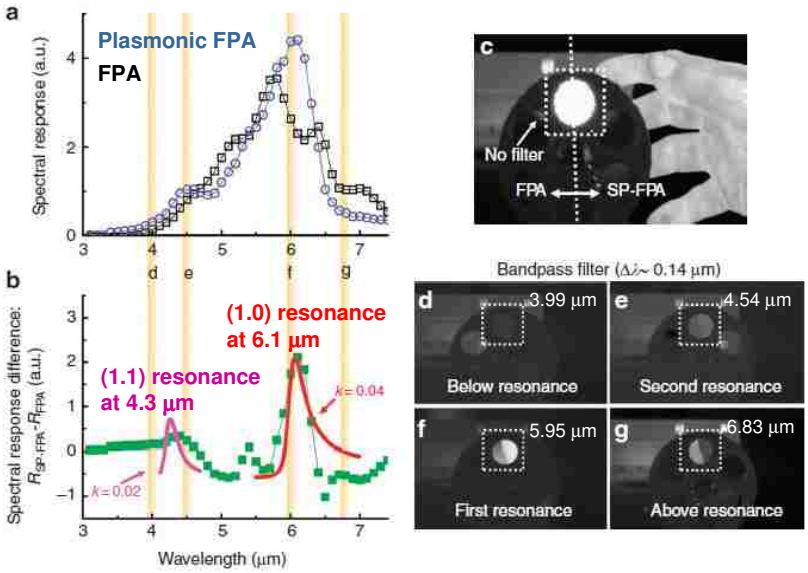

Figure 2: (a) Spectral responses of the non-SP and SP sections of the array. (b) Difference in spectral response showing the experimentally observed peaks at the (1,1) and (1,0) resonances. (c) Representative image of the blackbody source seen through the open slot in the filter wheel. Blackbody images (d) below the (1,1) resonance at λ = 3.99 µm, (e) near the (1,1) resonance at λ = 4.54 µm, (f) close to the (1,0) resonance at λ = 5.95 µm and (g) above the (1,0) resonance at λ = 6.83 µm [45].

The plasmonic resonance as well as the bias-dependent spectral tunability of DWELL has not been explored in our group as yet. The essential concept is that pixels with

different plasmonic structures as well as applying different biases can be operated as different detectors. Target spectral reconstruction using a DWELL FPA alone is insufficient for a target with very sharp spectral features. The combined use of both plasmonic resonance and bias-tunability can potentially produce spectral responses with higher SNRs, better resolution, and more spectral diversity than just the DWELL FPA alone, resulting in improved synthetic spectral filter reconstruction. Potential applications are gas and effluent discharge identification that require very high resolution spectrometry as illustrated in Fig. 3. The idea is to perform the spectral sensing modalities (algorithmic spectrometer and spectral matched filter) using the plasmonic DWELL detector to achieve very high resolution MS/HS sensing.

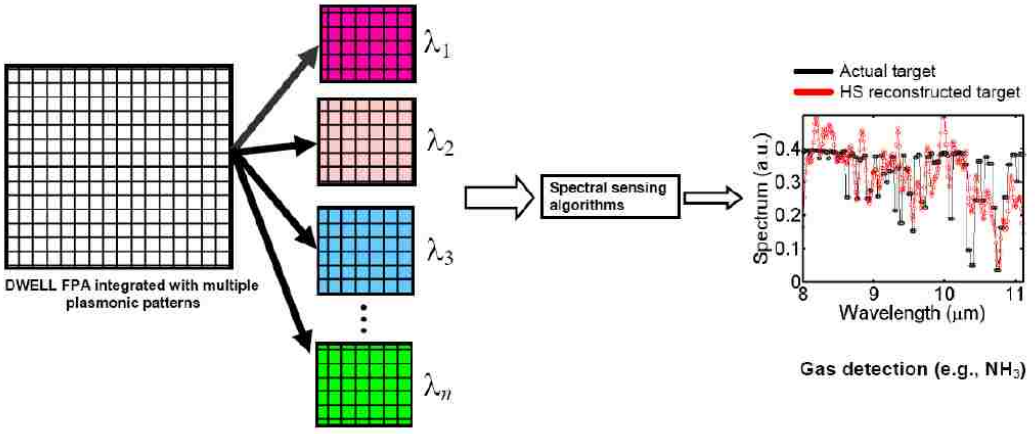

Figure 3: Potential application of the plasmonic DWELL detector with the spectral sensing modalities

References

[1] A. Rogalski, ‘‘Assessment of HgCdTe photodiodes and quantum well infrared photoconductors for long wavelength focal plane arrays,’’ *Infrared Phys. Technol*., Vol. 40, pp. 279–294, 1999.

[2] A. Rogalski, “Quantum well photoconductors in infrared detector technology,” *J. Appl. Phys.,* Vol. 93, pp. 4355-4391, 2003.

[3] T. E. Vandervelde, M. C. Lenz, E. Varley, A. Barve, J. Shao, R. Shenoi, D. A. Ramirez, W-Y. Jang, Y. D. Sharma and S. Krishna, “Quantum Dots-in-a-Well Focal Plane Arrays,” *IEEE Journal of Selected Topics in Quantum Electronics*, Vol. 14, pp. 1150-1161, 2008 (Invited).

[4] N. Streibl, U. Nolscher, J. Jahns, and S. Walker, “Array generation with lenslet arrays,” *Appl. Opt*., Vol. 30, pp. 2739-2742, 1991.

[5] C. A. Musca, J. Antoszewski, K. J. Winchester, A. J. Keating, T. Nguyen, K. K. M. B. D. Silva., J. M. Dell, L. Faraone, P. Mitra, J. D. Beck, M. R. Skokan, and J. E. Robinson, “Monolithic integration of an infrared photon detector with a MEMS-based tunable filter,” *IEEE Elec. Dev. Lett*., Vol. 26, pp. 888–890, 2005.

[6] N. Gupta, R. Dahmani, and S. Choy, “Acousto-optic tunable filter based visible- to near-infrared spectropolarimetric imager,” *Opt. Eng*., Vol. 41, pp. 1033-1038, 2002.

[7] Yu. G. Sidorov, S. A. Dvoretsky, M. V. Yakushev, N. N. Mikhailov, V. S. Varavin and V. I. Liberman, “Peculiarities of the MBE growth physics and technology of narrow-gap II-VI compounds,” *Thin Solid Films*, Vol. 306, Issue 2, pp. 253, Sep., 1997.

[8] J. Phillips, “Evaluation of the fundamental properties of quantum dot infrared detectors,” *Journal of Applied Physics*, Vol. 91, No. 7, Apr., 2002.

[9] D. Tezcan, S. Eminoglu and T. Akin, “A Low-Cost Uncooled Infrared Microbolometer Detector in Standard CMOS Technology,” *IEEE T. Elec. Dev*., Vol. 50, pp. 494-502, 2003.

[10] D. L. Smith and C. Mailhiot, “Proposal for strained type II superlattice infrared detectors,” *J. Appl. Phys.*, Vol. 62, pp. 2545-2548, 1987.

[11] H. S. Kim, E. Plis, J. B. Rodriguez, G. D. Bishop, Y. D. Sharma, L. R. Dawson, S. Krishna, J. Bundas, R. Cook, D. Burrows, R. Dennis, K. Patnaude, A. Reisinger, and M. Sundaram, "Mid-IR focal plane array based on type-II InAs/GaSb strain layer superlattice detector with nBn design” *Appl. Phys. Lett*. 92, 183502, 2008.

[12] B. F. Levine, “Quantum-well infrared photodetectors,” *J. Appl. Phys*., Vol. 74, pp. R1-R81, 1993.

[13] K. W. Berryman, S. A. Lyon and M. Segev, “Mid-infrared photoconductivity in InAs quantum dots,” *Appl. Phys. Lett*., Vol. 70, pp. 1861-1863, 1997.

[14] S. D. Gunapala, S. V. Bandara, C. J. Hill, D. Z. Ting, J. K. Liu, S. B. Rafol, E. R. Blazejewski, J. M. Mumolo, S. A. Keo, S. Krishna, Y.-C. Chang, and C. A. Shott, “640 x 512 Pixels Long-

Wavelength Infrared (LWIR) Quantum-Dot Infrared Photodetector (QDIP) Imaging Focal Plane Array," *IEEE Journal of Quantum Electronics*, Vol. 43, pp. 230-237, 2007.

[15] J. Phillips, P. Bhattacharya, S. W. Kennerly, D. W. Beekman, and M. Dutta, "Self-assembled InAs-GaAs quantum-dot inter-subband detectors," *IEEE J. Quantum Electron.,* Vol. 35, pp. 936–942, 1999.

[16] J. Phillips, "Evaluation of the fundamental properties of quantum dot infrared detectors," *Journal of Applied Physics*, Vol. 91, No. 7, Apr., 2002.

[17] M. R. Matthews, R. J. Steed, M. D. Frogley, C. C. Phillips, R. S. Attaluri, and S. Krishna, "Transient photoconductivity measurements of carrier lifetimes in an InAs/$In_{0.15}Ga_{0.85}As$ dots-in-a-well detector," *Appl. Phys. Lett.,* Vol. 90, pp. 103519 - 103519-3, 2007.

[18] D. A. B. Miller, D. S. Chemla, T. C. Damen, A. C. Gossard, W. Wiegmann, T. H. Wood, and C. A. Burrus, "Band-Edge Electroabsorption in Quantum Well Structures: The Quantum-Confined Stark Effect," *Physical Review Letters.*, Vol. 53, pp. 2173–2176, Nov. 1984.

[19] P. Aivaliotis, N. Vukmirovic, E. A. Zibik, J. W. Cockburn, D. Indjin, P. Harrison, C. Groves, J. P. R. David, M. Hopkinson, and L. R. Wilson, "Stark shift of the spectral response in quantum dots-in-a-well infrared photodetectors," *Journal of Physics D*, Vol. 40, pp. 5537-5540, 2007.

[20] S. Krishna, "InAs/InGaAs quantum dots in a well photodetectors," *J. Phys. D (Appl. Phys.)*, Vol. 38, pp. 2142–2150, 2005.

[21] Ü. Sakoğlu, J. S. Tyo, M. M. Hayat, S. Raghavan and S. Krishna, "Spectrally Adaptive Infrared Photodetectors Using Bias-Tunable Quantum Dots," *Journal of the Optical Society of America B*, Vol. 21, pp. 7-17, 2004.

[22] Ü. Sakoğlu, M. M. Hayat, J. S. Tyo, P. Dowd, S. Annamalai, K. T. Posani, and S. Krishna, "A statistical method for adaptive sensing using detectors with spectrally overlapping bands," *Applied Optics*, Vol. 45, pp. 7224–7234, Oct. 2006.

[23] S. Krishna, M. M. Hayat, J. S. Tyo, Ü. Sakoğlu and S. Raghavan "Spectrally Adaptive Quantum Dots In A Well Detector", US Patent 7,217,951, 2007.

[24] Ü. Sakoğlu, "Signal-processing strategies for spectral tuning and chromatic nonuniformity correction for quantum-dot IR sensors," *Ph.D. Dissertation*, Univ. New Mexico, Albuquerque, 2006.

[25] Z. Wang, Ü. Sakoğlu, S. Annamalai, N.-R. Weisse-Bernstein, P. Dowd, J. S. Tyo, M. M. Hayat, and S. Krishna, "Real-time implementation of spectral matched filtering algorithms using adaptive focal plane array technology," in *Imaging Spectrometry*, *Proc. SPIE*, Vol. 5546, pp. 73–83, 2004.

[26] Ü. Sakoğlu, Z. Wang, M. M. Hayat, J. S. Tyo, S. Annamalai, P. Dowd, and S. Krishna, "Quantum dot detectors for infrared sensing: bias-controlled spectral tuning and matched filtering," in *Nanosensing: Materials and Devices, Proc. SPIE*, Vol. 5593, pp. 396–407, 2004.

[27] W-Y. Jang, B. Paskaleva, M. M. Hayat and S. Krishna, "Spectrally Adaptive Nanoscale Quantum Dot Sensors," *Wiley Handbook of Science and Technology for Homeland Security*, 2009.

[28] W-Y. Jang, M. M. Hayat, J. S. Tyo, R. S. Attaluri, T. E. Vandervelde, Y. D. Sharma, R. Shenoi, A. Stintz, E. R. Cantwell, S. C. Bender, S. J. Lee, S. K. Noh and S. Krishna, "Demonstration of Bias-Controlled Algorithmic Tuning of Quantum Dots in a Well (DWELL) MidIR Detectors," *IEEE Journal of Quantum Electronics*, Vol. 45, pp. 674-683, 2009.

[29] S. Krishna, M. M. Hayat, J. S. Tyo and W-Y. Jang, "Infrared Retina," US Patent 8,071,945 B2, 2011.

[30] P. Vines, C. H. Tan, J. P. R. David, R. S. Attaluri, T. E. Vandervelde, S. Krishna, W-Y. Jang and M. M. Hayat, "Versatile Spectral Imaging With an Algorithm-Based Spectrometer Using Highly Tuneable Quantum Dot Infrared Photodetectors," *IEEE Journal of Quantum Electronics*, Vol.47, pp. 190-197, 2011.

[31] W-Y. Jang, M. M. Hayat, S.E. Godoy, S. C. Bender, P. Zarkesh-ha and S. Krishna, "Data compressive paradigm for generalized multispectral sensing using tunable DWELL mid-infrared detectors," *Optics Express*, Vol. 19, pp. 19454-19472, 2011.

[32] P. Bhattacharya, *Semiconductor Optoelectronic Devices*, 2nd ed. Englewood Cliffs, NJ: Prentice Hall, 1996.

[33] J. Andrews, W.-Y. Jang, J. E. Pezoa, Y. D. Sharma, S. J. Lee, S. K. Noh, M. M. Hayat, S. Restaino, S. W. Teare, and S. Krishna, "Demonstration of a bias tunable quantum dots-in-a-well focal plane array," *Infrared Phys. Technol.*, Vol. 52, pp. 380–384, 2009.

[34] J. R. Andrews, S. R. Restaino, S. W. Teare, Y. D. Sharma, W-Y. Jang, T. E. Vandervelde, J. S. Brown, A. Reisinger, M. Sundaram, S. Krishna and L. Lester, "Comparison of Quantum Dots-in-a Double-Well and Quantum Dots-in-a-Well Focal Plane Arrays in the Long Wave Infrared," *IEEE Transactions on Electron Devices*, Vol. 58, pp. 2022-2027, 2011.

[35] B. S. Paskaleva, M. M. Hayat, Z. Wang, J. S. Tyo, and S. Krishna, "Canonical correlation feature selection for sensors with overlapping bands: Theory and application," *IEEE Trans. Geosci. Remote Sens.*, Vol. 46, pp. 3346–3358, 2008.

[36] B. S. Paskaleva, W-Y. Jang, S. C. Bender, Y. D. Sharma, S. Krishna and M. M. Hayat, "Multispectral Classification with Bias-tunable Quantum Dots-in-a-Well Focal Plane Arrays," *IEEE Sensors Journal*, Vol. 11, pp. 1342-1351, 2011.

[37] A. Milton, F. Barone, and M. Kruer, "Influence of nonuniformity on infrared focal plane array performance," *Opt. Eng. (Bellingham)*, Vol. 24, pp. 855–862, 1985.

[38] R. O. Duda, P. E. Hart, and D. G. Stork, *Pattern Classification*. New York: Wiley, 2000.

[39] S. F. Cotter, B. D. Rao, Kjersti Engan, and K. Kreutz-Delgado, "Sparse Solutions to Linear Inverse Problems with Multiple Measurement Vectors," *IEEE Trans. Signal Process*. Vol. 53, pp. 2477–2488, 2005.

[40] G. Davis, S. Mallat, and M. Avellandeda, "Adaptive greedy approximations," *Constr. Approx.*, Vol. 13, pp. 57–98, 1997.

[41] A. Majumdar, K. K. Choi, J. L. Reno, L. P. Rokhinson, and D. C. Tsui, "Two-color quantum-well infrared photodetector with voltage tunable peaks," *Appl. Phys. Lett.* Vol. 80, pp. 707–709, 2002.

[42] Hsieh, et al., *IEEE Trans. on Circuits and Sys. for Video Proc.*, 7(4), 594-605, 1997.

[43] M. G. Brown, J. Baker, C. Colonero, J. Costa, T. Gardner, M. Kelly, K. Schultz, B. Tyrrell and J. Wey, "Digital-pixel Focal Plane Array Development," *Proc. of SPIE*, Vol. 7608, pp. 76082H-1-76082H-10, 2010.

[44] P. Zarkesh-Ha, W-Y. Jang, P. Nguyen, A. Khoshakhlagh and J. Xu, "A Reconfigurable ROIC for Integrated Infrared Spectral Sensing," *the 23rd Annual Meeting of the IEEE Photonics Society Volume,* pp. 714-715, 2010.

[45] S. J. Lee, Z. Ku, A. Barve, J. Montoya, W-Y. Jang, S. R. J. Brueck, M. Sundaram, A. Reisinger, S. Krishna and S. K. Noh, "A Monolithically Integrated Plasmonic Infrared Quantum Dot Camera," *Nature Communications*, 2, 286, 2011.

[46] T. Yasuda *et al.*, "Adaptive-Integration-Time Image Sensor With Real-Time Reconstruction Function," *IEEE Trans. Elect. Dev.*, Vol. 50, pp. 111-120, 2003.

[47] T. Ogi *et al.*, "Smart image sensor for wide dynamic range by variable integration time," *IEEE Conf. on Multisensor Fusion and Integration for Intelligent Systems*, pp. 179-184, 2003.

[48] T. Hamamoto *et al.*, "A Computational Image Sensor with Adaptive Pixel-Based Integration Time," *IEEE J. Solid-State Circuits*, Vol. 36, pp. 580-585, 2001.